UNIVERSITY OF JYVÄSKYLÄ

MASTER'S THESIS

Stabilization of the carrier-envelope offset frequency of an Yb:KYW femtosecond laser for the generation of an XUV comb for He^+ spectroscopy

Author:
Jorge MORENO

First supervisor:
Dr. Akira OZAWA

Second supervisor:
Dr. Ruben DE GROOTE

A thesis submitted in fulfillment of the requirements for the degree of Master of Science

in the

Department of Physics, JYU
Laser Spectroscopy Division, MPQ

June 1, 2021

Abstract

Stabilization of the carrier-envelope offset frequency of an Yb:KYW femtosecond laser for the generation of an XUV comb for He^+ spectroscopy

by Jorge MORENO

In this work, the carrier-envelope offset (CEO) frequency of an Yb:KYW frequency comb was detected and stabilized. The stabilization of the Yb:KYW frequency comb is an important step in a larger scale experiment to perform spectroscopy on the yet unexplored $1S$-$2S$ two-photon transition in He^+, by means of the generation of an XUV frequency comb. The output from the Yb:KYW mode-locked laser consists of 100 fs pulses emitted at a 40 MHz repetition rate and spectrally centered at 1033 nm, which were amplified, compressed and spectrally broadened up to an octave of frequencies. This allowed measuring the CEO frequency through f-$2f$ interferometry, and its stabilization via feedback to the Yb:KYW laser's pump current. By simultaneously controlling the CEO frequency and the frequency one optical mode of the comb (with an independent setup), all degrees of freedom in the frequency comb are locked, and the system is fully stabilized. We report on the design and construction of a fiber amplifier, pulse compressor, f-$2f$ interferometer and phase-locked loop system for the aforementioned goals, and present proof of their successful operation on the stabilization of the frequency comb.

Acknowledgements

The experimental part of this work was developed at the Max-Planck Institute for Quantum Optics in Garching, Germany. The 5 months I spent working at Prof. Hänsch's Laser Spectroscopy Division, with the team working on the He^+ project, were the most enriching time and lead me to confirm my passion for this field. For the guidance and inspiration they provided, I would like to thank Thomas Udem, Johannes Weitenberg, Fabian Schmid and, most especially, my supervisor Akira Ozawa.

I would also like to thank the University of Jyväskylä for allowing me to develop this work abroad despite this year's pandemic, and for assisting me financially. Thank you Leena Mattila, Tuomas Grahn, Sami Räsänen and Minttu Haapaniemi for giving an answer to all my questions and concerns, and helping me throughout this process. All my gratitude to Iain Moore, and especially to my supervisor Ruben de Groote, for introducing me to this field and for their genuine support and encouragement to pursue my aspirations.

Finally, I would like to thank my parents and dear friends. Without your unconditional support I would not have found the strength to follow this path and be where I am now.

Contents

List of Abbreviations

Yb:KYW	ytterbium-doped potassium yttrium tungstate
MLL	**M**ode-**L**ocked **L**aser
CW	**C**ontinuous **W**ave (laser)
CE(O)	**C**arrier-**E**nvelope (**O**ffset)
XUV	E**x**treme **U**ltra **V**iolet
GVD	**G**roup-**V**elocity **D**ispersion
GDD	**G**roup-**D**elay **D**ispersion
TOD	**T**hird-**O**rder **D**ispersion
SPM	**S**elf-**P**hase **M**odulation
SSFM	**S**plit-**S**tep **F**ourier **M**ethod
CPA	**C**hirped-**P**ulse **A**mplification
DC(F)	**D**ouble-**C**lad (**F**iber)
SM(F)	**S**ingle-**M**ode (**F**iber)
MM(F)	**M**ulti-**M**ode (**F**iber)
PCF	**P**hotonic-**C**rystal **F**iber
GRIN (lens)	**Gr**adient-**In**dex (lens)
HWP	**H**alf-**W**ave **P**late (i.e $\lambda/2$)
QWP	**Q**uarter-**W**ave **P**late (i.e $\lambda/4$)
PBS	**P**olarizing **B**eam**s**plitter
LD	**L**aser **D**iode
ACF	**A**uto**c**orrelation **F**unction
FROG	**F**requency-**r**esolved **O**ptical **G**ating
SHG	**S**econd-**H**armonic **G**eneration
HHG	**H**igh-**H**armonic **G**eneration
BBO (crystal)	**B**arium **Bo**rate (crystal)
APD	**A**valanche **P**hoto**d**etector
SA	**S**pectrum **A**nalyzer
PID (control)	**P**roportional-**I**ntegral-**D**erivative (control)
PLL	**P**hase-**L**ocked **L**oop

Chapter 1

Introduction

Quantum Electrodynamics (QED) is regarded as a paradigmatic model for other quantum field theories, and its extremely accurate predictions makes it one of the most successful theories in physics. In fact, the two quantities that can be calculated with the highest precision are the anomalous magnetic moment of the electron and the energy levels of hydrogen, this being one of the simplest bound state systems in QED.

As scientists, we would like to make sure this theory really describes nature, and if not completely, then find its limitations. This means we need to design experiments that can measure the quantities described by the theory with a level of precision that matches that achieved by its calculations, and then compare the results from theory and experiment. In simple terms, QED predictions depend on parameters that need to be adjusted to experimental data, and if we make the same number of measurements than there are parameters in our theoretical expression, we can obtain a numerical value for such parameters. If the goal is to test the theory, what we need is more measurements than parameters, so that one can compare the obtained values from different measurement sets and check for consistency within the theory. This way, if these measurements are consistent, one can claim that QED is valid up to a certain precision level, and if they are not, one could argue that QED fails to describe the studied phenomena at such precision. For this reason, high-precision experiments are a good way of searching for unknown phenomena and new physics.

Experiments with hydrogen and hydrogenic systems have always provided excellent tests for QED, since these are some of the simplest quantum systems, and they can be theoretically described with exceptionally high precision. In the last years, spectroscopic experiments in such systems have matched and pushed the limits in both theory and precision measurements [1–4]. For instance, the $1S$-$2S$ transition in hydrogen has been measured with an astounding fractional uncertainty of $4 \cdot 10^{-15}$. The QED expression for the energy levels of atomic hydrogen effectively depends on two parameters: the Rydberg constant R_∞ and the proton charge radius r_p. This means that other parameters such as the fine structure constant and the electron-to-proton mass ratio are better obtained from other experiments. Before 2010 a compound of 15 different measurements of transition frequencies gave consistent values for R_∞ and r_p and therefore QED passed the test. But measurements in muonic hydrogen [5] and further experiments in electronic hydrogen [4] showed a $> 5\sigma$ discrepancy with the previously accepted values for r_p and R_∞, and gave place to a still unresolved situation that has come to be known as the *proton radius puzzle* [6, 7]. In this context, new measurements in other hydrogen-like systems, such as that of

the 1*S*-2*S* transition in He^+[8] are of great interest and may shed some light on this problem.

Towards He^+ Spectroscopy

Exploring atomic transitions in He^+ has some advantages regarding QED tests, considering that high order correction terms scale with high powers of the atomic number Z. Furthermore, He^+ can be stored and sympathetically cooled in ion traps such as Paul or Penning traps, which reduces systematic uncertainties such as second-order Doppler shifts, collisional shifts or time-of-flight broadening.

The 1*S*-2*S* two-photon transition in He^+ needs to be driven resonantly with 61 nm XUV radiation, where there are no CW lasers available. Generation of this radiation at a power high enough to efficiently excite the two-photon transition poses a major technical challenge [9, 10]. The most promising approach consists of the generation of high harmonics from a near-infrared femtosecond frequency comb in an enhancement cavity [11, 12]. Starting from an Yb:KYW mode-locked laser that emits pulses at 1033 nm, the 17^{th} harmonic at 61 nm can be obtained via high-harmonic generation, which is inherently a very inefficient process and thus needs ultra-short pulses with very high intensity. Eventually, an XUV generated power of 10-100 μW tightly focused down to an area $< 10\ \mu m^2$ will be required for reaching significant detection rates [8]. The adversities in the 1*S*-2*S* He^+ experiment are evident, but measuring this transition can provide very relevant input for QED tests, and a more precise determination of the Rydberg constant, adding a new relevant piece to the proton-radius puzzle.

The fact that high peak intensities but also narrow bandwidths are needed for completing this high-precision experiment immediately calls for the use of a frequency comb.

Understanding the Frequency Comb

The first question is obvious; what exactly is a frequency comb and how does it work? And the short answer is: a frequency comb is a phase-stabilized mode-locked laser.

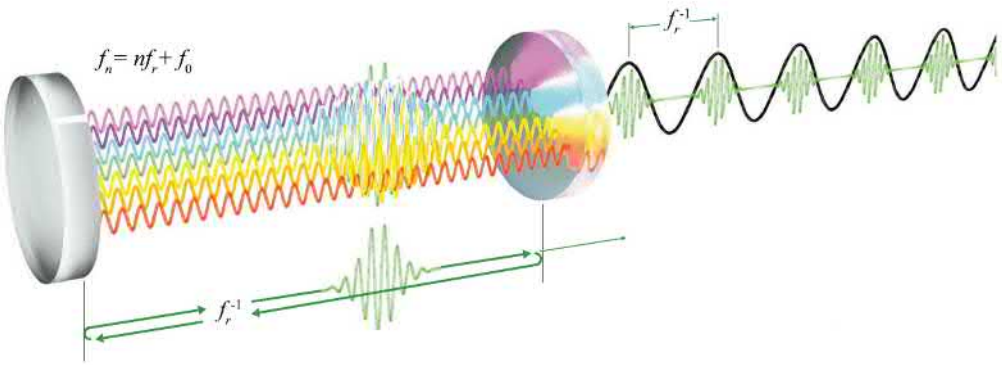

Fig. 1.1. Representation of the pulse formation in a frequency comb. In a frequency comb, the longitudinal modes of an optical cavity $f_n = nf_r + f_0$ are spatially overlapped and phase-coherent such that their superposition forms a pulse that circulates inside the cavity. The resulting output is a train of pulses emitted at the repetition rate f_r. From Diddams et al. [13]

Mode-locking is a technique by which one can make an optical oscillator produce ultra-short pulses of light, that can be as short as a few femtoseconds. So when talking about mode-locked lasers (MLL), we are basically talking about (pulsed) femtosecond lasers. These pulses are created by constructive interference of the resonant cavity's longitudinal modes, as is shown in Fig. 1.1. Mode-locking ensures constructive interference by enforcing every mode to be equidistant in frequency space and separated by a frequency f_r, and more importantly, that every mode is phase-coherent with each other, such that they share a common phase evolution. This produces a pulse inside the cavity that travels back and forth between the mirrors at its group velocity v_g, with a round trip time of $T_r = 2L/v_g = f_r^{-1}$, with L the cavity length. Every round trip, the pulse is partially transmitted by one of the mirrors (the output coupler), such that the output of the cavity consists of a series of pulses emitted at the repetition rate $f_r = T_r^{-1}$. It is useful to visualize this output as a carrier wave oscillating at an optical frequency ω_c, modulated by an envelope $A(t)$ with periodicity T_r. The fact that $A(t)$ is periodic in time, means the optical field outside the cavity can be decomposed in a Fourier series

$$E(t) = A(t)e^{i\omega_c t} = \sum_n a_n e^{i(\omega_c + n\omega_r)t} \tag{1.1}$$

where a_n are the Fourier components of $A(t)$ and $\omega_r = 2\pi/T_r$. One can see that, given the Fourier relation between time and frequency domains, the spectrum of this field is a set of equally spaced "deltas" or narrow lines. In other words, a frequency comb.

If every pulse were exactly the same and the modulation were to produce a pulse every n optical cycles, then the repetition rate f_r would be a sub-harmonic of the carrier frequency $f_r = f_c/n$, and the associated comb modes would be just $f_n = nf_r$. However, it must be noted that the output pulses are not identical to each other. Since there are dispersive elements in the cavity, such as the gain medium, the group and phase velocities are not equal, i.e. the pulse envelope and the optical carrier travel at different velocities inside the cavity. This produces a relative phase shift between the envelope and the carrier every round-trip, that is called the *carrier-envelope offset phase slip* $\Delta\varphi_{ce}$. The good thing is that this does not destroy coherence in the comb because the relative phase from pulse to pulse is always $\Delta\varphi_{ce}$, and the only effect this has is to shift every comb mode by the same frequency $f_0 = f_r\Delta\varphi_{ce}/2\pi$ [14], usually called the *carrier-envelope offset frequency*. This is depicted in Fig. 1.2.

The Comb Equation

Bringing together everything explained so far, one can describe the modes composing the spectrum of the MLL by the *frequency comb equation* [14–16]

$$f_n = nf_r + f_0\,. \tag{1.2}$$

This equation describes a set of optical modes f_n that are equally spaced by f_r and share a common offset f_0. The mode number n is in general on the order of $10^6 - 10^8$, and f_r and f_0 on the order of 10 MHz to 10 GHz, such that Eq.1.2 maps two microwave/radio frequencies onto the set of optical frequencies f_n. And it does so in a single step! Typically an optical frequency comb spectrum consists of hundreds of thousands up to a million of optical modes, spanning a bandwidth of hundreds of

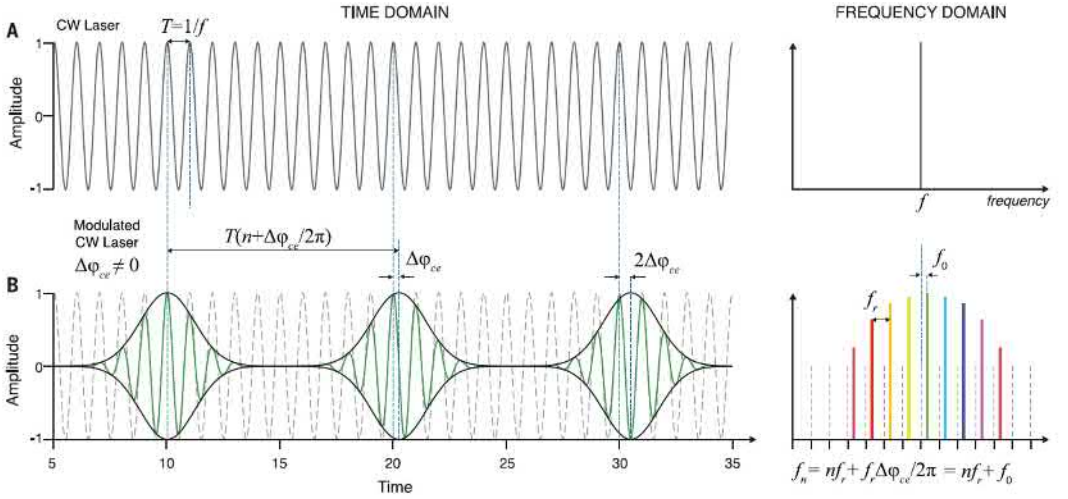

Fig. 1.2. Representation of the frequency comb in time and frequency domains. (A) Output of a continuous-wave (CW) laser, for reference. The Fourier transform of a harmonic signal of period $T = 1/f$ is a delta function centered at f. **(B)** The output of a mode-locked laser (MLL) is a train of periodic pulses, which is a frequency comb when Fourier transformed. Since there is a phase slip of $\Delta\varphi_{ce}$ from pulse to pulse, the period of the pulses' modulation T_r is not an exact multiple of the optical period T, but has some delay. This shifts the whole comb spectrum by an offset frequency f_0. From Diddams et al. [13]

terahertz in the optical domain. What is interesting, is that this comb has only two degrees of freedom, which are again f_r and f_0. If these two frequencies are controlled and stabilized to a precise radiofrequency reference, such as a Cs clock, one obtains more than 10^5 precisely defined optical frequencies in a single laser beam.

The f-$2f$ interferometer

The idea of the optical frequency comb seems rather simple and useful for many different experiments, so what took so long until it could be implemented? Not long after the first CW lasers were created, the MLL was invented too in the 1960s [17]. And while the nature of f_0 was understood around the 1970s [14], it was not until the 1990s that it was found how to measure and control it. It is precisely the control of the degrees of freedom of the comb what makes it a useful tool for high precision measurements.

The repetition rate is readily measurable by sending the pulsed laser beam into a regular photodetector, which will generate a periodic voltage at f_r that can be electronically resolved. Then, one can make a feedback loop to control the cavity length and lock the repetition rate at a constant value. By locking f_r, one prevents the comb lines from moving in an accordion-like manner.

On the other hand, measuring f_0 is not as straightforward, since it is an offset, common to every comb mode, that shifts the whole comb from the origin. The most common way of measuring f_0 is by using a so-called f-$2f$ interferometer [18, 19], which is a nonlinear interferometer that allows heterodyning (mixing) the second harmonic of an optical mode $2f_n$, taken from the low-frequency side of the comb spectrum, with a mode f_{2n} from the high-frequency side of the comb, to obtain $f_0 = 2f_n - f_{2n}$. Building such interferometer is one of the main parts of this work, and this process

will be explained in great detail in Chapter 5. Locking f_0 and f_r grants full control of the optical comb and is thus essential for high precision experiments.

The f-$2f$ method requires a spectrum broad enough to span an octave of frequencies, i.e. from f_n to f_{2n}, and this was highly simplified around the year 2000 with the invention of micro-structured or photonic crystal fibers (PCF). These are highly non-linear fibers that can broaden the narrow spectrum emitted by most MLL to a full octave of frequencies through non-linear processes such as self-phase modulation, in what is called *supercontinuum generation* [20]. These fibers along with the dynamics involved will be further discussed in Chapters 3 and 5.

20 years of frequency comb

Before 2000, the common method to access an optical frequency was by knowing the speed of light and using optical wavemeters to measure wavelengths with a relative precision of 10^{-7}, which is much lower than the standards required nowadays for testing QED in high-precision spectroscopy experiments. The first attempts to directly measure optical frequencies were made with harmonic frequency chains [21–23], which were highly complex and large experiments aimed to connect the 9.2 GHz Cs standard to the optical range through a series of nonlinear frequency multiplications, phased-locked at each step to different oscillators. The finest of these frequency chains needed up to 10 scientists, 20 different oscillators and 50 feedback loops in two laboratories in two different buildings to work [24]! Because of their complexity, these systems would hardly ever become widely available, and only one or two high precision optical measurements could be performed per year. The arrival of the optical frequency comb would eventually substitute the large frequency chains by a single mode-locked laser of the size of a shoe-box, that can connect the microwave standard with the optical range in a single step.

The capacity to connect the optical and radiofrequency domains, as well as the ability to measure absolute optical frequencies with unprecedented precision, made the optical frequency comb quickly accomplish its original goals in precision spectroscopy, and time and frequency metrology. Public recognition for this technology was granted in 2005, when John L. Hall and Theodor W. Hänsch were awarded with half[1] of the Nobel Prize in Physics "for their contributions to the development of laser-based precision spectroscopy, including the optical frequency comb technique" [25, 26].

The first all-optical atomic clock was build in 2001 by Diddams et al. [27], and in the last 15 years vast optical fiber networks have been expanded over Europe to connect and compare ensembles of optical atomic clocks, and eventually realize a redefinition of the SI second [28–30]. What few people could have foreseen, is the amount of different applications the optical frequency comb has found in these 20 years since its invention [13, 31]. For instance, the direct relation between the optical and microwave domains does not only allow optical stabilization from a highly stable microwave source, but also the generation of *ultra-low-noise microwaves* by using the same idea "in reverse", referencing the comb to a high-stability optical source to generate a microwave signal with a stability of 10^{-15}, which is a 100 times better than the best room-temperature electronic oscillators [32].

[1] The other half was granted to Roy J. Glauber "for his contribution to the quantum theory of optical coherence."

Other applications range from the study of time variations in fundamental constants such as the fine structure constant [33–36], searches for ultralight dark matter [37, 38], synthesis of single cycle and attosecond pulses [39], calibration of astronomical spectrographs for the search of exoplanets [40–42], and precision distance measurements with LIDAR systems [43, 44].

There has also been much progress in the technology and architecture of optical frequency comb themselves. Ti:Sapphire lasers have been one of the most used frequency comb systems [45], even though nowadays the different erbium-doped fiber MLL emitting in the 1550 nm (telecommunications) region are very widespread and commercially available from different companies [46–48]. These Er-doped systems are so robust, they have even been operated on board a space rocket [49]. Another notable case is that of the Yb-doped lasers, which are promising systems for XUV frequency comb generation via high-harmonic generation from their high power 1 μm emission [50]. There are also different approaches to the optical frequency comb that do not use MLL, such as electro-optic frequency combs and microresonator frequency combs [51–53]. The latter opens the door to microcombs integrated in semiconductor chips, that may one day bridge the gap even closer between optics and electronics in everyday technological applications.

All in all, spectroscopy was, and still is, one of the main applications of optical frequency combs [54]. They can either be used as precise optical references for spectroscopic CW lasers, or conversely, they can be used directly to excite or probe a sample. This second approach is usually referred to as *direct frequency comb spectroscopy* (Fig 1.3). The f-2f interferometer built in this work is used for stabilizing an Yb:KYW mode-locked laser, which will eventually serve for generating an extreme ultra-violet (XUV) frequency comb to be used in direct spectroscopy of the 1S-2S two-photon transition in He^+.

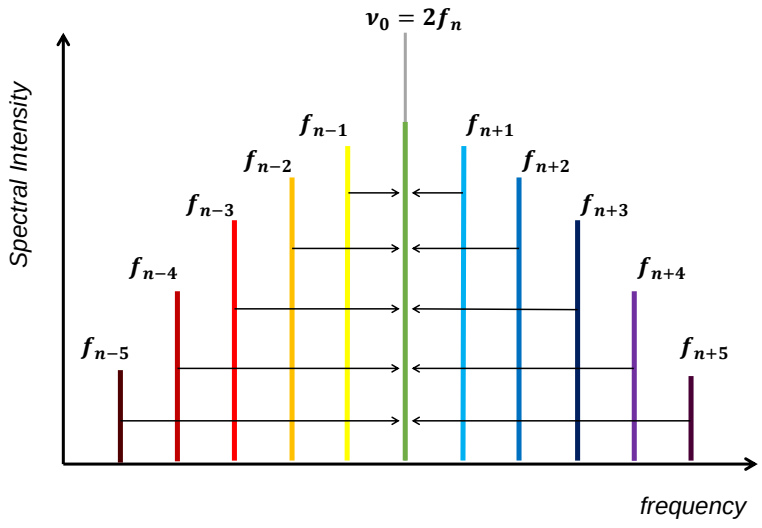

Fig. 1.3. Representation of direct comb spectroscopy in a two-photon transition. The use of a frequency comb for exciting a two-photon transition is just equivalent to that of a CW with the same average power. This is due to the fact that, if a single optical line is resonant to the two-photon transition, i.e. $\nu_0 = 2f_n = 2(nf_r + f_0)$, the pairs of modes that are symmetrically (red- and blue-) detuned from the resonance also sum up to the same resonance frequency $[(n + n')f_r + f_0] + [(n - n')f_r + f_0] = 2f_n = \nu_0$, and consequently the whole power of the comb contributes to the excitation. If two counter-propagating combs are used, the excitation can be made Doppler-free.

Chapter 2

Yb:KYW optical oscillator

Before presenting the work that was specifically developed for this Master's Thesis, we will go through a brief description of the Yb:KYW oscillator, the element that was taken as the starting point for the rest of this work. Some concepts and theoretical tools discussed in this short chapter, such as the main characteristics describing light pulses and their propagation dynamics, will be explained in detail in Chapter 3 and others. The reader that is not acquainted with them may prefer to read those first.

2.1 Kerr-lens mode-locking

The pulsed operation of the laser is achieved through **Kerr-lens mode-locking**. In general, mode-locking is a group of techniques that either actively or passively ensure the formation of an ultra-short pulse that circulates in the optical cavity. For correct operation in a steady-state, the various effects that provoke changes in the pulse parameters must be compensated. These are fundamentally dispersion and non-linear effects that cause the pulse shape and spectrum to distort, unless their net combined effect is appropriately balanced in each round trip. When the pulse reaches the output coupler every round-trip time T_r, a copy of the pulse is transmitted, generating an output consisting of a train of pulses emitted with a repetition rate $f_r = T_r^{-1}$. In this manner, all pulses are practically identical, preserving the same shape and spectrum, and only differ in their carrier-envelope phase, which slips by a constant amount $\Delta\varphi_{\mathrm{CE}}$ from pulse to pulse, as explained in the Introduction, and leads to the offset frequency f_0 in the frequency comb.

Passive mode-locking is often achieved by the introduction of a saturable absorber in the optical cavity. The basic idea is that the saturable absorber introduces losses in the cavity that prevent the laser from operating in a CW mode, but when a pulse with higher peak intensity hits the absorber, it saturates it and momentarily reduces losses in the cavity, enabling lasing in a pulsed fashion. Kerr-lens mode-locking acts similarly, but instead of introducing losses, it increases the net gain thanks to *Kerr lensing* in the gain medium. This self-focusing effect occurs by means of the intensity dependent refractive index $n(I) = n_0 + n_2 I$. When a pulse travels through a non-linear medium (i.e. a medium with sufficiently large n_2), its radially decreasing intensity profile modulates the index of refraction in the material in a similar shape. This gradient in the index of refraction deforms the pulse wavefront and effectively creates a lens that focuses the pulse while it propagates in the medium, reducing its radius or waist, and consequently increasing its peak intensity.

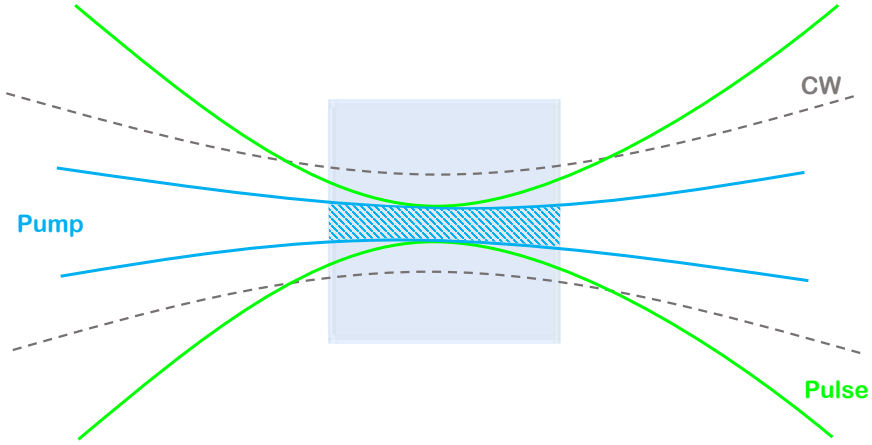

Fig. 2.1. Schematic representation of Kerr-lens mode-locking. The shaded area represents the overlap between the pump and the laser light, which limits the active region in the gain medium, and thus the net gain. A pulsed beam with higher peak intensity with respect to a CW field with the same average power will self-focus through Kerr-lensing, improving its overlap with a tightly focused pump, i.e. concentrating more energy in the active region.

To understand why this mode-locks the laser, it is useful to explain it in terms of the laser gain. The non-saturated gain depends on the spatial overlapping of both the pump and laser intensity profiles

$$g \sim \int_0^\infty I(r) I_p(r) r \mathrm{d}r \, . \tag{2.1}$$

If one tightly focuses the pump beam at the crystal, leading to a very narrow waist and abrupt intensity gradient, the overlapping with the lasing light becomes sharp. When a pulse is focused via Kerr-lensing, its waist shrinks, its overlapping with the pump profile improves and the gain increases. Note that it is not only the overlapping area that counts, but the light's intensity or energy density in that area, that increases when the beam waist is reduced. We therefore have a method for mode-locking and generating ultra-short pulses.

So far we have discussed mode-locking when a pulse is already circulating in the cavity, but an obvious question arises when one wonders how is the first pulse generated. This sort of laser usually starts operating in a CW mode after turning on the pump. Any random peak appearing in the flat intensity profile due to noise, may be amplified in the gain medium, eventually leading to the pulse formation. When a pulse passes through the gain medium and is amplified, it depletes the upper laser level and thus effectively rises the lasing threshold, preventing CW operation. In other words, the energy that was initially used for CW lasing is compressed in short periods and used for pulsed operation, which means simultaneous CW and pulsed lasing is only possible for very high pump power. If this process does not occur spontaneously (self-starting mode-locking), manual action to create a perturbation in the intensity may be needed, usually by knocking on one of the mirrors or by introducing some vibration in it.

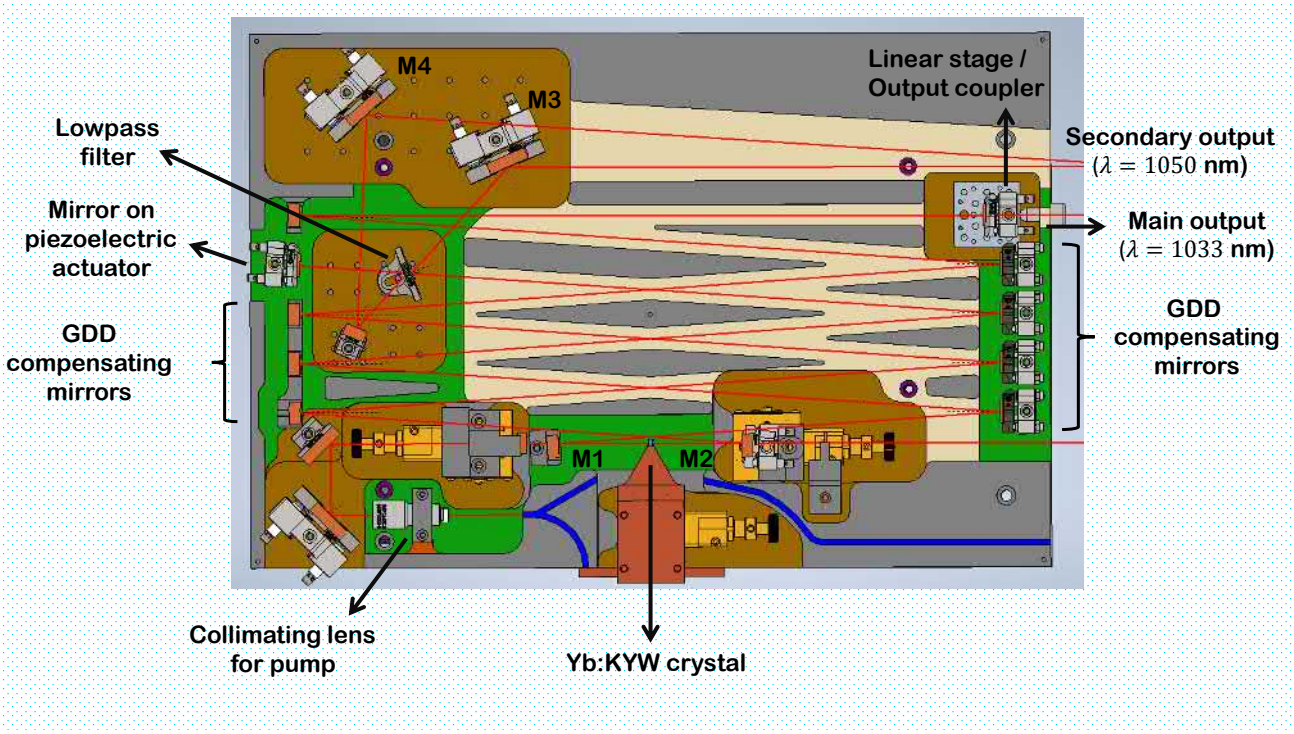

Fig. 2.2. Yb:KYW oscillator layout. Two focusing mirrors M1 and M2 tightly focus the laser diode's collimated pump into the Yb:KYW crystal for Kerr-lens mode-locking. The generated pulses travel along a set of dispersion (GDD) compensating mirrors to preserve the pulse's properties after each round trip. A piezoelectric transducer and a linear stage act on two movable mirrors that control the cavity length. A lowpass filter forces laser operation at 1033 nm and extracts a secondary output at 1050 nm (M3 and M4), which will be used for f-2f self-referencing. The main output is emitted through a 1% output coupler and consists of a 40 MHz - 100 fs pulsed laser beam at 1033 nm.

2.2 Cavity layout

The schematic setup can be seen in Fig. 2.2. This setup composes a diode-pumped solid-state femtosecond laser, with Yb:KYW (ytterbium-doped potassium yttrium tungstate) as its gain medium. The 10-at.% Yb:KYW crystal, commercially available from Altechna, has a size of $3 \times 4 \times 2$ mm in its N_p, N_m and N_g axes respectively, and it is AR (anti-reflection) coated. The pump and laser light fields are polarized parallel to the N_m axis, and are propagating through the N_g one. The pump light is provided by a laser diode at 981 nm, which coincides with a sharp absorption peak in Yb:KYW, and allows for laser emission in a broad band around 1020 - 1060 nm. The diode's output is collimated and tightly focused into the crystal, which is mounted on a linear stage for fine tuning its position.

The optical cavity is arranged in a linear configuration, meaning the light travels the same path to go from the crystal to the output coupler and back. For compensating the dispersion and ensuring constant pulse properties, a set of seven flat mirrors is used with appropriate GDD values[1]. The use of such number of mirrors allows for a longer (yet compact) cavity length, which sets the repetition rate f_r around 40 MHz. The cavity length can be tuned by two movable mirrors, one mounted on a linear stage for a long range - slow response, and another one mounted on a piezoelectric

[1]GDD stands for group-delay dispersion and we will discuss its effects further in Chapter 3.

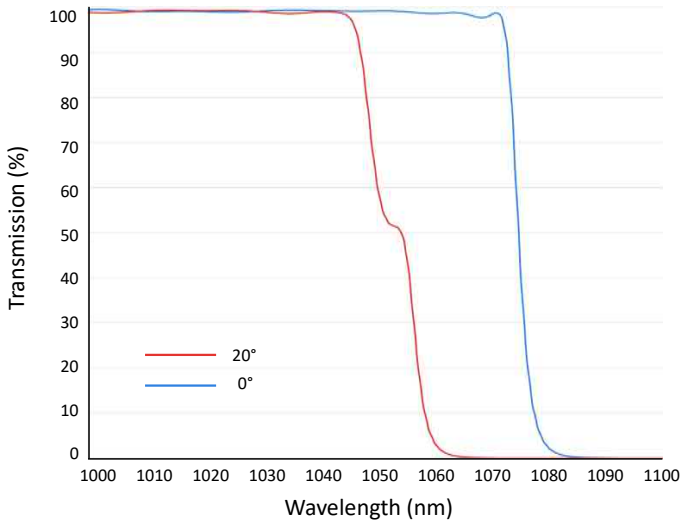

Fig. 2.3. Transmission spectrum for the 1075 OD4 SP Filter from Alluxa at 0° and 20° angle of incidence of a collimated beam. This optical low-pass filter has an angle-dependent cut-off wavelength, such that by tilting it one can obtain the desired performance with maximum transmission at 1033 nm. Adapted from the manufacturer's data.

actuator for a short range - fast response. The mirror mounted in the linear stage is precisely the output coupler, which has a 99% reflectivity from 980 nm to 1100 nm.

For its application in He^+ spectroscopy, the main output is set to 1033 nm. The Yb:KYW tends to emit closer to 1040 nm, so a shorter wavelength is obtained by means of a low-pass filter, whose cut-off edge can be tuned by tilting its angle relative to the incident beam (see Fig. 2.3). This is done in such a way that transmission at 1033 nm is maximized ($\sim$ 99%), and there is partial reflectivity around 1050 nm. The 1033 nm transmitted light hits the piezo-controlled mirror and is reflected back to the "main cavity path", while the light around 1050 nm is eventually expelled from the cavity by sending it towards the M3 and M4 mirrors. This causes the intracavity mode's spectrum to shift and narrow at 1033 nm, and this is what comes out the main output. The secondary output, centered at 1050 nm is used for f-2f self-referencing. This configuration allows for a 10 mW main output with a spectrum centered at 1033 nm and a FWHM $=$ 10 nm, and a 60 mW secondary output at 1050 nm and a 10 nm FWHM width. In fact, the secondary output is in principle composed of two beams, from mirrors M3 and M4, but only one of them is used for practical reasons. The achieved pulse duration is approximately 100 fs. The pulse shape from the main output and its spectrum measured by the FROG (*Frequency Resolved Optical Gating*) method[2] are shown in Fig. 2.4 and the spectrum of the secondary output measured with a regular spectrometer is shown in Fig. 2.5.

2.3 Acting on f_r and f_0

Our ultimate goal is to measure and control the frequency comb's offset frequency f_0. For this, it is necessary to understand what physical parameters in the optical oscillator affect f_0. A variation of the cavity length L readily changes the repetition rate, but leaves the offset frequency almost unchanged. On the other hand, it can

[2]We will describe the FROG method in Chapter 4.

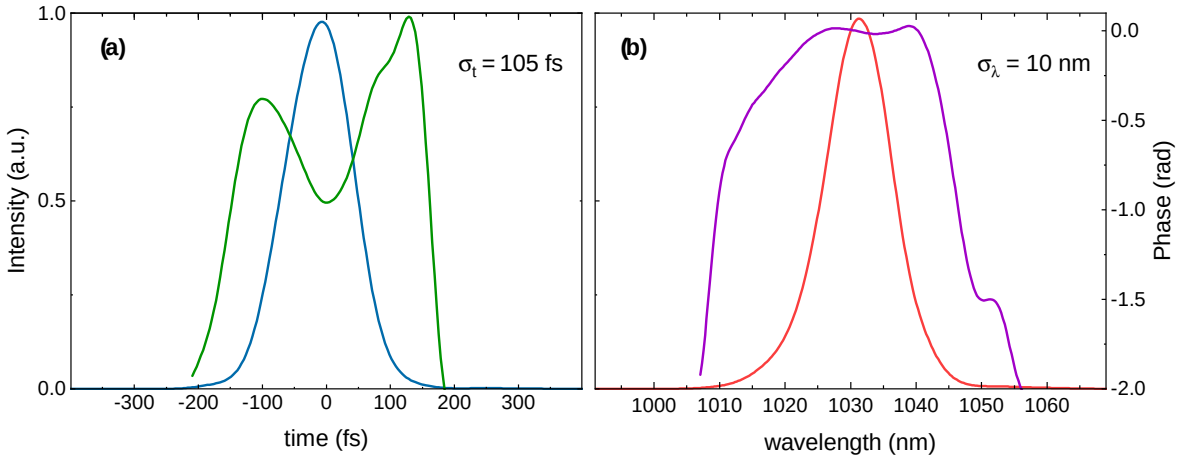

Fig. 2.4. Intensity and phase of the main output of the Yb:KYW oscillator in both (a) time (pulse-shape) and (b) frequency (spectrum) domains. The pulse shape (blue) forms a quasi-gaussian peak with a duration $\sigma_t = 105$ fs, which gives a quasi-gaussian spectrum (red) centered at 1033 nm with a $\sigma_\lambda = 10$ nm bandwidth. The spectral phase (purple) seems to be dominated by a quadratic component, even though its top flattens at the maximum of the spectrum. This means the pulses come rather linearly chirped out of the cavity, hence the different spectral components are temporally distributed along the pulse and its duration is not strictly Fourier-limited. Data from FROG measurements.

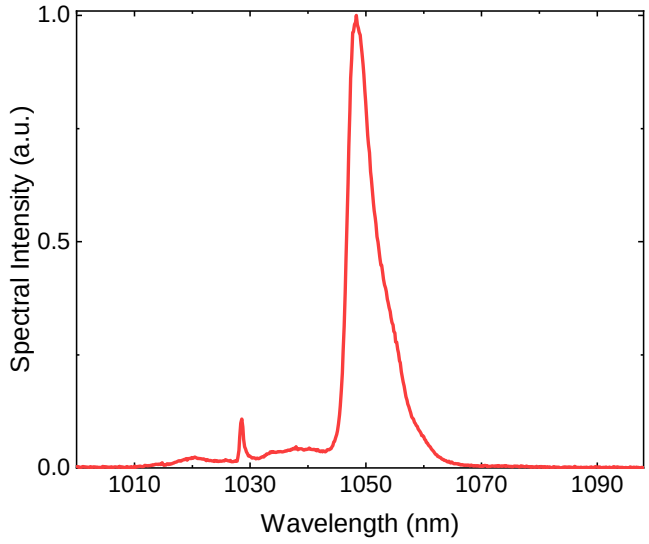

Fig. 2.5. Spectrum measured at the secondary output of the Yb:KYW oscillator. Due to the action of the low-pass filter, this spectrum has a strong component centered at 1050 nm, but also a weak contribution at $\sim$ 1028 nm. This is the spectrum that is sent towards the f-2f interferometer for measuring f_0 and self-referencing the frequency comb, after appropriate amplification and spectral broadening.

be shown that the intensity of the laser acts on both parameters through the aforementioned Kerr effect. These two frequencies, which represent the two degrees of freedom of the comb, can be expressed as $f_r = v_g/2L$ and $f_0 = \frac{\omega_c}{2\pi}\left(1 - \frac{v_g}{v_p}\right)$ [55], where ω_c is the carrier or central frequency, and v_g and v_p are the *group* and *phase* velocities, defined as $v_g = c\left[\bar{n} + \omega_c\left(\frac{\mathrm{d}\bar{n}}{\mathrm{d}\omega}\right)_{\omega_c}\right]^{-1}$ and $v_p = c/\bar{n}$. Here, $\bar{n} = \bar{n}_0 + \bar{n}_2 I$ is the average refractive index in the cavity, and thus $\bar{n}L$ is the optical path length throughout the cavity. It is therefore straightforward to see how an intensity dependent index of refraction leads to intensity dependent group and phase velocities, and consequently to a variation of both f_r and f_0. A more detailed description of the intensity related dynamics can be found in e.g. [55, 56], but what is clear is that one can use the pump power to change the intensity of the emitted light (within the the limits imposed by mode-locking) and thus control the degrees of freedom of the frequency comb. If one sends feedback to the cavity length to control either f_r or the frequency of one optical mode f_n, then the offset frequency can be controlled by acting on the optical pump power, and that is precisely what we will do in this work.

Chapter 3

Ultra-short pulses

When talking about ultra-short pulses, one usually refers to femtosecond light pulses. These are fully characterised by their space and time dependent electric field, and their dynamics are governed by the well-known Maxwell's equations. Due to their high peak-intensity, these sort of pulses are very useful for exploiting nonlinear optical phenomena. Throughout this chapter we will introduce and define the main quantities that describe a light pulse, relating them with experimentally measurable parameters. We will put special effort in describing the interaction of these pulses with matter in a classical framework, in which a macroscopic polarization with linear and nonlinear contributions in the field amplitude will significantly shape the pulses during their propagation in material elements such as optical fibers. Understanding these dynamics and how to use them to our advantage is a key step in the stabilization of the frequency comb, as one needs to generate an optical spectrum wide enough to span an octave of frequencies to perform f-$2f$ interferometry, which is usually not readily available from most laser systems. Numerical methods for the simulation of propagation of pulses in matter are described and implemented, eventually considering realistic parameters for supercontinuum generation and octave-spanning.

3.1 Theoretical background

3.1.1 Characteristics of light pulses

Light pulses are electromagnetic wave-packets characterised by their electric field, with its corresponding space, time and polarization dependencies. For the moment, and without loss of generality, we can describe the electric field as a complex quantity dependent on time only. Keeping in mind that the physical electric field is real, we define it as

$$E(t) = \frac{1}{2}\tilde{\mathcal{E}}(t)e^{i\omega_c t} + \text{C.C.} = E^+(t) + E^-(t)\ , \tag{3.1}$$

where ω_c is the *carrier* frequency and $\tilde{\mathcal{E}}(t)$ is the complex *envelope*, characterised by its **amplitude** and **phase**

$$\tilde{\mathcal{E}}(t) = \mathcal{E}(t)e^{i\varphi(t)+\varphi_0}\ . \tag{3.2}$$

The envelope determines the temporal width and shape of the pulse, and it is typically parametrized as a gaussian or a sech function, even though it can take any

arbitrary form. The constant phase term with φ_0 is commonly neglected since it is actually hard to define in a single pulse, but the pulse-to-pulse carrier-to-envelope (CE) phase difference $\Delta\varphi_{\mathrm{CE}}$ plays a relevant role and is the origin of the frequency offset f_0 in a frequency comb.

Let us pay some special attention to the phase of the electric field and its physical meaning. We have implicitly defined with respect to the carrier frequency as $\Phi(t) = \varphi(t) + \omega_c t$[1], which means the instantaneous frequency is

$$\omega(t) = \frac{\mathrm{d}\Phi(t)}{\mathrm{d}t} = \omega_c + \frac{\mathrm{d}\varphi(t)}{\mathrm{d}t} \,. \tag{3.3}$$

This is a clear way of seeing how the frequency can vary inside the pulse, or in other words, how the frequency components of the pulse can be temporally distributed. When $\mathrm{d}\varphi(t)/\mathrm{d}t$ is constant, then Eq. 3.3 just adds a correction to the carrier frequency $\omega_c' = \omega_c + \omega_0'$, demonstrating that an appropriate choice of ω_c minimizes or eliminates the envelope's phase variation. On the other hand, when $\mathrm{d}\varphi(t)/\mathrm{d}t$ is a function of time, the carrier frequency increases or decreases along the pulse, and the pulse is said to be *up* or *down chirped* respectively. The simplest and very common case happens when $\varphi(t)$ varies quadratically in time and thus the pulse is linearly chirped.

Intensity and Power: from single pulses to a laser beam

From the characteristics of single pulses, one should be interested in describing those of laser beams, since these are what we work with and can measure in a lab. Thus, we can begin by describing some instantaneous quantities such as intensity and power in terms of single pulse parameters, and then average them in time over the number of pulses per second, i.e. the repetition rate f_r, in a beam. Since electronic detectors are not fast enough to resolve optical oscillations, we define the instantaneous intensity as averaged over an optical cycle $T = 2\pi/\omega_c$, in units of energy per time per surface, usually $[\mathrm{W/cm^2}]$ [2]

$$I(t) = \epsilon_0 c n \frac{1}{T} \int_{t-T/2}^{t+T/2} \left|E(t')\right|^2 \mathrm{d}t' = \frac{1}{2}\epsilon_0 c n |\mathcal{E}(t)|^2 \,, \tag{3.4}$$

where n is the index of refraction of the propagation medium. The instantaneous power is obtained by integrating the intensity over the cross section of the beam

$$P(t) = \int_S \mathrm{d}S I(t) = \epsilon_0 c n \int_S \mathrm{d}S \frac{1}{T} \int_{t-T/2}^{t+T/2} \left|E(t')\right|^2 \mathrm{d}t' \,. \tag{3.5}$$

Note that in general, the intensity profile is space-dependent $I(\mathbf{r}, t)$. In fact, the fundamental transverse mode in an optical cavity corresponds to a Gaussian profile, but many other forms are possible.

Now, we can average Eqs. 3.4 and 3.5 in time over the number of pulses per second f_r to obtain the average power and intensity that characterise the laser beam as we measure it in the lab:

[1] Do not confuse the envelope's phase $\varphi(t)$ with the electric field's phase $\Phi(t)$

[2] This definition can be traced back to Poynting's theorem

$$\bar{I} = \frac{1}{2}\epsilon_0 c n f_r \int_{-\infty}^{\infty} \mathrm{d}t |\mathcal{E}(t)|^2 \tag{3.6}$$

$$\bar{P} = \frac{1}{2}\epsilon_0 c n f_r \int_S \mathrm{d}S \int_{-\infty}^{\infty} \mathrm{d}t |\mathcal{E}(t)|^2 \,. \tag{3.7}$$

Lastly, if one was interested in knowing the energy per pulse, they would only need to divide the average power $\bar{P}$ by the repetition rate.

Spectral representation

So far, we have constructed a description of the main parameters that describe the light pulses with time as the main argument, i.e. in the time domain. Equivalently, we could choose to describe our pulses in the frequency or spectral domain. As conjugate variables, time and frequency domains are related through the Fourier transform $\mathcal{F}$, and thus one can express the spectrum of the complex electric field as

$$E(\omega) = \mathcal{F}\{E(t)\} = \int_{-\infty}^{\infty} E(t) e^{-i\omega t} \mathrm{d}t \,, \tag{3.8}$$

which, in terms of the complex envelope function is

$$\begin{aligned} E^+(\omega) &= \int_{-\infty}^{\infty} \frac{1}{2}\tilde{\mathcal{E}}(t) e^{-i(\omega-\omega_c)t} \mathrm{d}t \\ &= \frac{1}{2}\tilde{\mathcal{E}}(\omega-\omega_c) \\ &= \frac{1}{2}\mathcal{E}(\omega-\omega_c) e^{i\gamma(\omega)} \,. \end{aligned} \tag{3.9}$$

Here, he have defined the spectral envelope and phase, and we have seen how naturally the spectral envelope is evaluated at the carrier frequency ω_c.

In a similar manner, we can define the *spectral intensity* as

$$S(\omega) = \frac{\epsilon_0 c n}{4\pi} \left|\tilde{\mathcal{E}}(\omega-\omega_c)\right|^2 \,. \tag{3.10}$$

Commonly one talks about the "spectrum" of light, which can be measured with a spectrometer or optical spectrum analyzer, and this usually refers to a graphical representation of the spectral intensity (often in logarithmic scale) as a function of frequency.

Pulse duration and spectral width

There is no unique way of defining the duration of a pulse $\Delta\tau$, but it is common to describe it as the FWHM of the intensity profile $\left|\tilde{\mathcal{E}}(t)\right|^2$. A similar definition can be made for the bandwith $\Delta\omega$ of the spectral intensity profile $\left|\tilde{\mathcal{E}}(\omega)\right|^2$, even though

in many practical cases the spectrum can have an intricate structure that may require a re-definition of the spectral width for that particular case. The Fourier duality between temporal and spectral characteristics of the pulse leads to a minimum duration-bandwidth product [57]

$$\Delta\omega\Delta\tau \geq 2\pi c_B \, . \tag{3.11}$$

c_B is a numerical constant on the order of the unit that depends on the specific shape of the pulse. Pulses that satisfy the minimum product equality, meaning they have the minimum duration for a given spectrum, are said to be *Fourier-limited*. This condition is accomplished when the pulse's phase is flat or linear in time, and the pulse is thus un-chirped, so that its frequency components are not distributed along the pulse.

3.1.2 Propagation of pulses in dispersive media

A pulse of light propagating through a medium will create a response in that medium that ultimately depends on the amplitude of the light's electric field, in either a linear or nonlinear manner. This response is represented by a macroscopic polarization

$$\mathbf{P}(\mathbf{r},t) = \mathbf{P}_{\mathrm{L}}(\mathbf{r},t) + \mathbf{P}_{\mathrm{NL}}(\mathbf{r},t) \tag{3.12}$$

that is induced by the electric field through a causal and local response function known as the electric susceptibility

$$\mathbf{P}_{\mathrm{L}}(\mathbf{r},t) = \epsilon_0 \int_{-\infty}^{\infty} \chi^{(1)}(t-t') \cdot \mathbf{E}(\mathbf{r},t')\mathrm{d}t' \tag{3.13}$$

$$\mathbf{P}_{\mathrm{NL}}(\mathbf{r},t) = \epsilon_0 \int_{-\infty}^{\infty} \chi^{(3)}(t;t_1,t_2,t_3) \vdots \mathbf{E}(\mathbf{r},t_1)\mathbf{E}(\mathbf{r},t_2)\mathbf{E}(\mathbf{r},t_3)\mathrm{d}t_1\mathrm{d}t_2\mathrm{d}t_3 \, . \tag{3.14}$$

In this work, we are mostly interested in the propagation of pulses in optical fibers, and for this reason the nonlinear polarization depends directly on $\chi^{(3)}$. This is so because $\chi^{(2)}$, responsible for phenomena such as second-harmonic generation or sum-frequency generation, vanishes in materials with inversion symmetry, as it is the case of common silica (SiO_2) fibers, even though some weak second order effects may arise due to imperfections or color centers in the fiber core. The interaction of the light pulses with the medium will therefore change the properties of both the pulse and the medium, and these quite complicated dynamics are governed by Maxwell's equations, from which one can obtain the following wave equation:

$$\left(\nabla^2 - \frac{1}{c^2}\frac{\partial^2}{\partial t^2}\right)\mathbf{E}(\mathbf{r},t) = \mu_0 \frac{\partial^2}{\partial t^2}\mathbf{P}(\mathbf{r},t) \, . \tag{3.15}$$

Solving Eq. 3.15 requires appropriate knowledge of the linear and nonlinear response functions, and since that is usually inaccessible, this problem is commonly treated in a perturbative manner, such that different effects and contributions may be accounted for. A proper discussion can be found in textbooks such as Agrawal's [58], so here a more applicable form of the propagation equation will be presented

directly, in terms of the slowly-varying pulse envelope $\mathcal{E}(t)$ and assuming spatial dependence only along the propagation axis z:

$$\frac{\partial \mathcal{E}(t)}{\partial z} + \beta_1 \frac{\partial \mathcal{E}(t)}{\partial t} + \frac{i\beta_2}{2}\frac{\partial^2 \mathcal{E}(t)}{\partial t^2} + \frac{\alpha}{2}\mathcal{E}(t) = i\gamma(\omega_c)|\mathcal{E}(t)|^2\mathcal{E}(t)\ . \tag{3.16}$$

It must be noted that, in Eq. 3.16, the temporal variation of $\mathcal{E}(t)$ and $\varphi(t)$ is assumed to be small within an optical cycle $T = 2\pi/\omega_c$. This is known as the *slowly-varying envelope approximation* (SVEA), and in terms of the complex pulse envelope is expressed as

$$\left|\frac{\mathrm{d}}{\mathrm{d}t}\tilde{\mathcal{E}}(t)\right| << \omega_c\left|\tilde{\mathcal{E}}(t)\right|\ . \tag{3.17}$$

This also means that the bandwith of the pulse is be very narrow around the carrier frequency $\Delta\omega/\omega_c << 1$.

Today, pulses with only a few optical cycles or even single-cycle pulses can be generated, so one has to be careful as to when to describe the pulse in terms of a slowly varying envelope and a phase as we are doing.

Linear Effects: Group-velocity dispersion

Let us describe Eq. 3.16 in detail. The left-hand side gathers all the terms that are linear in the field amplitude. Losses are accounted for through α, and chromatic dispersion through β_1 and β_2. Chromatic dispersion means that different spectral components travel at different velocities because of the frequency dependency of the index of refraction $n(\omega)$, which makes the spectral components spread over time, effectively stretching or broadening the pulse.

In this context, one can define a so-called mode-propagation function $\beta(\omega) = n(\omega)\omega/c$ and expand it in a Taylor series centered at the carrier frequency ω_c, where β_1, β_2, β_3... are its Taylor components. Therefore, chromatic dispersion is treated too in a perturbative way and its coefficients describe different features of linear pulse propagation. In short, the envelope propagates at a **group velocity** $v_g = 1/\beta_1$ and its dispersion is described by the **group-velocity dispersion** (GVD) represented by β_2. Higher order terms add further effects, like β_3, related to the **third-order dispersion** (TOD) that introduces temporal asymmetry in the pulse. These effects will be further discussed in the Results section.

GVD is the main factor responsible for stretching pulses in dispersive media, such as optical fibers, which means the duration of the pulses after propagation in such elements can be considerably longer, depending on the β_2 parameter and length of the specific medium. This is understood again thinking on the frequency dependent accumulated phase over a distance z

$$\varphi_D(\omega, z) = \frac{i}{2}\beta_2\omega^2 z\ . \tag{3.18}$$

When the pulses get broader, and since energy is conserved within the pulse[3], their peak intensity is reduced accordingly, and their nonlinear interaction with the medium

[3] neglecting absorption or losses in the medium

will decrease, which may be in detriment of the interests of the experiment. For this reason, techniques such as pulse compression are commonly used to compensate the dispersion introduced by optical fibers, as we will see in Chapter 4.

Nonlinear effects: Self-phase modulation

Nonlinear effects in optical fibers stem from the third order susceptibility $\chi^{(3)}$, which is related to the nonlinear refractive index, i.e. the variation of the refractive index with the intensity of the light propagating in a medium, also known as the *Kerr effect*.

$$n(\omega) + n_2 I = n(\omega) + \bar{n}_2 |E|^2 \,. \tag{3.19}$$

The right-hand side of Eq. 3.16 accounts for the main nonlinear contribution to the propagation dynamics, namely **self-phase modulation** (SPM), which is weighted by a *nonlinear coefficient* $\gamma(\omega)$, that is specific of each material. Self-phase modulation introduces a time-dependent phase in the pulse after a propagation distance z

$$\varphi_{\mathrm{NL}}(t,z) = \gamma |\mathcal{E}(t)|^2 z \,. \tag{3.20}$$

This phase shift does not stretch the pulse envelope in time domain, but it does broaden the spectral envelope. By generating new frequencies and keeping the time width constant, the frequency chirp introduced in the pulse translates into a broader spectral width. As a matter of fact, this is the main mechanism that we use for spanning an octave of frequencies in the f-$2f$ interferometer.

Higher order terms in the field amplitude can be added, leading to phenomena like *stimulated Raman* and *Brillouin* scattering, but we will not consider them here.

3.2 Numerical methods: Split-step Fourier method

The scope of this section is to explain the method by which we will numerically solve Eq. 3.16, or a very similar one. A numerical approach is needed because the propagation equation is a differential equation that does not have an analytic solution in general. For this, we will make use of the split-step Fourier method (SSFM) [58]. To understand this method easily, it is useful to express the propagation equation in the following way

$$\frac{\partial \mathcal{E}}{\partial z} = (\hat{D} + \hat{N})\mathcal{E} \,, \tag{3.21}$$

where $\hat{D}$ is a differential operator that comprises the linear terms accounting for dispersion, and $\hat{N}$ is a nonlinear operator that comprises nonlinearities in the propagation dynamics

$$\hat{D} = -i\frac{\beta_2}{2}\frac{\partial^2}{\partial t^2} + \frac{\beta_3}{6}\frac{\partial^3}{\partial t^3} \tag{3.22}$$

$$\hat{N} = i\gamma |\mathcal{E}|^2 \,. \tag{3.23}$$

Note that here we are considering the effects that are of most interest to us in understanding the propagation dynamics, which are GVD and potentially higher order dispersion terms, such as TOD; and SPM. Additionally, the t parameter here means time measured in a reference frame that moves with the pulse at the group velocity v_g (retarded frame)[4] A formal solution of Eq. 3.21 would be of the form

$$\mathcal{E}(z,t) = e^{(\hat{D}+\hat{N})z}\mathcal{E}(z,t)\ , \tag{3.24}$$

but the partial derivatives in time from $\hat{D}$ make this solution inadequate for practical computation. A way around this is to Fourier transform the $\hat{D}$ operator, so that the mapping $\partial_t \rightarrow -i\omega$ converts the differential expression in a simple algebraic one in the frequency domain. For this purpose, we would like $\hat{D}$ and $\hat{N}$ to act independently on the envelope $\mathcal{E}$, even though this is not true since these are non-commuting operators. In fact, one should formally use the Baker-Campbell-Hausdorff (BCH) formula

$$\exp(\hat{D}z)\exp(\hat{N}z) = \exp\left(\hat{D}z + \hat{N}z + \frac{1}{2}[\hat{D},\hat{N}]z^2 + \dots\right)\ , \tag{3.25}$$

where $\left[\hat{A},\hat{B}\right] = \hat{A}\hat{B} - \hat{B}\hat{A}$. As a first approximation, we can let $\hat{D}$ and $\hat{N}$ act independently, i.e. to commute, in small split steps, so that the higher order terms in z in the BCH expansion can be neglected. This means that after a small step h, the envelope propagates as

$$\mathcal{E}(z+h,t) \approx e^{\hat{D}h}e^{\hat{N}h}\mathcal{E}(z,t) \tag{3.26}$$

and in each of these steps, we can evaluate the action of $\hat{D}$ in the frequency domain via Fourier transform, and then transform back to the time domain so that

$$e^{\hat{D}h}\mathcal{E}(z,t) = \mathcal{F}^{-1}e^{\hat{D}(\omega)h}\mathcal{F}\mathcal{E}(z,t)\ . \tag{3.27}$$

Subsequent application of this formula over the whole fiber length will lead to a pulse that will show features arising from linear and nonlinear effects in both time and frequency domains.

There is a simple modification to this protocol that can improve the accuracy of the results, and it is sometimes called the symmetrized SSFM. When propagating from z to $z+h$, instead of acting first with $\hat{N}$ and then with $\hat{D}$, one can do the following:

$$\mathcal{E}(z+h,t) \approx e^{\hat{N}\frac{h}{2}}e^{\hat{D}h}e^{\hat{N}\frac{h}{2}}\mathcal{E}(z,t)\ , \tag{3.28}$$

thus applying the nonlinear operator in the middle of the segment. By using the BCH formula twice in Eq. 3.28 one can easily see how the first order commutators ($\propto z^2$) vanish, and the leading error term is on the second order commutators ($\propto z^3$). Besides, implementation of this method is not substantially harder than that of Eq. 3.26, because by consequent application of Eq. 3.28 over a length L, the expression obtained is equivalent to

[4] That is why the term with β_1 does not appear on this equation.

$$\mathcal{E}(L,t) \approx e^{-\frac{h}{2}\hat{N}} \left(\prod_{m=1}^{M} e^{\hat{N}h} e^{\hat{D}h} \right) e^{\frac{h}{2}\hat{N}} \mathcal{E}(0,t) \ , \tag{3.29}$$

where $L = Mh$ is the total fiber length.

Several issues must be considered when computationally implementing this method. First, the time window $-T \leq t \leq T$ used for simulations must be sufficiently bigger than the pulse time width, keeping in mind the possible stretching. Also, the time resolution is set by the number of points N in the FFT algorithm that implements the Fourier transform, being $\delta t = 2T/N$, and the frequency resolution is in fact set by the time window

$$\delta\omega = \frac{2\pi}{\delta t}\frac{1}{N} = \frac{\pi}{T} \ . \tag{3.30}$$

Therefore, for a correct sampling of the pulse in both time and spectral domains, one would want δt and $\delta\omega$ to be small enough, which means having large N and T with the consequent increment in computation time. This means that a balance must be found, probably by trial and error. Another important issue is the choice of the step size h. In principle, the criterion is having a step small enough so that terms of order h^3 and higher can be safely neglected in the BCH formula. In practice, the step size can be varied in different simulations until the results converge, meaning if the step size is too large, the results may differ when changing h, but when it is sufficiently small, they will be independent of it.

3.2.1 Implementation of the method

The split-step Fourier transform method was implemented for this work in C++. A Fourier limited 100 fs Gaussian pulse was used as a seed to propagate over different distances for consistently showing the effects of linear and nonlinear propagation in a medium. Some characteristic lengths can be defined in terms of the β_2, β_3 and γ parameters, that represent the length from which their corresponding contributions (GVD, TOD and SPM) are more apparent.

$$L_{\mathrm{D}} = \frac{\tau_0^2}{|\beta_2|} \tag{3.31}$$

$$L_{\mathrm{TOD}} = \frac{\tau_0^3}{|\beta_3|} \tag{3.32}$$

$$L_{\mathrm{NL}} = \frac{1}{\gamma P_0} \tag{3.33}$$

where τ_0 is the pulse duration and P_0 the peak power. Therefore, when studying the interplay of these effects, comparing their characteristic lengths gives an idea of their relative contribution to the pulse dynamics. It must be noted that a simulation of linear or nonlinear effects only does not need the SSFM, and just propagation with the corresponding phases in either frequency (GVD) or time (SPM) domains is performed. Only when both linear and nonlinear effects are considered simultaneously the SSFM is fully exploited.

3.3 Results

3.3.1 Linear propagation with dispersion

We begin our simulations with a 100 fs Fourier limited Gaussian pulse, with a $T = 3$ ps time window and a $\delta t = 1$ fs resolution. The first phenomenon we would like to study is pulse broadening from GVD, and for that purpose we use Eq. 3.21 to propagate the pulse with only the term in β_2. This effectively means we can use Eq. 3.27 with an arbitrary step distance, equivalently to applying the SSFM for one large step. In other words, we Fourier transform the pulse, add a phase of the form $\frac{i}{2}\beta_2\omega^2 L$ to it, and Fourier transform back to the time domain. Doing this simulation for different values of L/L_D, with L_D as defined in Eq. 3.31, one can clearly see the effects of GVD symmetrically stretching the pulse (Fig. 3.1).

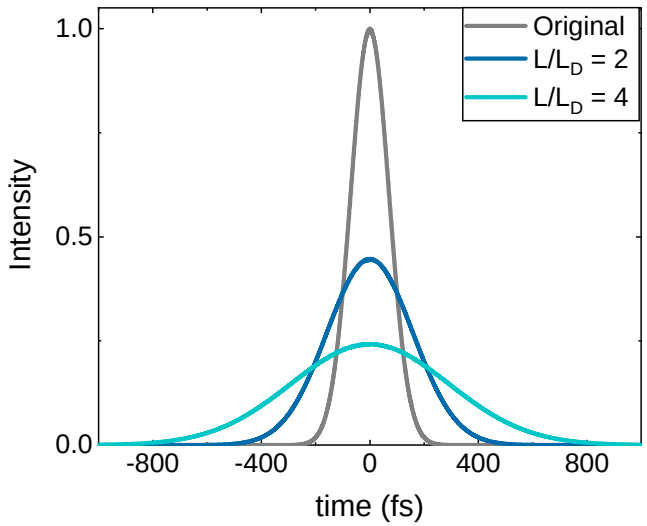

Fig. 3.1. Pulse broadening by the effects of GVD. Only considering the effects of GVD, A 100 fs Gaussian pulse is propagated over $L/L_D = 2$ and 4 showing a clearly increased duration. The integrated area is constant, meaning the pulse energy is conserved.

Note that the pulse energy is conserved, meaning that while the pulse broadens, the peak intensity decreases accordingly, so that the integrated area of the pulse remains constant. Furthermore, GVD broadens the pulse without distorting the pulse shape, i.e. the Gaussian envelope remains a Gaussian.

GVD is present in almost any occasion where a pulse propagates in a dispersive medium, and the broadening of the pulse can only be avoided by GVD-compensating mechanisms (pulse compressor), by propagation near the zero dispersion wavelength $\lambda_c \approx \lambda_D$ (where $\beta_2 \approx 0$) or in special conditions where GVD and SPM contribute to the pulse dynamics with opposite signs and exactly compensate each other so that the pulse travels without changing as a *soliton*. [5].

Next, we study the effects of TOD in exactly the same manner, but using only the term with β_3 in the propagation equation, meaning we add a phase in the frequency domain of the form $\beta_3\omega^3 L$. Propagating the pulse over different values of L/L_{TOD}, we obtain the results of Fig 3.2. TOD breaks the time symmetry in the pulse and introduces a distinctive oscillatory tail on one of its sides. These oscillations are deep and bring the intensity to zero on some points when GVD is not present, but

[5] This can happen in the so-called anomalous-GVD region, where $\lambda_c < \lambda_D$ and $\beta_2 < 0$.

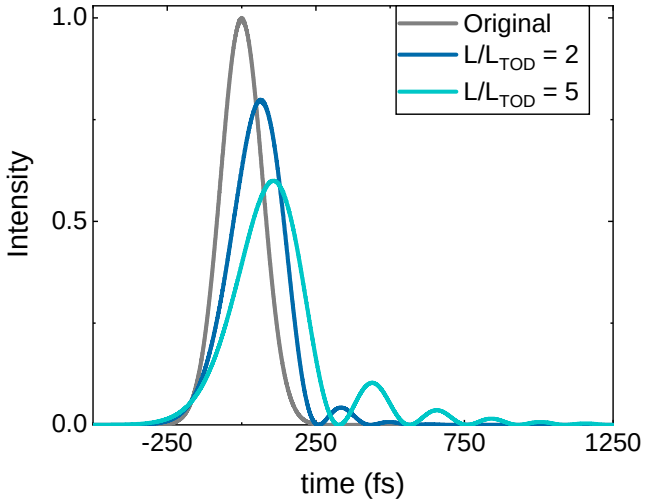

Fig. 3.2. Breaking of time-symmetry via TOD. A 100 fs Gaussian pulse is propagated over distances $L/L_{\mathrm{TOD}} = 2$ and 5, with the effects of TOD only. The pulse envelope shape changes asymmetrically, developing an oscillatory tail on one of its sides.

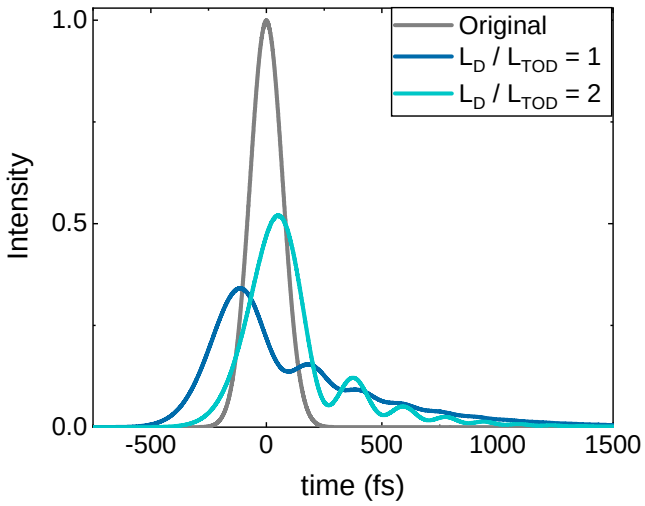

Fig. 3.3. Pulse propagated with combined effects from GVD and TOD. After propagation over $L = 5\ L_{\mathrm{TOD}}$, the pulse broadens more than with GVD alone, and asymmetrically, but the oscillations from TOD are smoothed. The relative importance of both effects is indicated by the ratio L_D/L_{TOD}.

are smoothed out when $\beta_2 \neq 0$. In Fig. 3.3 a simulation with both effects active is shown. The pulse is propagated through a distance $L = 5\ L_{\mathrm{TOD}}$, and the relative importance of the effects is represented by the ratio of their corresponding characteristic distances L_D / L_{TOD}.

When introducing some GVD to the case with TOD only, the oscillations on the pulse's tail see their relative amplitude reduced, and increasing the GVD parameter may smooth them out entirely, but keeps the asymmetry introduced by TOD. From another point of view, TOD increases the broadening introduced by GVD alone, but it does so asymmetrically.

3.3.2 Nonlinearities with SPM

In order to realize the effects of SPM, we set the dispersion parameters β_2 and β_3 to zero, and propagate the pulse by adding a phase $\exp\left(\hat{N}L\right)$ with $\hat{N} = i\gamma|\mathcal{E}(t)|^2$. This time, we will not look at the pulse envelope in time domain, which does not change, but at the spectrum or spectral intensity. The spectra shaped by SPM for different accumulated nonlinear phases are shown in Fig. 3.4.

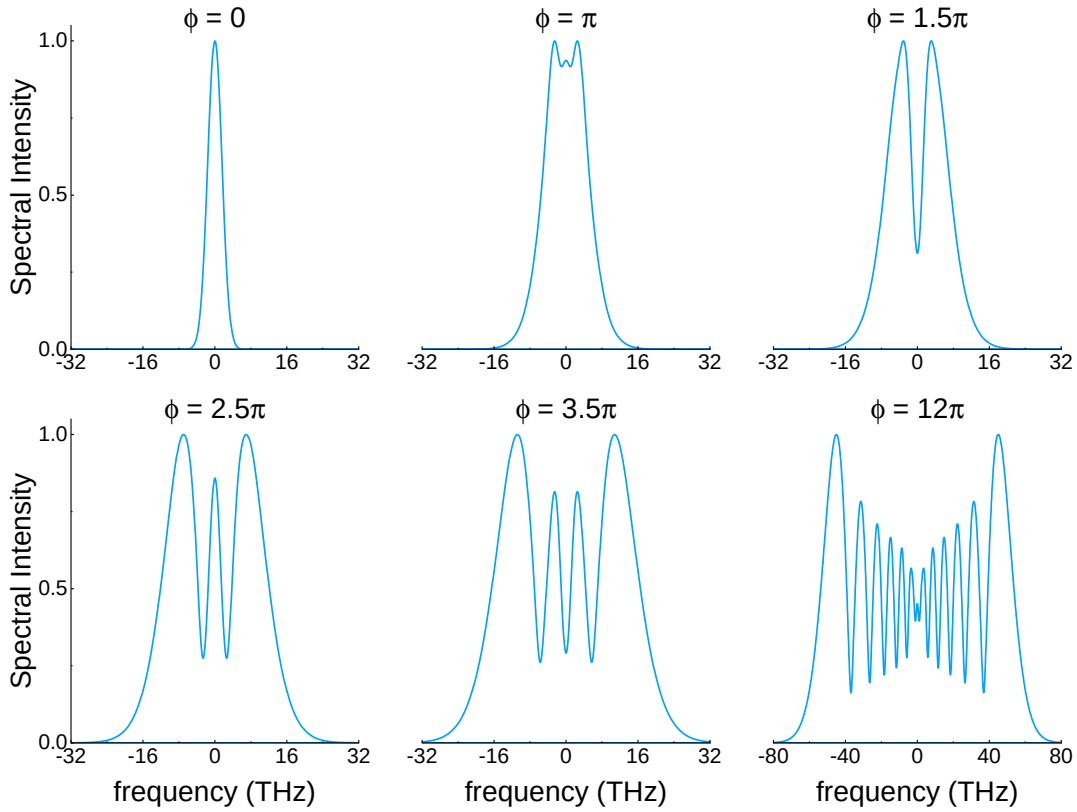

Fig. 3.4. Spectra modified via SPM A Gaussian pulse is propagated through different nonlinear phases, without considering dispersion effects. The spectrum broadens and develops an oscillatory structure, always keeping two prominent peaks at both sides of the spectrum. Note these spectra have been normalised to their maxima, but their maximum intensity decreases with spectral broadening as to conserve the area of the spectrum.

What we first notice is how the spectrum broadens and develops an oscillatory structure that covers the whole spectral range symmetrically from its center. In general, the spectrum consists of many peaks (the number of peaks increases linearly with the nonlinear phase), with the most prominent peaks at both edges of the spectrum.

This structure can be understood by considering the chirp introduced by SPM. The chirp is a nonlinear function of time and will in general have the same value at two different times t. This means there will be pairs of equal frequencies that can interfere constructively or destructively depending on their relative phase. In any case, it must be noted that the symmetry of the spectrum is not a general property, and can be broken by different pulse shapes or original chirp in the pulse.

When GVD and SPM contributions are of the same order, the pulse dynamics can change significantly. We simulate this situation making full use of the symmetrized SSFM, with a distance step chosen so that the distance sample spans 1500 points. In the normal-GVD region ($\beta_2 > 0$), the pulse stretching is enhanced by SPM, and the stretching factor increases with distance. This can be understood by thinking how the linear chirp introduced by GVD temporally distributes the frequencies in the pulse from trailing (blue) to leading edge (red), and the new frequencies generated by SPM are red- or blue-shifted accordingly, boosting the pulse stretching. The specific pulse shape and spectrum structure can vary significantly depending on the ratio between both contributions, but in general the minima of the peaks generated by SPM are not as deep when GVD plays a role.

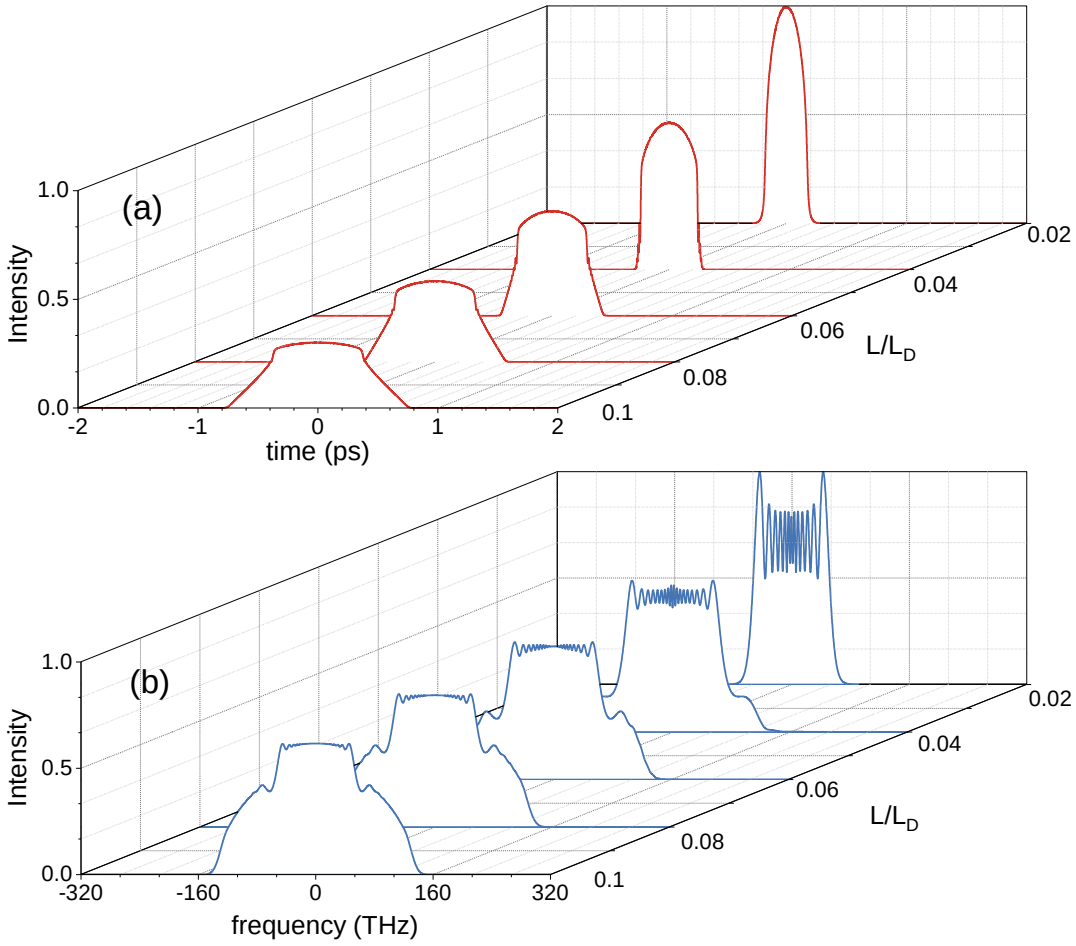

Fig. 3.5. (a) temporal and (b) spectral evolution of a pulse propagating under GVD and SPM simultaneous dynamics, simulated with with SSFM. The pulse is propagated with non-zero $\beta_2 > 0$ and γ coefficients, with $L_D/L_{\mathrm{NL}} = 2000$, for different distances L/L_D. The interplay of GVD and SPM lead to intricate forms of the pulse in both time and frequency domains, but in general the broadening rate will increase when $\beta_2 > 0$ and decrease when $\beta_2 < 0$.

3.3.3 Soliton dynamics

Very rich dynamics arise when propagating the pulse in the anomalous-GVD region, i.e. with $\beta_2 < 0$. The opposing contributions to the chirp from GVD and SPM give rise to the formation of a **soliton**, characterised by its soliton order $N^2 = L_D/L_{NL} = \gamma P_0 \tau^2/|\beta_2|$. If $N \approx 1$, the chirp from SPM and GVD tends to cancel out, and the *fundamental soliton* pulse shape will remain constant along its propagation through the fiber. As a matter of fact, it can be shown that fundamental solitons in an optical fiber must have a sech^2 shape[58], so that even with $N = 1$, if the original pulse has a different shape, it will asymptotically tend to reshape as a sech^2 pulse. This behaviour can be seen in Fig. 3.6, where an initially gaussian pulse is propagated with $N = 1$ and it evolves to become a sech^2 pulse, while its spectrum narrows due to the Fourier-limited broadening of the pulse. If $N > 1.5$, the pulse will find a different steady state which will consist on some sort of periodical behaviour of the pulse shape, were several peaks may appear in both time and spectral domains to be recombined again in a cyclic manner, as in Fig. 3.7.

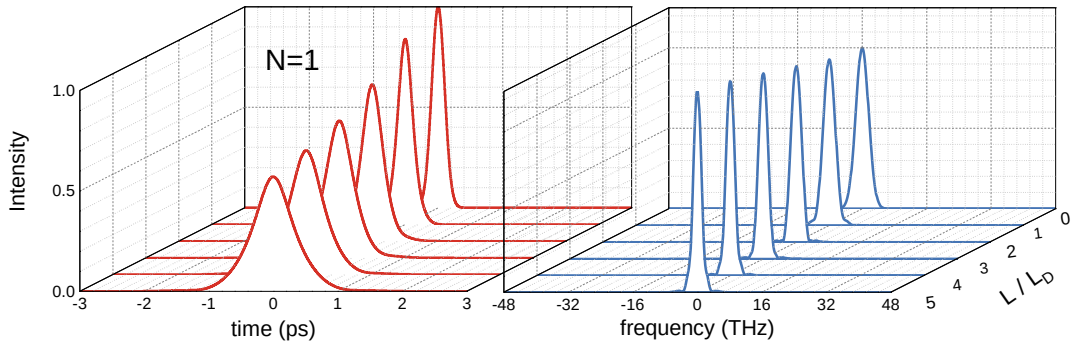

Fig. 3.6. Fundamental soliton. An initially Gaussian pulse is propagated under conditions such that $N = 1$, so that it reshapes to form a sech^2 fundamental soliton. In this process the pulse stretches in time domain and its spectrum narrows, keeping a chirp-free pulse.

A soliton of order N can be portrayed as a superposition of N fundamental solitons evolving collectively in a periodic fashion. This formation can only remain intact if all the individual solitons travel with the same group velocity, but any dispersive or nonlinear perturbation may break a high order soliton into its fundamental constituents, leading to the so-called **soliton fission**. Without this phenomenon, spectral broadening in the anomalous-GVD region would not occur, since a soliton would keep its spectrum intact or periodically varying in a steady state. Typical features of soliton fission are observed in Fig. 3.8, where a spectral peak appears by the high-frequency side of the spectrum and a pulse gradually separates from the main peak in time domain, when being perturbed by TOD. Any soliton, even when $N = 1$, will emit part of its energy when perturbed by TOD or higher order dispersion, in what is called non-solitonic radiation or a *dispersive wave* which, in the case of $\beta_3 > 0$, is emitted by the short-wavelength side of the spectrum, and consequently travels at a group velocity that is higher than that of the original pulse[6].

Different phenomena related to soliton fission contribute to exceptional spectral broadening and supercontinuum generation. The creation of dispersion waves from TOD generate spectral peaks in the blue or anti-Stokes side of the spectrum, and *intrapulse Raman scattering* may form Raman solitons on the red or Stokes side. These spectral

[6]Remember $\beta_2 < 0$ in the anomalous-GVD region and blue components travel at a faster group velocity than red ones.

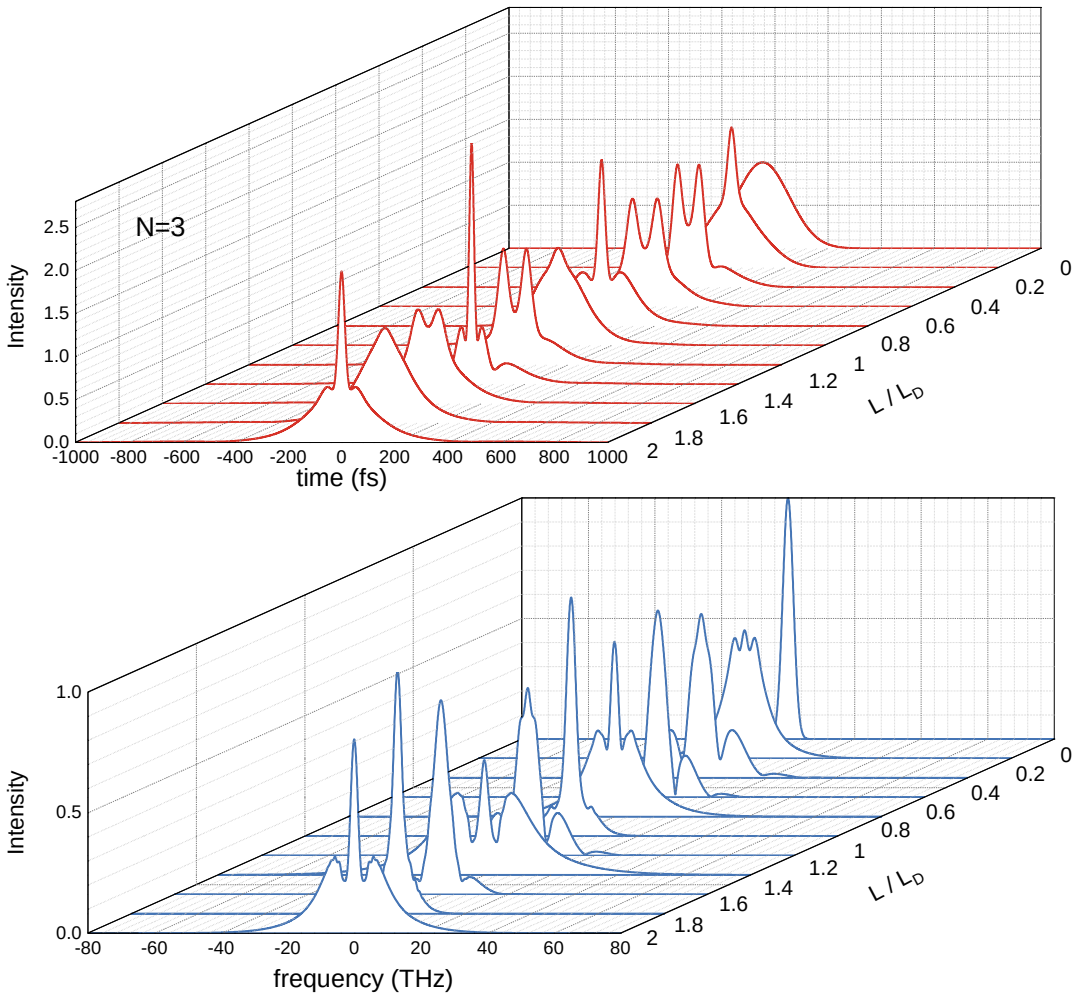

Fig. 3.7. Third order soliton A third order soliton (N=3) exhibits a cyclic behaviour in both time (**top**) and frequency (**bottom**) domains, such that the chirp induced by SPM and GVD compensates periodically, finding a steady state as long as the pulse is not perturbed by higher-order effects.

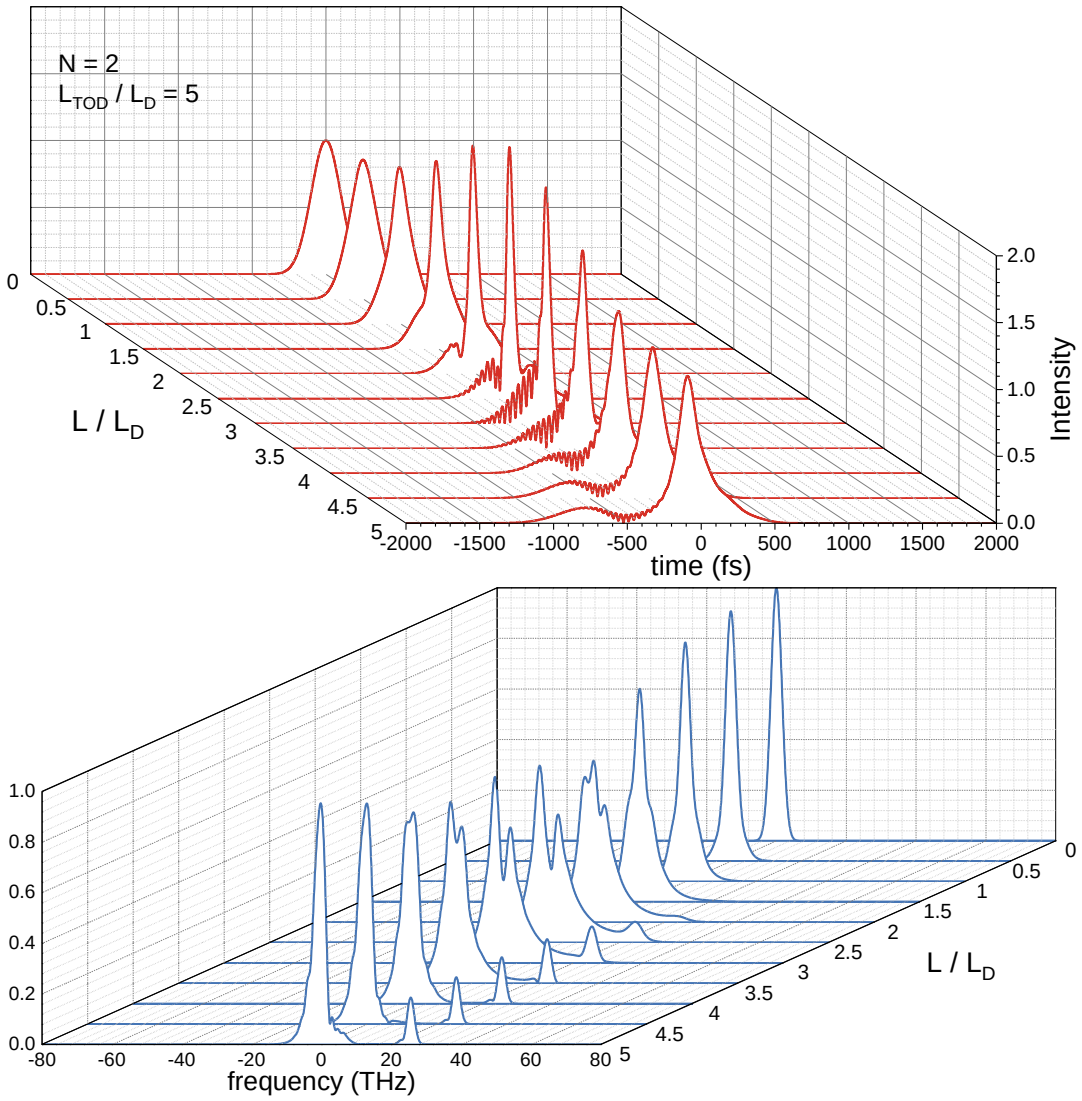

Fig. 3.8. Soliton fission A TOD perturbation is introduced to the second order soliton conditions, such that $N = 2$ and $L_{\mathrm{TOD}}/L_{\mathrm{D}} = 5$. A spectral peak appearing in the high-frequency (anti-Stokes) side of the spectrum (**bottom**) is a typical evidence for soliton fission. The original pulse separates into two pulses in time domain (**top**), a soliton and a dispersive wave, and fringes from their coherent interference appear in the overlapping region.

peaks at both sides of the original spectrum may overlap in time domain and generate new spectral components, under certain phase-matching conditions, through *cross-phase modulation* and *four-wave mixing*, making it possible for the original spectrum to span many octaves of frequencies and form a supercontinuum. Additionally, one must note the full spectrum may fall on both sides of the zero-dispersion wavelength, which means there will be a combination of the different dynamics from the normal- and anomalous-GVD regions discussed so far. Our current version of the code does not include Raman scattering, and thus leaves out some of the effects that lead to a realistic broadening of the spectrum, but we can still reproduce the conditions that we find in our experimental setup and study the expected broadening from SPM, GVD, TOD and higher order dispersion terms.

3.3.4 Simulation with experimental parameters

Up to here we have studied the effects of GVD, TOD and SPM in pulse propagation dynamics from a purely theoretical point of view, but we would be interested in simulating the pulse propagation under conditions similar to those we may find in the lab. Our main goal is finding the parameters that allow for broadening the spectrum up to an octave of frequencies, thus enabling f-$2f$ interferometry.

The parameters we need to consider are those describing the ultra-short pulses and the propagation medium. In the latter case, we will consider a highly nonlinear fiber that enhances SPM for spectral broadening, which is a photonic-crystal fiber (PCF) from NKT Photonics, namely the SC-3.7-975. The manufacturer offers a curve for a frequency dependent β_2 parameter, which means that for a correct description, higher order dispersion terms in frequency have to be considered. Performing numerical fittings of $\beta_2(\omega)$ around the central laser wavelength $\lambda_c = 1050$ nm for polynomials of different orders, led to an optimal fitting at third order in frequency, which means that terms up to fifth order in the Taylor expansion of $\beta(\omega)$ need to be considered[7]. Therefore, the linear operator $\hat{D}$ in Eq. 3.21 will have terms up to fifth order in frequency, i.e.

$$\hat{D}(\omega) = \frac{i}{2}\beta_2(\omega-\omega_c)^2 + \frac{i}{6}\beta_3(\omega-\omega_c)^3 + \frac{i}{24}\beta_4(\omega-\omega_c)^4 + \frac{i}{120}\beta_5(\omega-\omega_c)^5 \quad (3.34)$$

with $\omega_c = 2\pi/\lambda_c$. The β parameters extracted from the fitting of the manufacturer's data are

β_2	$-9.03 \pm 0.03 \cdot 10^{-27}$	s^2/m
β_3	$8.06 \pm 0.01 \cdot 10^{-41}$	s^3/m
β_4	$-5.25 \pm 0.04 \cdot 10^{-56}$	s^4/m
β_5	$2.1 \pm 0.1 \cdot 10^{-72}$	s^5/m .

The nonlinear coefficient is simply provided by the manufacturer for this fiber and is $\gamma = 18\ (W \cdot km)^{-1}$, and the mode field diameter is 3.3 μm. The index of refraction is 1.45 as it usually is in silica fibers.

[7] If β_2 was constant, we would "cut" the expansion of $\beta(\omega)$ at second order. A linear β_2 asks for a third order contribution ($\beta_3 \neq 0$)... and a cubic behaviour of β_2 means that at least $\beta_5 \neq 0$ needs to be considered.

With respect to the pulse characteristics, the pulses are again taken to be $\tau = 100$ fs Fourier-limited Gaussian pulses with a spectrum centered at $\lambda_c = 1050$ nm. The pulse peak amplitude $\mathcal{E}_0$ (and thus its shape) is reconstructed from Eq. 3.7, which can be integrated analytically for a Gaussian pulse, and therefore the peak amplitude can be expressed in terms of the average beam power $\bar{P} = 100$ mW, the repetition rate $f_r = 40$ MHz, and a spatial area of integration corresponding to a circle of radius $w_0 = 3.3$ μm equal to the fiber's mode field diameter, i.e.

$$\mathcal{E}_0 = \sqrt{2\bar{P}/(\pi w_0^2 \sqrt{\pi}\tau f_r \epsilon_0 c)}\,. \tag{3.35}$$

The intensity profile in both time and spectral domains is shown in Fig. 3.9, calculated at different distances inside the fiber from the SSFM simulation. One can clearly see the emission of dispersion waves typical of TOD, and an abrupt broadening of the spectrum at the very short distance of $\sim$ 3 cm, which then seems to cease and keep a practically constant bandwidth for longer distances. This spectrum is already spanning an octave of frequencies under the current conditions, and one must remember than intrapulse Raman scattering is expected to enhance the spectral broadening even more. This simulation shows in a coarse manner that the conditions for octave spanning can be achieved with a set of parameters similar to the ones considered here, that may be achieved in our current setup as it will be shown in the following chapters.

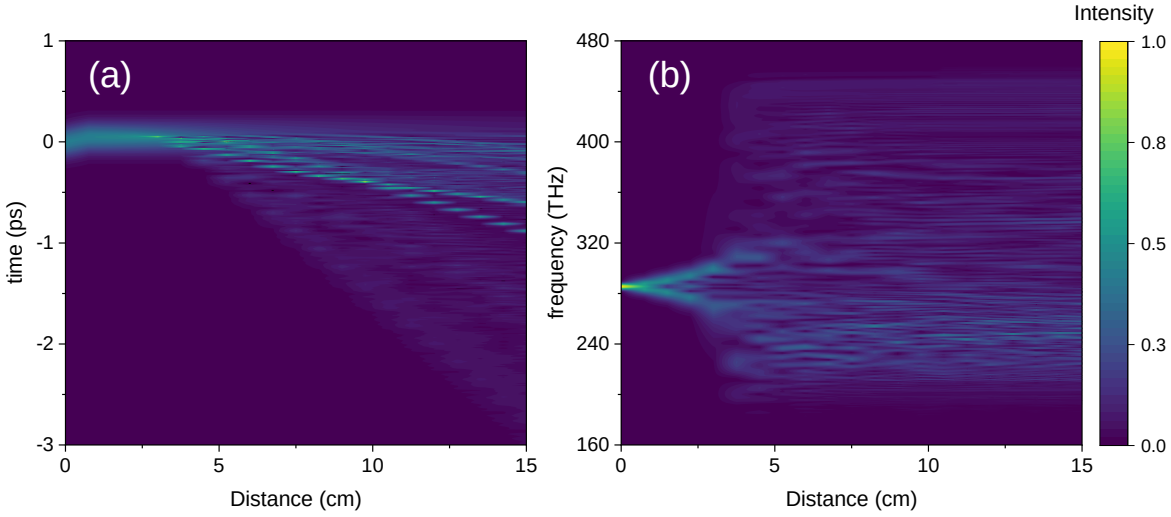

Fig. 3.9. Temporal (a) and spectral (b) evolution of a pulse under realistic conditions, accounting for up to fifth-order dispersion terms and SPM. An initially Gaussian pulse is propagated in a photonic-crystal fiber with dispersion and nonlinear parameters extracted from the manufacturer's specifications (see main text). The initial pulse is reconstructed from measured average power, pulse duration, repetition rate and mode-field diameter of the fiber. Clear signs of dispersive wave emission can be seen in (a), and (b) shows a spectrum that broadens significantly even lacking contribution from intrapulse Raman scattering.

Chapter 4

Yb fiber amplifier

One of the cornerstones of the f-2f interferometer is the broadening of the comb spectrum up to an octave of frequencies, mainly via self-phase modulation. Being a non-linear process, it is highly dependant on the peak intensity of the light pulses. The 60 mW direct output from the Yb:KYW oscillator proved to be insufficient for effective octave spanning, and for this reason it was necessary to design and build an optical amplifier for this work. This consists of an Yb-doped fiber amplifier and a pulse compressor, such that not only the average power of the laser beam is amplified, but also the peak power of the pulses.

This idea is inspired by the *chirped-pulse amplification* (CPA) protocol [59], which is used by most high-power lasers in the world, and which granted the Nobel prize to Gérard Mourou and Donna Strickland in 2018.

The motivation behind the CPA protocol is that direct amplification of ultra-short pulses is not straightforward, because due to their high peak intensities, unwanted distortions from non-linearities can be introduced or even the gain medium or other optical elements can be damaged. For this reason, if the pulses are stretched and chirped by a *pulse stretcher* before amplification, the peak intensity is significantly reduced while keeping the same average power and spectral properties intact. Then, they can safely be amplified in an optical amplifier that increases the pulse energy while possibly chirping and stretching the pulses even more. Finally, a *pulse compressor* is used for compressing the pulses again and concentrating the amplified average power in short pulses with high peak power.

In this work we implement a similar protocol, but dispensing with the pulse stretcher, because the initial power is not enough to damage the optical fibers used in the amplifier or to produce significant non-linear effects.

Throughout this chapter, we will deepen in the theoretical concepts that are needed for understanding how to design and construct a fiber amplifier and a pulse compressor, and we will present the actual setup that was built for amplifying the pulses up to a power that will allow us to span an octave of frequencies in the f-2f interferometer.

4.1 Theoretical background

4.1.1 Laser amplification

The process of coherent light amplification is the core principle of lasers[1]. As a matter of fact, a laser system is basically a laser amplifier in which the output is fed back to the input, hence the denomination of optical oscillator.

Light amplification is achieved from the interaction of light with a gain medium. At the microscopic level, this interaction is fundamentally governed by three mechanisms: absorption, spontaneous emission and stimulated emission. Absorption and stimulated emission are responsible for attenuation and amplification respectively, and spontaneous emission is the cause of noise generated in the amplifier.

By stimulated emission, a photon in a given mode can induce the emission of a photon into the same mode from a system that undergoes a transition from an excited state to a lower energy state, as long as the energy of the incoming photon is approximately the same as the energy difference between the two levels, i.e. $E_2 - E_1 = h\nu$. This energy matching condition restricts the interaction to a certain bandwidth of frequencies, which is given by the linewidth of the transition. More explicitly, the probability density rate for stimulated emission can be written as [60]

$$W = \phi\sigma(\nu) = \phi\frac{\lambda^2}{8\pi\tau_{sp}}g(\nu)\ , \tag{4.1}$$

where ϕ is the photon-flux density and $\sigma(\nu)$ is the transition cross section, which depends on the wavelength of the light in the medium λ, the effective spontaneous lifetime τ_{sp} and the normalized lineshape function $g(\nu)$. Interestingly, the probability density for absorption is exactly the same as that for stimulated emission.

Now, let us picture the gain medium as an ensemble of two-level atoms with N_1 atoms in the lower state and N_2 atoms in the upper state. The density number of absorbed photons must be N_1W and the density number of photons emitted by spontaneous emission N_2W. Consequently, the net gain in the number of photons per unit of time and volume is $(N_2 - N_1)W \equiv NW$. From this, it is obvious that, in order to have a positive net gain in the process, the effect of stimulated emission must be predominant over absorption, which necessarily means having more atoms in the excited state than in the lower state., i.e. $N > 0$. This situation is referred to as *population inversion*, because this is generally not the case for an ensemble of atoms in thermal equilibrium. Therefore, one needs an excitation mechanism to drive the system out of equilibrium, that comes in the form of a pump that continuously populates the upper level.

The gain

To characterize the net gain in an amplifier, we can first describe the differential increment in the photon-flux density $\mathrm{d}\phi$, in a differential slide of the medium $\mathrm{d}z$

$$\frac{\mathrm{d}\phi}{\mathrm{d}z} = NW = \phi N\sigma(\nu) \equiv \phi\gamma(\nu)\ , \tag{4.2}$$

[1] Remember that LASER stands for Light Amplification by Stimulated Emission of Radiation.

where we have used Eq. 4.1 for W, and then defined the *gain coefficient* as

$$\gamma(\nu) = N\sigma(\nu) = N\frac{\lambda^2}{8\pi\tau_{sp}}g(\nu)\ . \tag{4.3}$$

Solving Eq. 4.2 tells us that the photon-flux increments exponentially with the distance, and consequently, so do the optical intensity $I = h\nu\phi$ and the optical power.

$$\phi(z) = \phi(0)e^{\gamma(\nu)z}\ , \tag{4.4}$$
$$I(z) = I(0)e^{\gamma(\nu)z}\ , \tag{4.5}$$
$$P(z) = P(0)e^{\gamma(\nu)z}\ . \tag{4.6}$$

Finally, we can measure the net gain of the amplifier by comparing the input and output optical powers, after a total interaction length L, corresponding to

$$G(\nu) = \frac{P(L)}{P(0)} = e^{\gamma(\nu)L}\ . \tag{4.7}$$

It should be noted that we have established the following relations: the gain coefficient $\gamma(\nu)$ depends on the population inversion N (Eq. 4.3), N is governed by the pumping rate and the transition rate W, and W depends on the photon-flux ϕ (Eq. 4.1). This means that the gain coefficient depends on the photon-flux to be amplified, which is the origin of amplifier non-linearity and gain saturation. Gain saturation stems from the fact that a high power signal[2] can compete with the pump, in the sense that when stimulation emission is too high, population inversion is destroyed and $N \approx 0$. At this point the amplifier is saturated and does not amplify anymore. In general we can write a *saturated gain coefficient*

$$\gamma(\nu) = \frac{\gamma_0(\nu)}{1 + \phi/\phi_s(\nu)}\ , \tag{4.8}$$

where N_0 and $\gamma_0(\nu)$ are the "small signal" population inversion and gain coefficient respectively, and $\phi_s(\nu)$ is the saturation photon-flux density. Eq. 4.8 makes it clear that the gain coefficient decreases as the photon flux ϕ increases, and tends to zero for high values of the signal photon flux.

Pumping schemes

As we have pointed out previously, as long as the gain coefficient is positive, i.e. there is population inversion, there will be amplification in the system. There are different pumping schemes to transfer population from the lower to the upper laser level, but they all involve the use of auxiliary energy levels. This is due to the fact that in a continuously driven two-level system, since the absorption and stimulated emission probabilities are equal, the best one can obtain is continuous oscillations of the population between the two levels, known as Rabi oscillations. Therefore, it is mandatory to use three or four atomic levels, or even bands of level manifolds to

[2]By signal we refer to the laser light that is being amplified. We may sometimes refer to the input signal as the *seed*, before amplification.

achieve population inversion. In the next section, we will study the specific pumping scheme, as well as the absorption and emission bandwidths and any other relevant characteristics of the amplifier that was build for this work, an ytterbium-doped fiber amplifier.

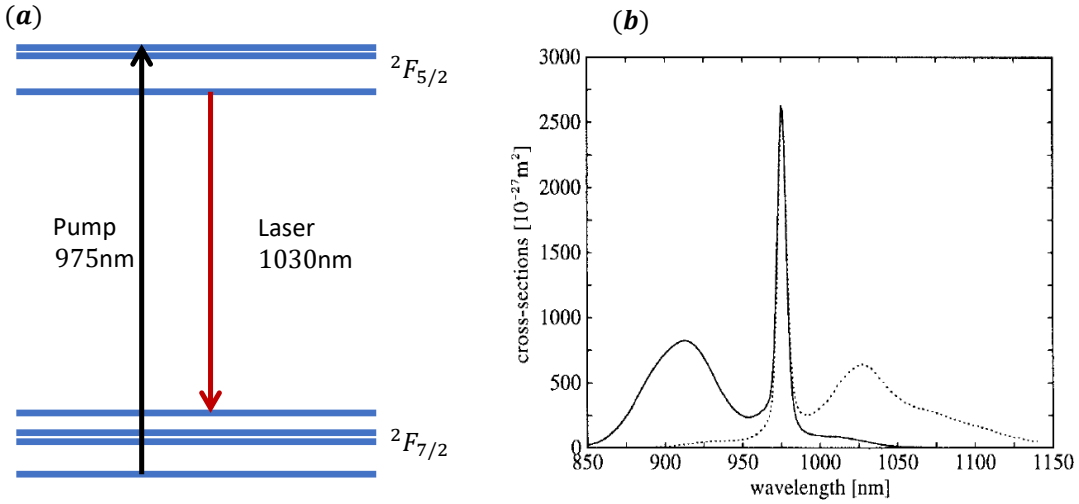

Fig. 4.1. Spectroscopic characteristics of Yb^{3+}. (a) Energy level scheme (not to scale), showing the $^2F_{7/2}$ and $^2F_{5/2}$ manifolds participating in the laser transition and pumping scheme of the Yb-doped fiber amplifier. **(b)** From R. Paschotta et al. [61]. Absorption (solid) and emission (dotted) cross sections of Yb-doped germanosilicate glass. The absorption peak at 975nm is pumped for amplification of radiation near the 1030nm emission peak.

4.1.2 Yb fiber amplifier

Ytterbium-doped fibers are commonly silica glass optical fibers, with a core doped with Yb^{3+} ions. Using an optical fiber as a gain medium allows for long amplification regions, of several meters easily. So even though the gain coefficient may be small compared to other systems, the net gain may be of tens of decibels with moderate pump power, which may generate an output of hundreds of watts or even kW. In single-mode fiber amplifiers the signal and the pump propagate together in the core, but to achieve very high powers double-clad fibers are used. In these fibers the laser light propagates in the single-mode core, and the pump travels through an inner cladding, that allows for multi-mode propagation[3] at higher power. This reduces the risk of destroying the fiber and avoiding distortion of the gain shape caused by saturation from a standing-wave like pump spatial mode (spatial hole burning). Every time the pump passes through, or partially propagates in the core, amplification of the laser light occurs.

The spectroscopic scheme of Yb^{3+} shows two relevant energy level manifolds for the laser transition: the $^2F_{7/2}$ manifold acting as the lower level, and the $^2F_{5/2}$ manifold serving as the upper one. Note that these manifolds consist of 4 and 3 sublevels respectively, as depicted in Fig. 4.1 (a). The specific absorption and emission spectra

[3] Multi-mode propagation can be visualized as geometrical reflections inside the cladding.

have some dependency on the host medium, and these are shown for Yb in germanosilicate glass, which is the most common material for optical fiber cores (Fig. 4.1 (b)).

From the absorption and emission spectra one can see how there are different pumping-lasing schemes, always considering that the pump must have shorter wavelength than the signal. One can for instance pump the peak at 910 nm and amplify at 975 nm, or as it is the case in our experiment, pump at 975 nm and amplify near the wide 1030 nm peak. For the latter configuration, since the absorption peak is narrow, the pump linewidth must be rather small, and a maximum of 50% excited population can be achieved because of the absorption and stimulated emission cross sections being equal at 975 nm, which sets a limit to the gain of the amplifier.

4.1.3 Pulse compression with gratings

The dispersion introduced by the typically long fibers in fiber amplifiers can be compensated by a pair of parallel gratings. These act as a *pulse compressor*.

In fact, any optical element that introduces chromatic angular dispersion, introduces GDD. This can be intuitively understood by acknowledging that after the dispersive element, different frequency components follow different optical paths, which introduces a frequency dependent phase delay in the pulse. This causes spectral dispersion in time domain (chirp), while leaving the spectrum unchanged, and inevitably stretching or compressing the pulse, depending on its original chirp. By using a second dispersive element after the first one, one can compensate for the angular dispersion and make all the spectral components parallel again, keeping a collimated but compressed (or stretched) pulsed beam.

To characterize the GDD introduced by a pair of parallel gratings, we first need to obtain the phase delay $\psi(\omega)$ for different spectral components. For this, we can take a central frequency ω_0 and a neighbouring frequency $\omega = \omega_0 + \mathrm{d}\omega$, such that if ω_0 is diffracted by an angle β' on a first grating, the ω component is diffracted by $\beta' + \mathrm{d}\beta'$.

Let us look at the frequency dependent optical path $\overline{ABC}$ shown in Fig. 4.2. The ω component follows a path $\overline{AB} = \frac{b}{\cos\beta'}$ and $\overline{BC} = \overline{AB}\sin\left(90^\circ - (\beta + \beta')\right) = \frac{b}{\cos\beta'}\cos(\beta + \beta')$, such that

$$\overline{ABC} = \frac{b}{\cos\beta'}\left(1 + \cos\left(\beta + \beta'\right)\right) , \tag{4.9}$$

where β is the angle of incidence, β' the diffraction angle[4], and b is the normal distance between the gratings. The incidence and diffraction angle are related through ω by the grating equation. For the first order of diffraction $m = 1$:

$$\sin\beta' - \sin\beta = \frac{2\pi c}{\omega d} , \tag{4.10}$$

where d is the distance between the grating grooves. Usually, we would say that the phase delay is related to the optical path length through $\psi(\omega) = L_{\text{opt.}}(\omega)\omega/c$, but gratings have a special feature that adds an extra correction to that. In a grating,

[4]Note that $\beta' + \mathrm{d}\beta' \approx \beta'$

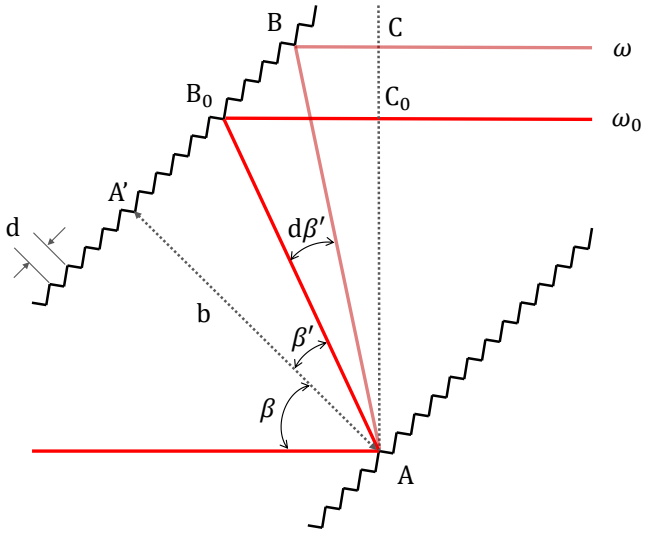

Fig. 4.2. Two parallel gratings set up for pulse compression. Higher frequencies are diffracted by a larger angle β' and travel a shorter path length, which causes a negative GDD on light pulses. Note that $d\beta'$ is a differential quantity and its size has been exaggerated. The choice of a reference wavefront $\overline{CC_0}$ is arbitrary, and it has been chosen so that its extension falls on A for convenience.

there is a $2\pi m$ phase-shift from one groove to the next one, such that we should account for a phase difference of 2π times the number of grooves between B and B_0 [62]. This can also be done consistently by just subtracting a phase to $\overline{ABC}\omega/c$, corresponding to the number of grooves from A' to B. This gives a frequency dependent phase delay of [57]

$$\psi(\omega) = \frac{\omega}{c}\overline{ABC} - 2\pi\frac{b}{d}\tan\beta' \,. \tag{4.11}$$

The GDD is obtained as the second-order derivative of Eq. 4.11, making use of Eqs. 4.9 and 4.10:

$$\mathrm{GDD} = \frac{\mathrm{d}^2\psi}{\mathrm{d}\omega^2} = -\frac{4\pi^2 bc}{\omega^3 d^2\cos^3\beta'} \,. \tag{4.12}$$

Rewriting this expression for wavelengths, at the central wavelength λ_0 , one gets

$$GDD\Big|_{\lambda_0} = \frac{\mathrm{d}^2\psi}{\mathrm{d}\omega^2}\Big|_{\lambda_0} = -\frac{\lambda_0}{2\pi c^2}\left(\frac{\lambda_0}{d}\right)^2\frac{b}{\cos^3\beta'} \,. \tag{4.13}$$

This equation shows how the dispersion introduced by a pair of gratings is always negative. This can be intuitively understood looking again at Fig. 4.2, and noticing that the higher frequencies travel a shorter optical path, making the blue components come out before the red ones in the pulse (negative chirp). Even though we are calling this device a pulse compressor, it should be clear that a pulse with no initial chirp can only be stretched by introducing GDD of any sign. But it is precisely because the pulses coming out of the long fiber amplifier are positively chirped and

stretched (positive GDD is introduced in the normal-GVD region), that the pulse compressor can be tuned to compensate for the amplifier's GDD with opposite sign, and restore the pulses to their original width. This tuning is usually made by adjusting the distance b between the pair of gratings with a specific grating parameter d^{-1}. The transverse displacement of the different spectral components can be compensated by using two consecutive pairs of gratings or by sending the beam twice through the same grating pair, keeping in mind that in that case we are introducing twice the dispersion of Eq. 4.13.

4.2 Experimental setup

4.2.1 Yb-doped fiber amplifier

For the amplification of the 60 mW output from the Yb:KYW oscillator, in this work, a fiber amplifier based on an Yb-doped double clad fiber (Yb-DCF), was built. The gain medium fiber is the YB1200-10/125DC from Thorlabs, an ytterbium-doped single mode double-clad fiber with a 7 ± 0.5 μm mode-field diameter [5] and a 125 ± 2 μm inner cladding diameter. The core numerical aperture (NA), defined as the value of the sine of the largest incidence angle a ray can have for total internal reflection, is NA $= 0.12$, which is a typical value in SM fibers. The amplifier is fully fiber based, which makes it compact and robust. The different fibers and optical elements used in the amplifier will be explained throughout this section. A photo of the Yb-DCF can be seen in Fig. 4.3.

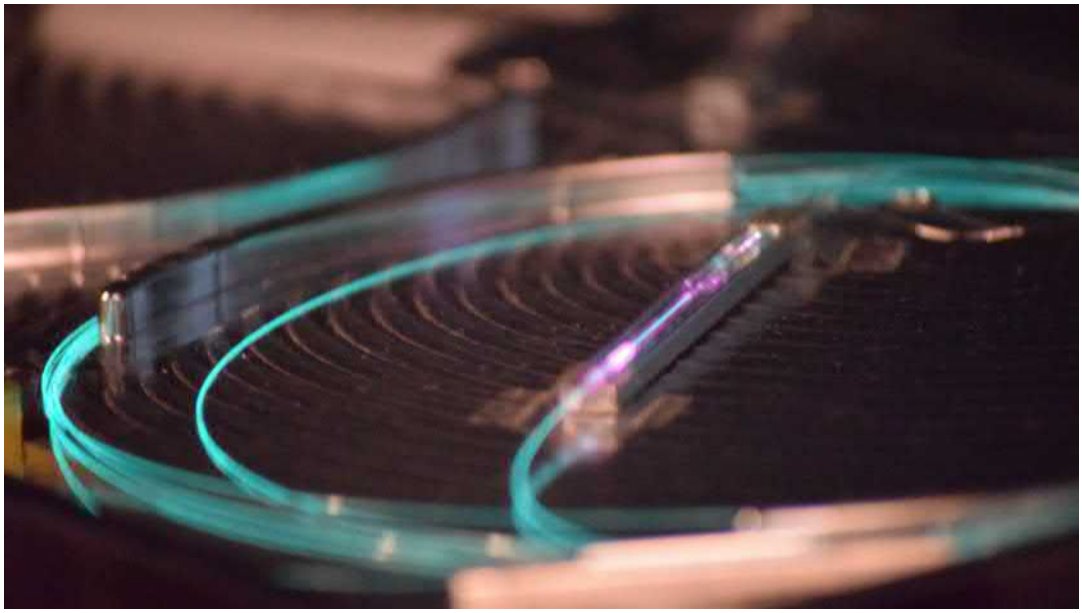

Fig. 4.3. Ytterbium-doped double-clad fiber. The Yb-DCF has a core doped with Yb^{3+} ions that acts as a gain medium. The 1050 nm signal propagates through the core, and the 975 nm pump propagates through the inner cladding. The appreciable green glow is a typical fluorescence emission in Yb. A metallic case for protecting a spliced region can also be seen.

[5] This is similar, but not equal to the core diameter.

Coupling light to the amplifier

To optimize the free-space-to-fiber coupling at the input of the amplifier, a GRIN lens is used. These are solid cylinders engineered to have an index of refraction $n(r)$ that varies radially and continuously from a maximum value at its symmetry axis to a minimum at its outer surface[6]. It can be shown that when this variation is parabolic, an initially collimated beam can be focused to a certain focal point. The GRIN lens used is a commercial device that is glued to a SM fiber and is designed in such away that accounting for the lens width and length, a beam of light incident on the GRIN lens is focused and coupled to the core of the fiber. This simplifies the task of coupling light into the fiber, since one does not need to be concerned with finding the right focusing lens configuration. Still, the laser beam needs to be resized to a 1.8 mm waist, which is smaller than the starting Yb:KYW output. To resize a collimated beam, two regular lenses can be used in a telescope configuration. In this case, two lenses of focal lengths $f = 500$ mm and $f = 150$ mm are used such that the beam size is reduced to a ~ 1.8 mm waist and still collimated. Measuring the power right at the output of the SM fiber attached to the GRIN lens permits aligning and optimizing the coupled power to nearly 80%.

Now that we have a way to couple the light into a SM fiber, we need to splice this to the Yb-DCF. A splice of two fibers with different core sizes and cladding configurations is delicate, but it can be done with a fusion splicer. The FSM-30S Arc Fusion Splicer model from Fujikura can automatically align the cores of two fibers and splice both fiber ends together by quickly heating them up to their fusion temperature, without significant power loss at the joint. An imaging system and digital display allow for checking the quality of the prior alignment and subsequent splicing. The success of this process is highly dependent on how well the fiber ends are cleaved. One must make sure that both end surfaces are cleaved clean and straight, i.e. with a sharp cut and no angle with respect to the fiber propagation axis. This is achieved with a cleaver from Fujikura. The same procedure (with appropriate parameter selection of the fusion cleaver) will be used for splicing all the other fiber segments used in this setup.

The pump

As explained in section 4.1.2, the pumping scheme of choice consists on pumping at 975 nm, such that we can amplify around 1030 nm or 1050 nm. This task is performed by a laser diode, the LU0975T090 from Lumics. According to the manufacturer, this diode operates at a maximum CW output power of 9 W for a 11.5 A current, even though it will be operated at much lower power for the range of amplification needed (< 3 A). The laser light goes straight into a multi-mode fiber with a 105 μm core and a 125 μm cladding diameter. It has a peak wavelength of 975 nm with a very narrow spectral width of 5 nm, even though it shifts with temperature by 0.3 nm/K, and 0.6 nm/W with changes in power. For this reason, and to avoid overheating of the diode, it needs to be temperature controlled.

To measure the diode temperature, an Analog Devices AD590 temperature sensor is attached to its surface with a thermally conducting glue. This sensor is an integrated circuit temperature transducer that produces an output current proportional to the absolute temperature. A Peltier element is used as a temperature controller. A Peltier device uses the thermoelectric effect to transfer heat from one side of the

[6]Other geometries are possible, but this is the one used in this work.

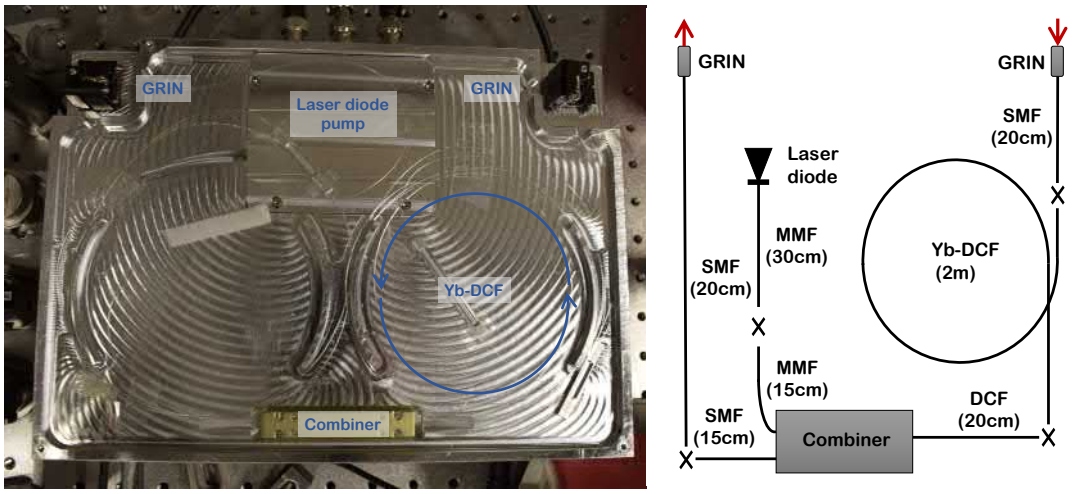

Fig. 4.4. Yb-doped fiber amplifier. The schematic figure on the **right** depicts the main components of the fiber amplifier. The signal laser is coupled into the fiber system through the right GRIN lens and a single-mode fiber (SMF), which is spliced to the Yb-doped double-clad fiber (Yb-DCF). This one is joint to a combiner via another double-clad fiber (DCF). The combiner receives the pump from a laser diode through multi-mode fibers (MMF) and sends it to the inner clad of the Yb-DCF. After amplification, the signal comes through the combiner's SMF and comes out the left GRIN lens. The *X* symbols mark fiber splicings. Note that the temperature stabilization system for the laser diode is not shown here (see text). On the **left**, a picture of the actual setup, with some labels for orientation. The compartment for the laser diode, Peltier element and temperature sensor is marked on the picture.

device to the other when an electric current is applied. The heat flux is proportional to the DC electric current, and is bidirectional, meaning it can heat up or cool down one surface or the other depending on the sign of the current. The diode is then attached to one surface of the Peltier element with thermally conducting double-sided tape, and by continuously reading the temperature one can stabilize and control it by sending a feedback signal to the Peltier device, compensating for temperature drifts and setting a chosen temperature. This is performed by a PID loop filter that compares the output current from the temperature sensor with a set-point, and sends a current to the Peltier element to keep the temperature at a constant value [7].

Now, we need to couple the pump laser to the Yb-doped fiber for enabling amplification. This is performed with the aid of a fiber-optic combiner. This device has two multi-mode fibers for pump inputs (one is idle in this case), one double-clad fiber for signal input / pump output and one single-mode fiber for signal output. The pump and signal fibers are tapered and fused together so that their cores are in close contact over a few centimeters. This way, the evanescent wave from one fiber can be coupled into the other fiber and both signal and pump are effectively combined. The signal DCF and the pump MMFs have 10/125 and 105/125 μm core and cladding diameters respectively. The MMF from the laser diode is then spliced to the combiner's MMF pump input, and similarly, the DCF from the combiner and the Yb-doped DCF are spliced together, coupling the 975 nm pump light into the amplifying fiber. Splicing the DCFs may be tricky since they have different core sizes (mode field diameters are 10 μm and 7 μm), but it can be achieved without great

[7] We will discuss PID controllers and feedback loops in Chapter 6

losses after, perhaps, a few attempts. A schematic view of the different fibers used and their splicing points is shown in Fig. 4.4.

Assembling and boxing

All the components are placed in a specifically designed metallic box, as can be seen in Fig. 4.4. This way the fiber is more tightly fixed and small motion, which would introduce polarization rotation, is minimized. The output SM fiber from the combiner, which propagates the amplified signal, is spliced to a SM fiber attached to a GRIN lens identical to that of the input coupler. In this manner, the output is a collimated beam of known size. The laser diode, temperature sensor and Peltier element that form the stabilized pump system are placed inside the compartment marked in the left picture on Fig. 4.4. Three BNC connectors, which pins were wired and soldered to those of the three constituent elements, allow cabling with a power supply for the laser diode (LD), and the PID controller, which receives the sensor's signal and supplies the Peltier element. The input and output GRIN-lens couplers were mounted in 1/2" mirror mounts for ease of alignment. The joints between spliced fibers are mechanically fragile, because the coating must be removed for splicing, thus they are sheltered by small metallic cases that accommodate the fiber in a central channel and make a frame that prevents contact with the un-coated segment, which is critical in DCF where the pump propagates through the cladding, (one can be seen in Fig. 4.3), while some others were just made a white-tape coat for less sensitive fibers such as SMF.

4.2.2 Pulse compressor

The fiber amplifier has a total length of approximately 3 m in optical fibers. This introduces significant dispersion in the light pulses, and thus broadening. As has been noted before, self-phase modulation (which will grant spectral broadening in the f-$2f$ interferometer) and non-linear effects in general, depend not on the average power, but on the peak power. For this reason, we would like to compress the pulses to at least compensate for the amplifier's dispersion, and reach the Fourier limited width if possible, therefore optimizing the pulses' peak power. For this purpose, a pulse compressor had to be designed and built for this work, based on the ideas of pulse compression by a pair of gratings explained in Section 4.1.3. We will first discuss some design concerns, and then explain the setup dividing it in two arms: the input and the compression arms.

Preliminary considerations

To design the compressor, we must first do an estimation of the GDD introduced by the amplifier. Ultimately, the parameter that we want to obtain is the distance needed between the gratings; b in Eq. 4.13. The different fibers produce slightly different GVDs, depending on their characteristics, but to do an estimation we will assume homogeneous dispersion along the amplifier.

We can quickly do some numbers by looking at the specifications of one of the fibers, that we can take as a model. For instance, the combiner's SM output fiber, a HI 1060 Specialty Fiber by Corning, has a dispersion of $D_\lambda = -38$ ps/nm/km at 1060 nm according to the manufacturer. Expressed as GVD, this is a (positive) group velocity dispersion of GVD $= 22.7$ fs^2/mm, which after 3 m produces a group delay dispersion of GDD $= 68 \cdot 10^3$ fs^2, corresponding to a final pulse width of 2 ps from the

initial 100 fs, which is a factor 20 larger. This highlights the importance of compressing the pulses after the amplifier.

Knowing the GDD, we can calculate the distance b between the gratings, but for that we need to know the specific parameters of the gratings to be used. These will be two T-1600-1030s lithographically patterned transmission gratings from II-VI. They have a line density of 1600 lines/mm, or equivalently, a line periodicity of $d = 0.625$ μm, and an optimal incident angle of 55.5° at 1030 nm. The incidence angle is, by design, that angle that maximizes the power transmitted in a certain diffraction order ($m = 1$ in this case). This is achieved by tilting the grooves in a certain angle, so that they have a sawtooth shape that form little prisms. In *blazed transmission gratings*, the transmitted intensity is maximized at an order m when the refraction of the incident light in a prism occurs in the same direction as the one given by the diffraction equation for that order, which is called the blaze angle[8]. It is common to choose the blaze angle such that the incident and diffracted angles are the same for a certain wavelength, in what is called the Littrow configuration. For our spectrum centered at 1050nm, the Littrow angle is $\sim 57°$.

With all this, we are in position to calculate the optimum distance b for the grating pair from Eq. 4.13. For the values of the GDD discussed, we obtain a distance of $b \sim 1$ mm, accounting for a two-step compression. Eventually, we will optimize the gratings' separation by mounting one of the gratings in a linear translation stage and finding the distance that minimizes the pulse width or autocorrelation function, that we will measure with a FROG system[9].

Setup: Input arm

The input arm, previous to the compression arm, consists of an optical isolator, to prevent any unwanted light from going back into the fiber amplifier, and a set of waveplates to prepare the right polarization states (see Fig. 4.5).

The optical isolator transmits light only in one direction, blocking the light going in the opposite direction. The most common way to achieve this is by means of the Faraday effect, by which the polarization of light propagating in certain materials can be rotated proportionally to an applied magnetic field. A Faraday isolator includes such a material with a permanent magnetic field (Faraday rotator), enclosed by two linear polarizers with a relative angle of 45° between their polarization axes. When light linearly polarized at the right direction comes into the isolator, it passes through the first polarizer without losses. The Faraday rotator is set to rotate the polarization axis by 45° and make it coincide with that of the second polarizer, such that the light comes out the isolator minimizing losses. If any light would come in from the output port, it would be polarized and rotated by yet another 45° such that it would be orthogonally polarized to the input polarizer, therefore being blocked by it.

Consequently, we need the ability to have linearly polarized light at an axis of choice at the input, and this can be achieved by a $\lambda/2$ waveplate (HWP1) and a $\lambda/4$ waveplate (QWP). Elliptical polarization coming from the fiber amplifier can be converted to linear polarization at an arbitrary direction by the QWP, and then set to a specific

[8] In reflection blazed grating this condition is satisfied when the reflection and the diffraction directions are matched.

[9] This will be discussed in Section 4.3.2

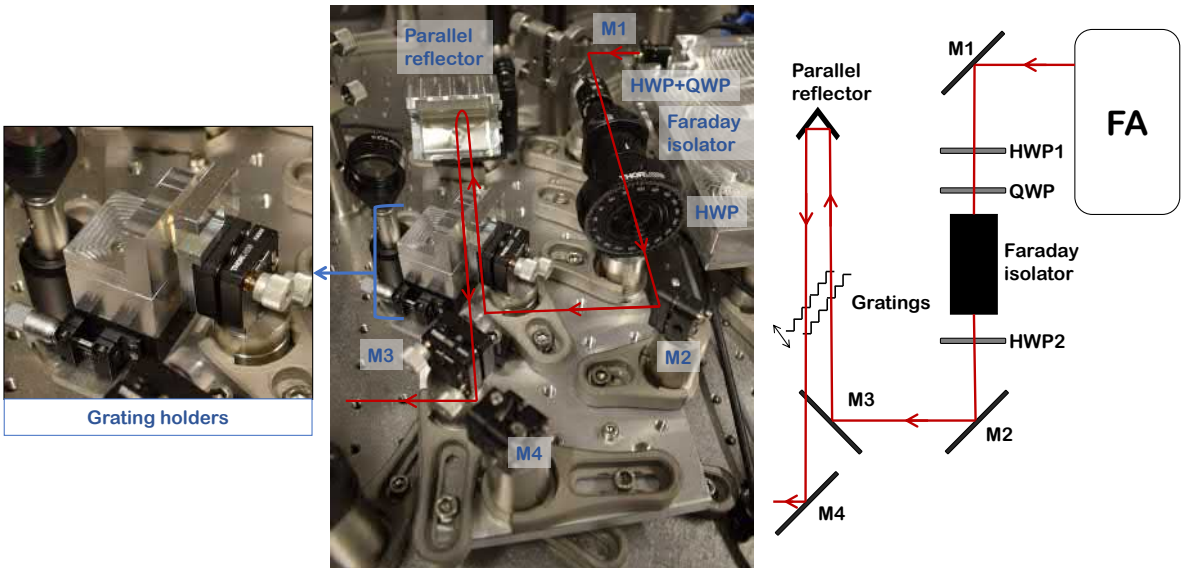

Fig. 4.5. Pulse compressor. The **rightmost** figure is a schematic of all the components forming the compressor module and their alignment. The laser beam coming out of the fiber amplifier (FA) is reflected by a first mirror (M1) through a half-wave plate (HWP) and a quarter-wave plate (QWP) and sent into the Faraday isolator. A second HWP and two mirrors (M2 and M3) send the beam through the gratings in S-polarization. The parallel reflector sends the beam back, but vertically displaced such that it goes again through the gratings but over M3. Finally the M4 mirror sends the beam out of the compressor module. The **central** picture is a photograph of the actual setup with labeled components and the laser beam path in red. On the **left**, a close-up on the custom grating holders.

polarization axis by the HWP1. This can be optimized with respect to the isolator by rotating both waveplates to maximize the transmitted output.

Yet another $\lambda/2$ waveplate (HWP2) is placed after the isolator because the gratings are designed to work at S-polarization, meaning the light should be polarized parallel to the grating lines for optimal performance. Again, we can rotate the HWP to maximize the intensity transmitted by the grating pair.

Setup: Compression arm

Alignment of the grating pair, as well as the mirror that allows for back reflecting the beam such that it passes twice through the gratings, is critical for the success of the compressor. These three elements compose the core of the compressor. The main idea is, as mentioned before, to fix one grating, and mount the other one on a translation stage with sub-millimeter precision, so that we can manually and precisely regulate the distance between them. Once the beam has passed once through the gratings, it will be reflected back by what we will call a parallel reflector, an arrangement of two mirrors forming 45° in a V-shape, such that the reflected beam is parallel to the incident beam, but displaced by a small distance in the vertical direction. This way, the reflection travels along the same path but in opposite direction and vertically displaced. The vertical shift is determined by the relative height of the incident beam with respect to the vertex where the two mirrors are joined, i.e. the incident and reflected beams are symmetrically shifted from the vertex. This has to be taken into account, since the gratings have a vertical length of 12.3 mm, and therefore the

separation of the beams cannot be larger than that[10]. The strict constraints on the relative height, angles, and parallelism of the gratings, made it necessary to design and manufacture special holders for the gratings, that are shown in Fig. 4.5.

Since the alignment of these elements can be pretty challenging, we will now describe it step by step.

First, we align the beam, parallel to the table, to a horizontal virtual axis that we will take as a reference for aligning the rest of the elements. Then, we must align one of the gratings (the one on the linear stage) with the beam, so that the incident angle is close to 55° - 57°. This can be done by finding the angular position that maximizes the intensity of the light at the first diffraction order. Once that position is found, we have to align the second grating to be parallel to the first one and approximately at the right distance $b \sim 1$ mm. The best way to do this is to move the stage to the most forward position, and then place the second grating as close to the first one as we can, avoiding direct contact. For finding the parallel position, the second grating with its holder were glued to a 1/2" mirror mount, such that the alignment could be fine tuned. Then, by observing the back-reflected beam at a distant screen, one can find the alignment that makes the beam more circular, i.e. that compensates the lateral spectral dispersion. As it was noted, the relative height of the incident beam with the gratings and parallel reflector is critical, because the reflected beam must fit within the gratings' window size, but also go over the $M3$ mirror without clipping, and hit the $M4$ mirror to be extracted out of the compressor. This was achieved by hitting the parallel reflector ~ 2 mm below the joint of its two mirrors, so that the two beams are separated by ~ 4 mm, which is enough for successful extraction of the compressed beam.

4.3 Results

4.3.1 Characterization of the amplified power

A first test to make is checking the performance of the laser diode (LD), in order to have an idea of the range of pumping optical powers that we can access, for reasonable values of the electric current. The average power of a laser beam with a relatively narrow spectrum can be measured with a photodiode powermeter.

Fig. 4.6 shows the LD ouput power measured right after its MMF, before splicing with the combiner. A typical diode behaviour is observed, with no significant emitted power before the threshold at 0.7 A, and a linear increase in power with increasing current from the threshold. The range of available powers is quite significant, rising up to 2 W for a current lower than 3 A. This proved to be very adequate for our application.

With the fully operative fiber amplifier, we would like to check the available output powers as a function of the pump electrical current. This is presented in Fig. 4.7. The power right after the fiber amplifier is compared to the output from the pulse compressor, to account for the losses introduced by the latter and characterize the average optical power that will be sent to the f-$2f$ interferometer. For a 3 A pump current we obtain a net gain factor of roughly 8, corresponding to an optical power of almost 500 mW, compared to the initial 60 mW. We also confirm the linear behaviour

[10] Actually, the limitation is more strict, because the alignment was such that the incident beam passes through the gratings at approximately their center.

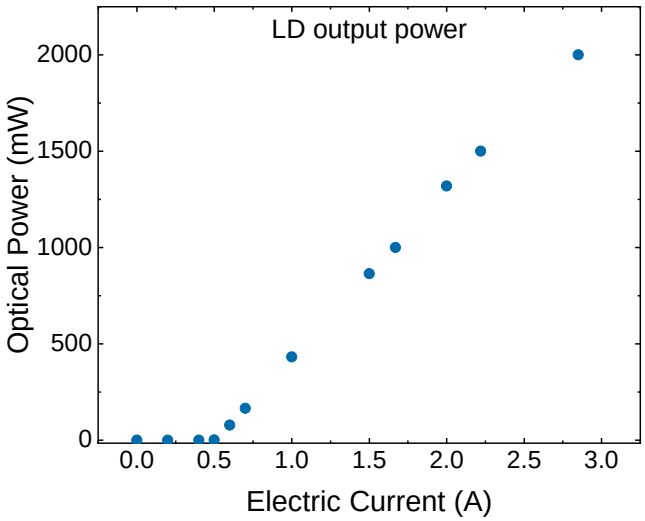

Fig. 4.6. Optical output power of the laser diode as a function of the supplied electrical current. A typical linear diode behaviour can be observed, with a threshold at 0.7 A. The diode can stand currents up to 11.5 A with a corresponding 9 W output power, but values above the ones shown in this plot are not needed for the current application.

of the amplifier, which is always a desirable feature in any amplifier, and denotes that we are not saturating the gain.

After losses in the compressor, mostly in the Faraday isolator and the grating pair, the effective net gain is reduced to 3. Losses in the isolator usually arise even for perfect alignment and polarization matching due to the quality of the polarizers, residual reflections from the anti-reflection coatings and imperfect 45° rotation in the Faraday rotator. In a similar manner, the pair of gratings introduce unavoidable losses since part of the power is lost in other orders of diffraction than the one used. Nevertheless, it should be reminded that it is not the average power what we are interested in, but the peak pulse power. Therefore, the pulse compression is a crucial condition for evaluating the quality of the amplifier, and ultimately the ability to span an octave of frequencies in the f-$2f$ interferometer will be the key to confirm the success of the fiber amplifier for this application (we will verify this in Chapter 5).

As we mentioned in Section 4.2.1, the central wavelength of the LD's emission depends on the temperature of the diode. Since the absorption peak at 975 nm in the gain medium is quite narrow (Fig. 4.1), a slight deviation from this wavelength may cause large changes in the population inversion, and thus in the gain of the amplifier. This is confirmed in Fig. 4.8, where the temperature of the diode was manually changed using the PID controller that stabilizes the temperature of the pump system as described in Section 4.2.1. A very significant change in the amplified power, of a factor 2-3 can be observed when varying the temperature of the LD while keeping the supply current fixed. In both cases, for currents of 2 A and 1 A, the amplified optical power increases with increasing temperature until it starts reaching a saturation point, where possibly the wavelength does not change significantly[11]. The change is such, that in the 2 A case we find the amplifier in the optical attenuator regime for low temperatures, but achieve a gain factor of 3.4 at 40 °C. From this observations, it

[11] Higher temperatures were not available with this temperature controller.

was decided to operate the fiber amplifier at an LD temperature of 40 °C, at the cost of reducing the diode's lifetime in the long term.

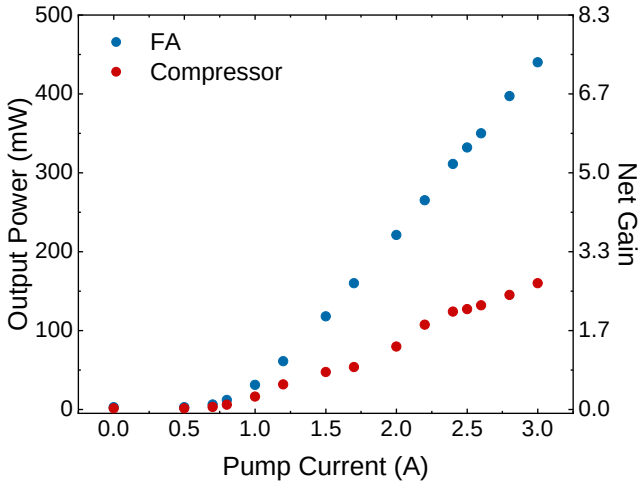

Fig. 4.7. Amplified optical power out of the fiber amplifier (FA) and pulse compressor. The blue data points are measured right after the FA's output GRIN lens, and the red ones after the compressor's M4 mirror (see Figs. 4.4 and 4.5). The desired linear behaviour is observed, without hints of saturation. The net gain shown is the ratio between the output power and an input power of 60 mW. The temperature of the LD is set to 40 °C

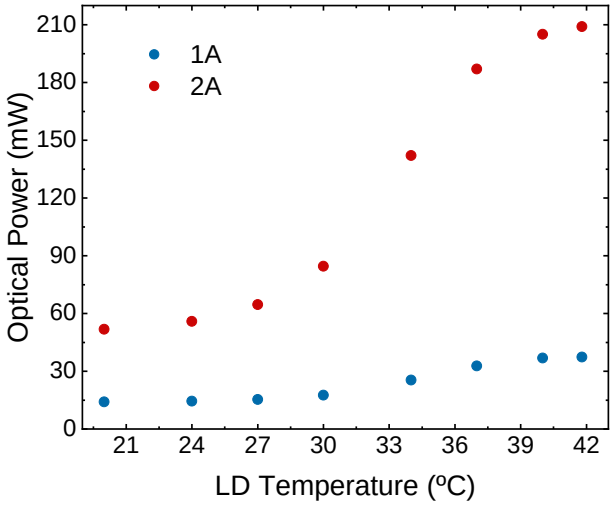

Fig. 4.8. Amplified optical power vs. laser diode temperature for constant supply current. In blue, power measurements for a current of 1 A, and in red for 2 A. In both cases, amplification is enhanced with increasing temperature until a saturation point seems to be reached. The measurements were made before the pulse compressor.

4.3.2 Characterization of the pulses after compression

We will study now not the average properties of the laser beam, such as the power, but those of the single pulses. Our goal is to make sure that the pulse compressor is indeed compressing the pulses, and quantify their temporal width. This can in principle be done by measuring their autocorrelation function (ACF) with an *autocorrelator*, but a full characterization of the pulses is achievable with a FROG system (Frequency-resolved optical gating system). The difference is that, while the ACF

contains information about the pulse time-width, it does not contain enough information about its phase to reliably recreate the exact pulse shape or even give an exact numerical value of its time-width. Still, it can be used for optimizing the pulse compressor (the distance b between the grating pair), because minimizing the width of the ACF generally leads to minimization of the pulse time-width. As a matter of fact, the optimization of the compressor was done with an autocorrelator, but fortunately a FROG system was available for a few days, which allowed a complete characterization of the pulses.

In short, the FROG system measures the optical spectrum of the second-harmonic light generated by overlapping two pulses in a frequency-doubling crystal. Measuring this SHG spectrum as a function of the time delay between the pulses generates a time-frequency 2D trace that contains information about the amplitude and phase of the pulse in both time and frequency domains[12]. This information is automatically retrieved with a software offered by the manufacturer, MesaPhotonics, by solving the so-called *two-dimensional phase-retrieval problem*.

An important feature of this system is that it provides feedback about the validity of the results via the FROG trace error, which is assumed to be indicative of reliable results when $< 1\%$. In a few words, the FROG trace is an $N \times N$ array of points, that is used to calculate N intensity and N phase points, i.e. $2N$ total. There are thus more degrees of freedom in the FROG trace than in the pulse, and the pulse intensity and phase are over-determined. This allows for re-calculation of a "retrieved" FROG trace that can be compared to the measured one, as a manner of checking whether the software has captured all relevant features of the trace for the reconstruction of the pulse. The fidelity of the reconstruction is highly dependent on a correct alignment of the FROG setup[13] and on the correct tuning of some software parameters. A good starting point is making sure the trace is centered at, and symmetric from, zero time delay, but comparing with the retrieved trace is the key test, as well as minimizing the calculated FROG trace error.

A FROG measurement of the pulses after the compressor, with its corresponding measured and retrieved traces, is plotted in Fig. 4.9. We find outstanding agreement between both traces, and both demonstrate good symmetry properties. This is an indicator of the excellent quality of the measurement and retrieval, and also proves the superb stability of the pulses.

As we said, from these traces, the commercial software reconstructs the intensity and phase profiles in both time and frequency domains. From observing the real-time calculated pulse width, one can optimize the grating distance that minimizes the time-width. The intensity and phase of the minimum-width pulses in both time and frequency domains are shown in Fig. 4.10. The most noticeable feature of the pulses is that most of their power has been compressed to 65 fs, which is more than 20 times narrower than the 1.5 ps estimated width after the fiber amplifier. This proves the excellent performance of the pulse compressor. This width is even shorter than the presumed 100 fs of the pulses emitted by the Yb:KYW oscillator. This is not strange, since the pulses are most likely chirped when they are emitted, so that they admit further compression. Also, as we can see in Fig. 4.10 (b), the spectrum is somehow wider than the seed spectrum before the amplifier (shown in Fig. 2.5), which means the amplifier has introduced new frequencies via self-phase modulation. This also

[12] It effectively contains a frequency-resolved ACF.

[13] In a commercial system this shouldn't be necessary often, but due to some special circumstances the FROG setup had to be dismounted and realigned.

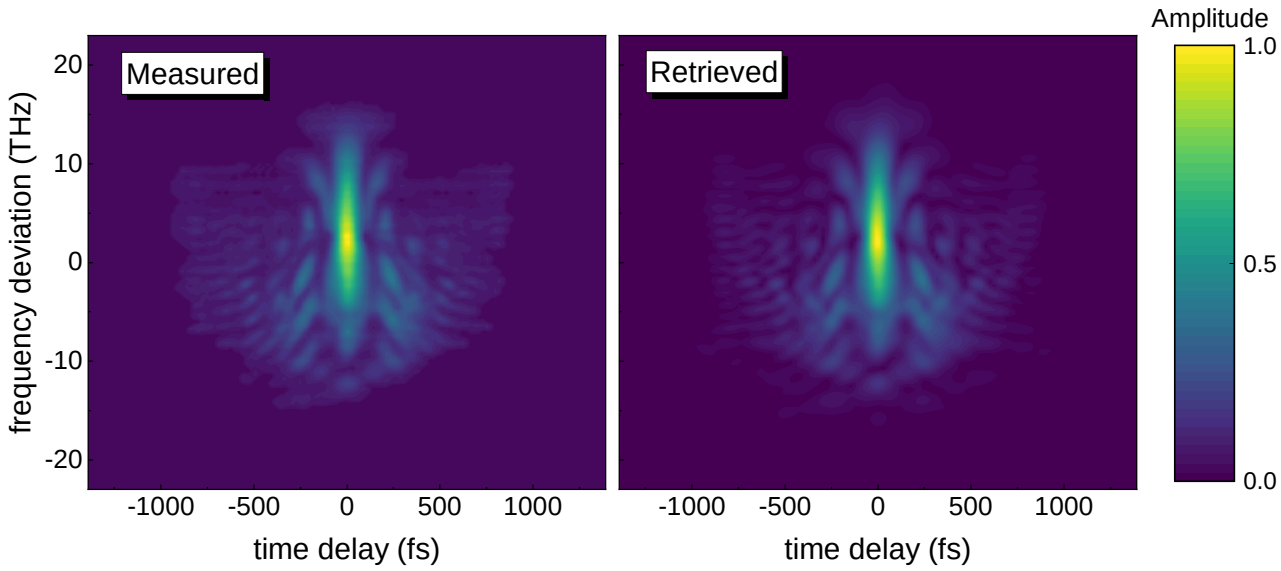

Fig. 4.9. Measured and retrieved FROG traces from compressed pulses. The measured time-frequency array contains all the information needed to (over) characterise the light pulses. The retrieved trace captures a very high level of detail and is in excellent agreement with the measured trace. A FROG trace error of 0.52% is also indicative of a good measurement and pulse reconstruction, and also good pulse stability.

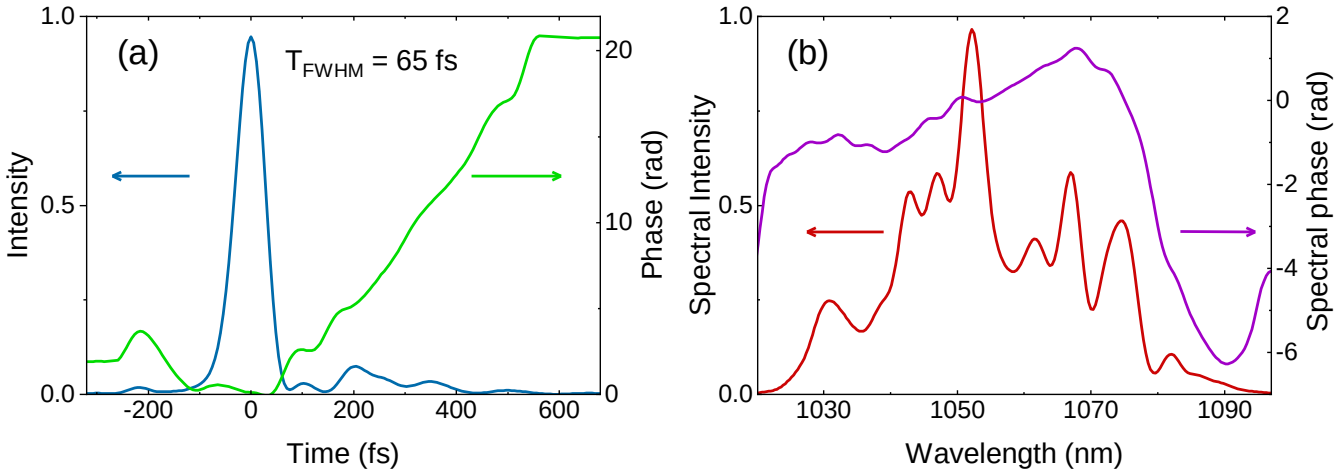

Fig. 4.10. Intensity and phase of compressed pulses in time and frequency domains. **(a) Time domain.** Intensity profile in blue and phase in green. The pulse is mostly forming a smooth main peak with a width of $T_{\mathrm{FWHM}} = 65$ fs, meaning it is more than 20 times narrower than before compression. The wiggling tail at longer time delays is characteristic from third order dispersion (TOD). **(b) Frequency domain.** Spectral intensity (in wavelengths) in red and spectral phase in purple. The spectrum spans more frequencies than the original Yb:KYW seed spectrum, which is a sign of non-linearities (SPM) in the Yb-doped amplifier. The fact that the spectral phase is not completely flat nor linear, means the pulse width is still not Fourier-limited.

leads to think that, from a wider spectrum, we can compress the pulses further than their "original" widths. Looking at the spectral phase, we can see that it is not completely flat nor linear, meaning there is still some chirp in the pulse and its width is still not Fourier limited. In fact, it seems to be slightly convex upwards, which leads to think the main contribution to the chirp is linear.

Chapter 5

f-2f Interferometer

The f-2f interferometer is the core of the present work. As it was stated in the introduction, controlling f_0 is essential for gaining full control over the frequency comb and succeeding in applications such as high precision spectroscopy. Optical heterodyne detection of the beat note generated by mixing f_{2n} with $2f_n$ modes of the comb, in what is called f-2f interferometry, is the standard technique for measuring f_0.

With the purpose of stabilizing an Yb:KYW mode-locked laser for future high-precision spectroscopy in He^+, an f-2f interferometer was built for this work. Throughout this chapter, the theory behind heterodyne detection and f-2f interferometry will be further explained, a detailed description of the experimental setup for octave spanning and the interferometer will be made, and results proving the operational success of the f-2f interferometer will be presented.

5.1 Theoretical background

5.1.1 Optical heterodyne detection

The concept of optical heterodyne detection lies on the principle of superposition of two electromagnetic waves E_1 and E_2 with frequencies ω_1 and ω_2. Let us assume that these are optical frequencies which are relatively close to each other. For instance, they can be in the hundreds of terahertz range ($100 \cdot 10^{12}$ Hz) and their difference in the tens of megahertz range ($10 \cdot 10^6$ Hz). If they are superimposed on a beamsplitter, the output is a superposition of both waves travelling collinearly

$$\mathbf{E}(\mathbf{t}) = \mathbf{E}_1 \cos(\omega_1 t) + \mathbf{E}_2 \cos(\omega_2 t) \ , \tag{5.1}$$

where the two polarizations $\mathbf{E}_1$ and $\mathbf{E}_2$ are naturally perpendicular to the direction of propagation and form a relative angle θ. In this simple equation we are already assuming some conditions for interference, which is that both waves must be spatially coherent, so that their (laser beam) intensity profiles are overlapped, and that their wavefronts must match at the interference plane. Now, if we send their superposition to a photodetector, the device will create a current proportional to the optical intensity, which is proportional to the squared amplitude

$$E^2(t) = E_1^2 \cos^2(\omega_1 t) + E_2^2 \cos^2(\omega_2 t) + 2\mathbf{E}_1 \cdot \mathbf{E}_2 \cos(\omega_1 t) \cos(\omega_2 t) \ . \tag{5.2}$$

The cross-term already shows how both waves interfere to modulate each other, but this can be seen more explicitly by using some trigonometric relations[1]

$$E^2(t) = E_1^2\cos^2(\omega_1 t) + E_2^2\cos^2(\omega_2 t) + \mathbf{E}_1 \cdot \mathbf{E}_2[\cos((\omega_1+\omega_2)t) + \cos((\omega_1-\omega_2)t)] \,. \tag{5.3}$$

Therefore, the two waves interfere by creating two components at the sum and difference frequencies $\omega_1 \pm \omega_2$. Now, one must consider that photodetectors cannot resolve optical frequencies, because their oscillations are much faster than the detectors response time. This means, the electrical signal generated by the detector is proportional to Eq. 5.3, but averaged over its response time. Effectively, this means that terms oscillating at optical frequencies such as ω_1, ω_2 and $\omega_1+\omega_2$ are time averaged, leaving

$$\langle E^2(t)\rangle = \frac{1}{2}E_1^2 + \frac{1}{2}E_2^2 + \mathbf{E}_1 \cdot \mathbf{E}_2[\cos((\omega_1-\omega_2)t)] \,. \tag{5.4}$$

Therefore, the only time dependence that the detector is responsive to, is that at the *beatnote* frequency $\omega_1 - \omega_2$, presumed to be some tens of megahertz or gigahertz. Note that the scalar product of the polarizations $\mathbf{E}_1 \cdot \mathbf{E}_2 = E_1 E_2 \cos(\theta)$ means that the modulation of the detector's output will be maximum for parallel polarizations, and zero for orthogonal polarizations, assuming linearly polarized light.

With this detection scheme one can compare two optical frequencies that would otherwise be unresolvable by electronic systems, allowing for measuring and referencing optical frequencies by beating them with other known optical signals. In other words, having a very stable optical oscillator, one can reference a less stable source to it by measuring and locking their beatnote, thus translating the stability from one system to the other. This is what makes the frequency comb so useful in frequency metrology, because once the comb is referenced to a highly stable RF or optical source, one can translate this stability and accuracy from one domain to the other, allowing for synthesis of highly stable RF or optical light for referencing, direct spectroscopy, etc.

5.1.2 f-2f self referencing

Even though heterodyne detection is usually explained as the interference of light from two independent optical sources, in the case of f-2f interferometry, ω_1 and ω_2 are frequencies from both extremes of a comb spectrum that is broad enough to span an octave of frequencies. This why this technique is also called f-2f *self-referencing*.

Let us assume we have an octave spanning comb spectrum comprising frequencies f_n and f_{2n}, as described by the comb equation (Eq. 1.2 in the Introduction):

$$f_n = nf_r + f_0 \tag{5.5}$$
$$f_{2n} = 2nf_r + f_0 \,. \tag{5.6}$$

[1] $\cos(a)\cos(b) = \frac{1}{2}(\cos(a-b) + \cos(a+b))$

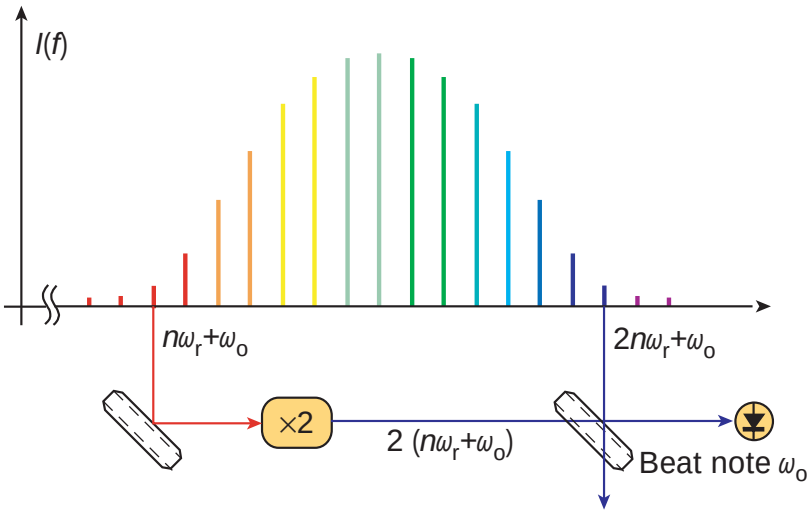

Fig. 5.1. Idea of f-2f interferometry. A mode ω_n, from the low-frequency side of the comb spectrum, is frequency doubled and made to interfere with a mode ω_{2n} from the high-energy side of the spectrum. The resultant beatnote is the carrier-envelope offset frequency f_0. From Th. Udem et al. [16].

By some means, such as a dichroic mirror, we spatially separate the spectrum so that frequencies below a frequency threshold ($f_n < f_{\text{thr}}$) are sent to one arm of the interferometer, and frequencies over that threshold ($f_{2n} > f_{\text{thr}}$) are sent to the other arm. Then, the lower-frequency beam is frequency doubled via second-harmonic generation (SHG) in a non-linear crystal. This turns the frequencies f_n into

$$2f_n = 2(nf_r + f_0)\ . \tag{5.7}$$

Then, both interferometer arms meet again, overlapping the lower-frequency and higher-frequency beams in a beamsplitter, in such a way that they are matched spatially and temporally[2]. The overlapped beam is sent into a photodetector, that will detect the beatnote as explained in Section 5.1.1 (Eq. 5.4). Interestingly, the beatnote between Eqs. 5.7 and 5.6 is

$$2f_n - f_{2n} = 2(nf_r + f_0) - 2nf_r + f_0 = f_0\ . \tag{5.8}$$

Consequently, what we measure at the photodetector is a sinusoidal signal at the carrier-envelope offset frequency f_0. If this electronic signal is sent to a spectrum analyzer, we would expect to obtain a spectrum with a line at f_0, only departing from a delta because of noise.

Beat spectrum

According to everything explained until now, one may expect to measure a spectrum consisting on a single delta line centered at f_0. This is because we have been conducting the explanation focusing on the beating of the $2f_n$ and f_{2n} modes, but as a matter of fact many other lines may satisfy the interference conditions of spatial

[2]This means that the light beams are aligned to the same axis and the pulses from both beams are overlapped. In practice this is done by optimizing the beatnote detection signal.

and temporal coherence, generating beatnotes that will also appear in the spectrum. Let us even forget for a while about the interferometer device and think about what will happen if we send our pulsed beam right out of the MLL onto a photodetector. Since the pulses are repeated periodically at f_r, the detector signal will correspondingly be a pulse train that, when Fourier transformed in the spectrum analyzer, will produce a comb of signals separated by f_r. This is understood from the point of view of the time-domain, but we can also look at it from the frequency-domain. The point is that the comb modes in the pulse can also beat with each other. For instance, we can look at the beat from neighbouring modes

$$\begin{aligned} f_{n+1} - f_n &= ((n+1)f_r + f_0) - (nf_r + f_0) = f_r \\ f_{n+2} - f_n &= ((n+2)f_r + f_0) - (nf_r + f_0) = 2f_r \\ &\dots \\ f_{n+m} - f_n &= ((n+m)f_r + f_0) - (nf_r + f_0) = mf_r \,. \end{aligned} \tag{5.9}$$

Therefore, even without an interferometer, the repetition rate will appear in the photodetector spectrum. In this sense, measuring the optical comb spectrum through an electronic photodetector is like translating the comb to the RF region near the origin of frequencies, since m starts from the unit.

So far we have seen how a comb structure is always implicit in a pulsed beam, and how f_0 is accessed via f-2f interferometry. The last step to complete our understanding of the beat spectrum after the f-2f interferometer, is to realize that f_r and f_0 can also beat. In fact, since they are both RF, they make two beatnotes, by keeping both the sum and difference terms in Eq. 5.3 [3]. Finally, we can write down an expression that describes the measured beat spectrum

$$mf_r \pm f_0 \quad \text{for} \quad m = 0, 1, 2 \dots \tag{5.10}$$

This means we will find comb lines at f_0, $f_r - f_0$, f_r, $f_r + f_0$, etc. in the RF region. One may also note that, in the f-2f interferometer, there will be beatings of the type $2f_{n+1} - 2f_{2n} = 2f_r + f_0$, but they do not add new lines to the spectrum described by Eq. 5.10.

5.2 Experimental setup

The f-2f experimental setup can be divided in two main parts: the octave-spanning section, with the photonic-crystal fiber as the main element, and the interferometry section, which has a Mach-Zehnder geometry with SHG in one of its arms. We will now proceed to a detailed description of these sections and all the elements they comprise.

[3] Remember that we originally discarded the sum term because optical oscillations are too fast to resolve, which is not the case now

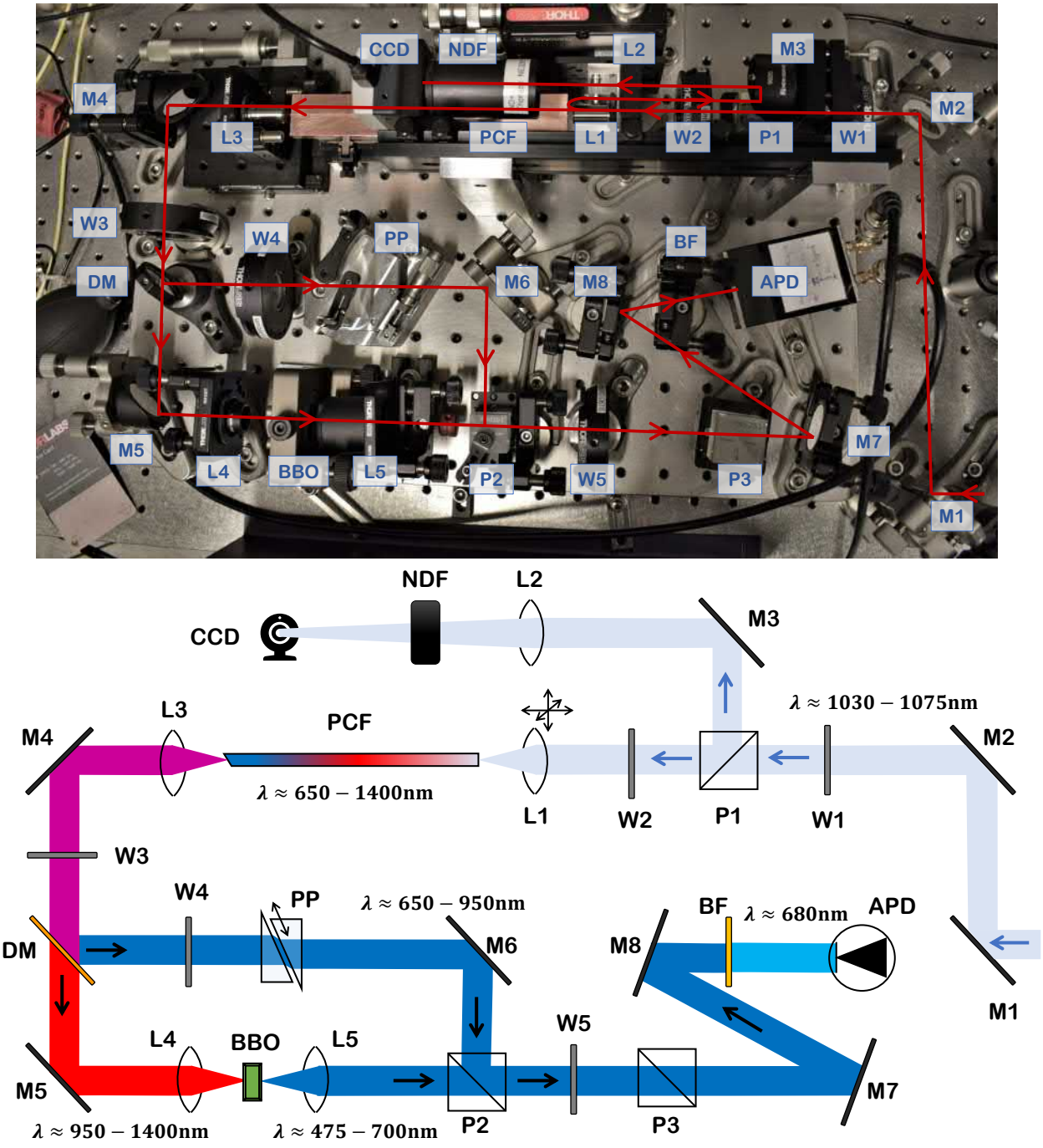

Fig. 5.2. Actual picture (top) and schematic diagram (bottom) of the f-2f setup. The incoming beam is coupled into the PCF with the help of two mirrors (M1 and M2) and a $f = 6.24$ mm lens on a 3-axis stage (L1). A $\lambda/2$-plate (W1) and a PBS (P1) control the transmitted power. Light reflected back from the PCF input face is sent by P1 to an imaging system. The spectrum is broadened in the PCF via SPM and it is sent towards the interferometer. A dichroic mirror (DM) separates the short and long wavelength components with a cut-on wavelength of 950 nm. A BBO crystal produces SHG in the IR arm. A prism pair (PP) with one of the prisms on a linear stage permits changing the optical path length of the red arm, for temporal overlapping of the pulses at the P2 PBS, where both arms are recombined and spatially overlapped. A $\lambda/2$-plate (W5) and a PBS (P3) project all components to the same polarization axis, and a bandpass optical filter (BF) blocks all wavelengths except for those at 680 ± 10 nm. An avalanche photodetector (APD) collects the light and sends its output current to a spectrum analyzer. The IR arm is sketched in red color and the red arm in blue for a clearer visualization.

5.2.1 Octave-spanning section

The octave-spanning section is aimed to broadening the comb spectrum in a controlled way up to an octave of frequencies. This is achieved via self-phase modulation in a photonic-crystal fiber (PCF). Photonic-crystal or micro-structured fibers are optical fibers that obtain their waveguide properties from an arrangement of cylindrical air holes that extend along the fiber parallel to its optical axis, surrounding the fiber core. The core can either be a missing hole in the arrangement (solid core) or a hole of a different size or position (hollow core), and wave-guiding can occur via one of two mechanisms: effective-index guidance (high-index core) and photonic-bandgap guidance (low-index core). This air-hole structure is used for tuning the zero-dispersion wavelength of the fiber, such that pulses propagating at this wavelength do not stretch from GVD and can keep a short duration over long propagation distances. This, along with a narrow mode-field diameter on the order of 3 - 4 μm, keeps high optical peak intensities in the fiber and enhances non-linear processes.

Different geometrical arrangements of the micro-structured cladding may lead to different sets of properties, therefore the selection of a specific PCF has to be studied within each application. In this work, two different PCFs from NKT Photonics were tested for viability of octave-spanning from the narrow spectrum of the Yb:KYW laser. These are the SC-3.7-975 and the SC-5.0-1040, whose distinctive characteristics are their mode-field diameters, 3.3 ± 0.3 μm and 4.2 ± 0.2 μm, and their zero-dispersion wavelengths 975 ± 15 nm and 1040 ± 15 nm respectively, as well as different cladding structures.

Coupling system

The system for coupling light into the PCF core is rather sophisticated. The reader should check Fig. 5.2 for reference. Two mirrors, M1 and M2, make a rough alignment of the incoming beam (from the pulse compressor) towards the PCF optical axis. A $\lambda/2$-plate (W1) along with a polarizing beamsplitter (P1) allow for adjusting the transmitted power. Polarizing beamsplitters (PBS), are polarizer cubes that transmit light that is linearly polarized in a certain axis, and reflect light polarized in the orthogonal direction. Thus, rotating the polarization of the beam with a $\lambda/2$-plate one can control the transmitted power. A second $\lambda/2$-plate (W2) allows for selecting a convenient polarization axis for propagation in the PCF.

The L1 lens is a $f = 6.24$ mm focusing lens that couples the laser beam into the PCF. The lens is chosen to maximize the coupling efficiency, attending to the beam waist and the fiber core size. It can be shown that a collimated gaussian beam with waist w can be focused down to a waist w', with a lens of focal length f, following the next expression [60]

$$w' = \frac{\lambda_c}{\pi}\frac{f}{w} \tag{5.11}$$

where λ_c is the laser central wavelength. The laser beam waist was measured to be $w = 1.4$ mm[4] with a CCD camera and specialized software. Therefore, the $f = 6.24$ mm lens focuses the beam to a $w' = 1.46$ μm waist according to Eq. 5.11, thus a 2.92 μm diameter, which is similar to both the core sizes of the PCFs considered. In

[4]The beam waist is defined here as the radius at which the intensity drops to $1/e^2$ from its maximum.

order to control the beam alignment accurately, the lens was mounted on a 3-axis stage, which allows for manually adjusting the spatial position of the lens in the three directions with sub-millimeter precision.

The system described so far is enough to couple the laser beam to the PCF, but to have a visual reference while aligning, an imaging system is also used. This consists in collecting the back-reflected light from the PCF input facet, which travels back through L1 and W2, and is reflected upwards by P1. A mirror (M3) and lens (L2) align and focus this light into a CCD camera that is connected to a computer for displaying the image. A neutral density filter (NDF) is used for power attenuation. What one observes, is the live-image of the PCF input face from the "beam's perspective", so that one can visually track the beam position with respect to the fiber core and its surroundings while aligning.

The usual alignment protocol is the following, considering the laser beam is roughly aligned, but may not even be hitting the PCF input facet. One starts adjusting the M1 and M2 mirrors searching for visual references in the imaging system display. These references may firstly be on the PCF holder, and at some point the PCF itself. For this process one may start with a L1-to-PCF distance somehow longer than its focal length, but once the PCF is found, the distance can be adjusted to form a clear and focused image on the display. This is realized when the air holes look sharply defined in the screen. Then, one must find the position with the L1 3-axis stage that better aligns the beam with the fiber core. On the screen display, this is usually seen as a bright spot on the core position. At this point some light should be coupled into the core and propagating through the fiber, such that it should be detectable with a power meter at the fiber end. Then, one can optimize the coupling by maximizing the output power. The alignment can be tuned with M1, M2 and L1, with their corresponding $2 + 2 + 3 = 7$ degrees of freedom, even though strictly speaking only M1, M2 and the longitudinal displacement of L1 are needed. Usually one has to patiently go back and forth adjusting these three elements in the vertical and horizontal directions, but gradually reducing the L1-to-PCF distance[5]. It is recommended to perform this whole operation with low laser power, which can be adjusted by rotating the half-waveplate W1 to a convenient position.

After propagation in the PCF, the output beam is highly divergent and is thus recollimated by another $f = 6.24$ mm lens (L3), and sent to the interferometry section by the M4 mirror. The L3 lens is mounted on a linear stage for fine tuning its distance from the PCF and optimizing the beam collimation.

The PCF

As stated, different PCFs were tested for finding the appropriate configuration for octave spanning. Segments of different lengths from the SC-3.7-975 and the SC-5.0-1040 from NKT Photonics were tested. Each segment needs to be prepared carefully for correct performance, meaning the input and output facets need to be precisely cleaved. While the input facet can be cleaved in a straight angle with respect to the optical axis, the output facet is always cleaved in a $\sim 8^\circ$ angle with respect to the vertical, such that light cannot be partially back-reflected and travel backwards in the PCF. This was done with an angle-cleaver. When dealing with the fibers after cleaving, one must make sure the face ends do not make contact with anything, to

[5]Once L1 is pretty close to the PCF, the image display stops being a sharp image of the PCF input facet, but rather a diffraction pattern from the micro-structured cladding array.

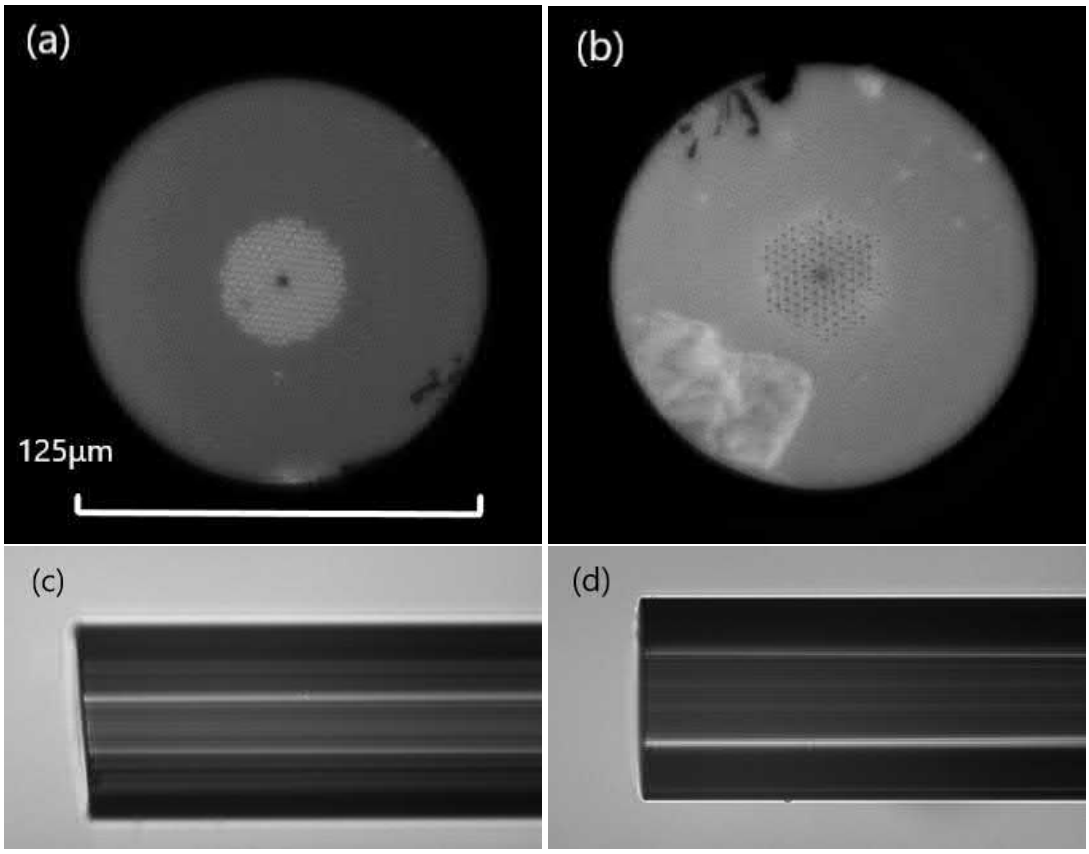

Fig. 5.3. Optical microscope images of photonic-crystal fibers. **(a)** and **(b)** show a frontal perspective of the SC-975 and SC-1040 fibers' input facet respectively. Note the different micro-structured air-hole arrays, with the core at the center. The cladding diameter is 125 μm, and some damage can be seen in the SC-1040 cladding. **(c)** and **(d)** show a side perspective of the output and input ends of the SC-975 fiber respectively. The output end is cleaved at $\sim 8^{\circ}$ while the input end has a straight cleave.

avoid dust particles or scratching. In fact, for checking the quality of the cleaving, an optical microscope part of a fiber splicer is used to obtain frontal and side images of the fiber ends. Some examples of these images are shown in Fig. 5.3.

In order to try different fiber lengths in the setup, a two-segment custom fiber holder was initially used. The two segments were mounted on a rail, so that the effective fiber holder length could be changed. The holder consisted of two copper blocks with a central V-shaped groove to accommodate the fiber in a relatively fixed position. A vertical cylindrical hole at each end of the blocks could fit a glass cylinder with a horizontal slit, such that the ends of the fiber could fit on the slits and be pressed down by the glass cylinders' own weight, and consequently fixed at the end points of the blocks. Additionally, the fibers were taped to the copper blocks for further stabilization. The fibers must be as still as possible, for keeping the alignment conditions on both the input (coupling) and output (subsequent interferometer alignment) ends.

When the appropriate PCF and its length was established (this will be discussed in Section 5.3.1), a new and final fiber holder was designed. This holder consists of a single copper block of a length similar to that of the fiber, but $\sim$ 1 mm shorter so that the end facets of the fiber are not in contact with it. It also has a V-shaped groove for fiber accommodation, but the glass-cylinder system for holding the fiber ends was

substituted by a $\sim 60\ \mu$m[6] step that serves as a support for the un-coated part of the fiber, in a way that avoids vertical bending, and permits fixing the fiber with tape.

5.2.2 Interferometry section

One may wonder why an interferometer is needed at all. Why can't we just send the octave spanning spectrum through a SHG crystal so that the frequency doubled part interferes with the fundamental spectrum, also transmitted through the crystal. The answer lies in temporal overlap. Since the group velocity in the crystal is different for the fundamental and doubled frequencies, the temporal overlapping of the different components within the pulse is lost. It is thus necessary to send them through different arms and control their relative phase in order to achieve interference.

A dichroic mirror with a cut-on wavelength of 950 nm transmits longer wavelengths towards M5 (we will call this the IR arm) and reflects shorter wavelengths towards the prism pair (PP, in the red arm). An image of the visible light out of the PCF can be seen in Fig. 5.4.

In the IR arm, the beam is tightly focused by a short focal-length lens (L4), so that high intensity is achieved at the BBO[7] crystal for efficient second-harmonic generation (SHG). Second-harmonic generation, also known as frequency doubling, is a non-linear process by which two photons of frequency ω are destroyed to create a single photon of frequency 2ω, therefore conserving energy. This process can occur in materials that lack inversion symmetry and have a non-zero second order susceptibility $\chi^{(2)}$. For SHG to happen, a condition known as *phase-matching* must be satisfied, which consists in keeping a phase relation between the fundamental and second-harmonic waves along the optical axis of the crystal such that all the frequency doubled photons interfere constructively to create a coherent wave.

This effectively imposes a condition on the incidence angle and polarization direction of the laser beam with respect to the non-linear crystal (BBO). For this reason, the BBO crystal is mounted in a rotational stage and the W3 $\lambda/2$ plate can also rotate the polarization of the beam to the direction that maximizes the frequency doubled light, which can simply be seen on a white piece of paper in the visible range. After the BBO crystal, the beam is re-collimated by the L5 lens, and sent towards the P2 polarizing beamsplitter, where the two interferometer arms are reunited. The polarization must also be chosen in such a way that the beam is mostly transmitted through P2.

In the red arm, a prism pair (PP) is used for effectively elongating the optical path length and introducing the right phase delay for temporal matching between the two interferometer arms, i.e. pulse overlapping at P2. One of the prisms is mounted on a linear stage, so that the optical path length can be tuned to find and maximize the interferometric signal. The W4 waveplate selects the right polarization for maximizing reflection at the P2 beamsplitter.

The alignment between the two arms must be extremely precise for achieving interference. First, the length of the arms should be the same within the length range that the prism pair can compensate (~ 5 mm). In fact, since the prisms add some effective length, the red arm should be just slightly shorter. Additionally, the beams from both arms need to be spatially overlapped from P2 on. This means that their spatial

[6] This is the distance between the outer coating surface and the cladding of the PCF.
[7] The BBO crystal one of the most common materials used for type I SHG.

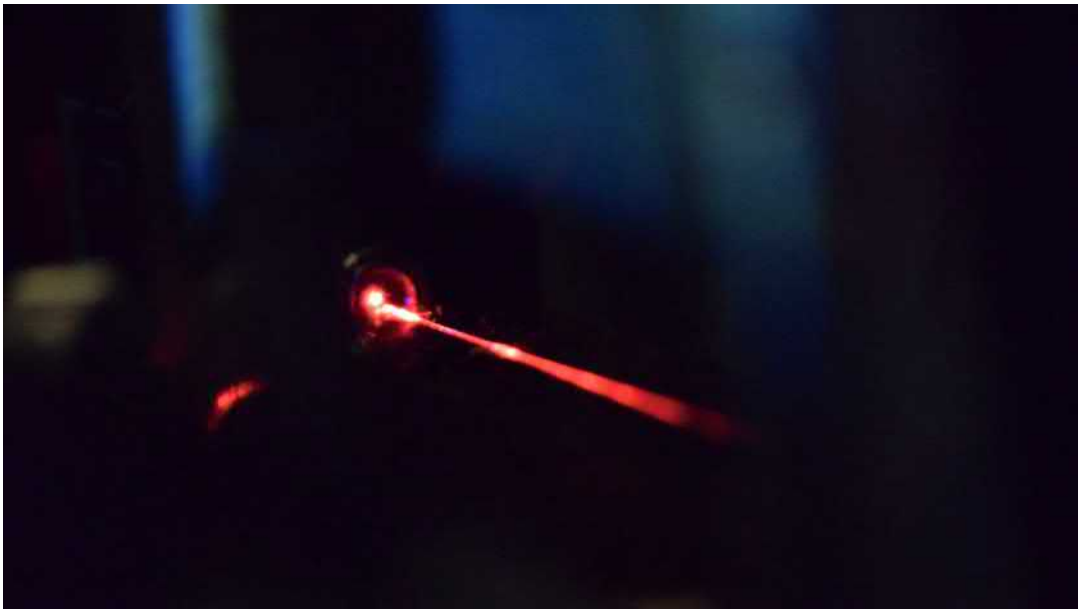

Fig. 5.4. Photonic-crystal fiber, generating red light via continuous broadening from IR. Infrared light with a spectrum centered at 1050 nm (see Fig. 4.10 (b)) enters the SC-975 fiber from the bottom right-hand corner in the picture, and red light is gradually generated via SPM. Note that SPM broadens the spectrum continuously and symmetrically, so that also longer wavelength IR light is generated. A collimating lens (L3) can be seen by the fiber end.

profiles are to be matched along their path until the photodetector. This is practically done by fixing the alignment of the frequency-doubled beam, and adjusting the alignment of the red beam with M6 and P2 so that both beams are matched. To check the correct overlapping of the beams, one can choose two reference points separated by a relatively long distance (right at P2's output and a distant wall, for instance) and make sure the beams are overlapped at both positions.

After P2, even though they are overlapped, the components coming from the two red and IR arms have orthogonal polarizations[8]. For that reason, a $\lambda/2$ plate (W5) and a polarizing beamsplitter (P3) project both polarizations onto the same axis, accomplishing every condition for optimal interference.

At this point we have a broad spectrum $\lambda \approx 475$ - 950 nm, but the f_0 beatnote is only contained in the narrow band that corresponds to the f_{2n} and $2f_n$ frequencies in the original spectrum, now corresponding to frequencies around 675 nm. If we are to maximize the signal-to-noise (S/N) ratio, we would like to filter the rest of the frequencies out, that would only contribute to the noise. This was first done by using a grating in place of the M7 mirror, that acted as a wavelength selector. This would diffract every spectral component in a different angle so that, by rotating the grating and the M8 mirror, one could select the frequencies that were sent to the photodetector (APD). Once the beatnote is found and the S/N ratio maximized, the spectrum at the position of the APD can be measured with an optical spectrometer to realize the frequency that is maximizing the S/N ratio. Knowing that, one can substitute the grating by a regular mirror (M7), and place an optical bandpass filter (BF) in front of the APD to select the appropriate spectral bandwith. After these considerations, the filter was chosen to have a transmission peak at a central wavelength of 680 nm (see Fig. 5.9 (b) in Section 5.3.1) and a FWHM= 10 nm, which improved the S/N ratio

[8] After all, one was transmitted and the other one was reflected by P2.

by roughly 10 dB with respect to the configuration with the grating only, by making a more specific and efficient wavelength selection.

Finally, the avalanche photodetector (APD) collects the light and generates an output current modulated by all the components that lead to Eq. 5.10. This output is sent to an electronic spectrum analyzer that displays the RF beat spectrum.

5.3 Results

5.3.1 Spectral broadening at the PCF

An important first step is to characterize the coupling of the laser beam to the PCF, by measuring the optical power before and after the fiber. This was done with a thermal detector, which is fairly wavelength-insensitive, in contrast with a photodiode detector, and is thus more accurate in measuring the power of broadband light. Comparing the values shown in Fig. 5.5, the coupling is around 60%.

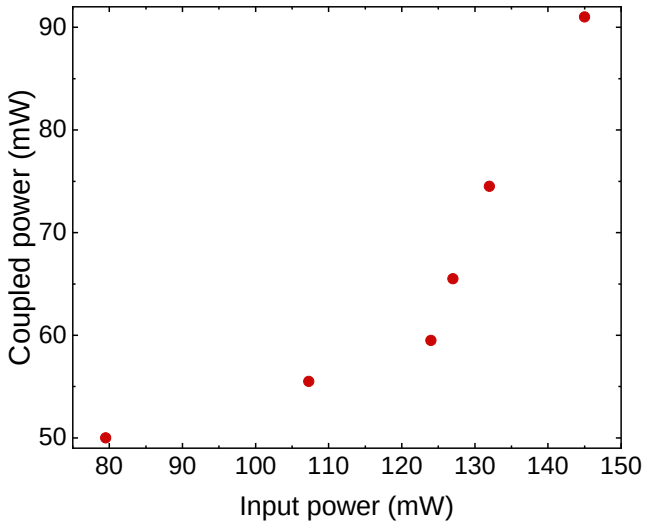

Fig. 5.5. Optical power coupled to the PCF. The optical power is measured at the PCF's output with a thermal detector and compared to that at the input. The maximum coupling efficiency is 60%.

A scanning optical spectrum analyzer is used to measure the spectra at the output of the PCF. For this purpose, the light coming out of the PCF is coupled into a broadband multi-mode optical fiber with a simple coupling system consisting of two mirrors and a focusing lens, and this fiber is then connected to the spectrum analyzer. The spectrum analyzer has some sort of tunable wavelength selector or monochromator, such as a rotating grating, that sends light of a specific wavelength to a photodetector. The spectral intensity is detected and displayed in a screen, as a function of the wavelength.

Optimization of the spectral broadening

Spectra were recorded for both PCF types, the SC-975 and SC-1040, different fiber lengths and optical powers. It must be noted that the first attempts at octave spanning were performed before the fiber amplifier was build. For this reason, with an input power limited to 60 mW, increasingly longer fibers were tested. The longest fiber used was a 22-cm-long SC-975. This length was limited by the available space

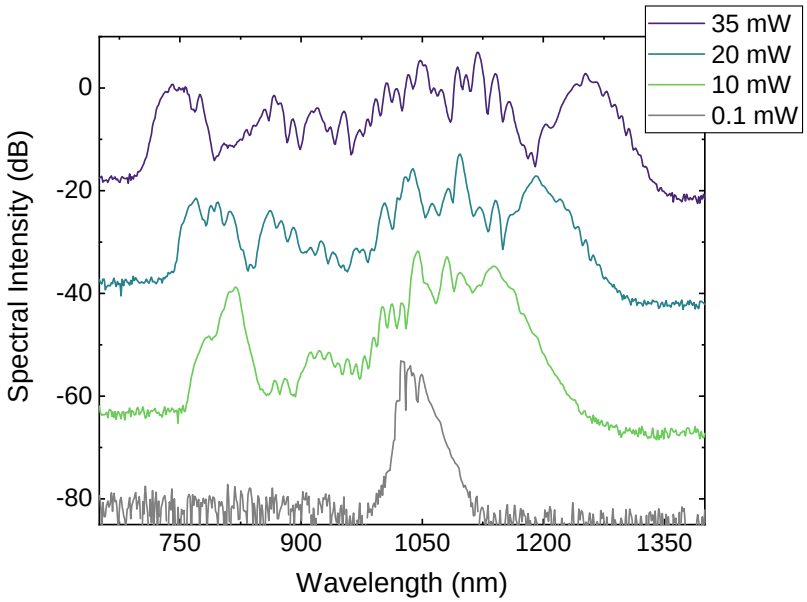

Fig. 5.6. Spectra measured after broadening in a 22-cm long SC-975 PCF. The optical powers in the legend corresponds to the coupled power in the PCF, measured at its output, and controlled by a $\lambda/2$ plate and a PBS (see Fig. 5.2). The spectra were measured with a scanning optical spectrum analyzer. These measurements were made before building the fiber amplifier, so the maximum power is limited by the direct output from the Yb:KYW oscillator (60 mW), and proves to be insufficient for octave spanning. The displayed curves have been offset by -40, -35, -20 and 0 dB (from lower to higher power) for a clear visualization.

in the setup, for placing the fiber without bending excessively. The measured spectra as a function of coupled power can be seen in Fig. 5.6. In this figure, one can see how the spectrum is notably broadened when the average optical power, and thus the pulse peak power, is increased. Typical features from SPM are observed, such as the prominent side lobes, but the complicated structure and asymmetries make it clear that there is an interplay of linear and non-linear effects that play a relevant role in the spectral modulation dynamics. For instance, asymmetry in the relative height of the side lobes appears when third-order dispersion (TOD) dominates over GVD, which happens when propagating close to the zero dispersion wavelength. A similar effect can be originated by *self-steepening*, a high-order non-linear effect, but the fact that the asymmetry is more obvious for lower powers, induces to think that it is indeed due to TOD, so that when the power is increased, SPM is dominant over TOD, and symmetry is somehow recovered.

What is obvious from Fig. 5.6, is that octave spanning was not readily achievable from the Yb:KYW available output power. The broadest spectrum, for a coupled power of 35 mW extends from $\sim$ 730 nm to 1270 nm, therefore less than an octave of frequencies. One could argue that the fiber length could be increased to broaden the spectrum more and more, but since the pulses also broaden in time-domain via GVD (this effect is even enhanced by SPM), the peak power is reduced over distance, so that at some point the spectral broadening is not efficient. This idea is reinforced when comparing the spectra from fiber segments with two different lengths, at the same coupled power, as in Fig. 5.7. Increasing the SC-975 fiber length from 17 cm to 22 cm did not produce a significant increment in the spectral broadening, proving the point that broadening cannot occur indefinitely by using longer PCFs.

The performance in terms of spectral broadening was also compared for the SC-975

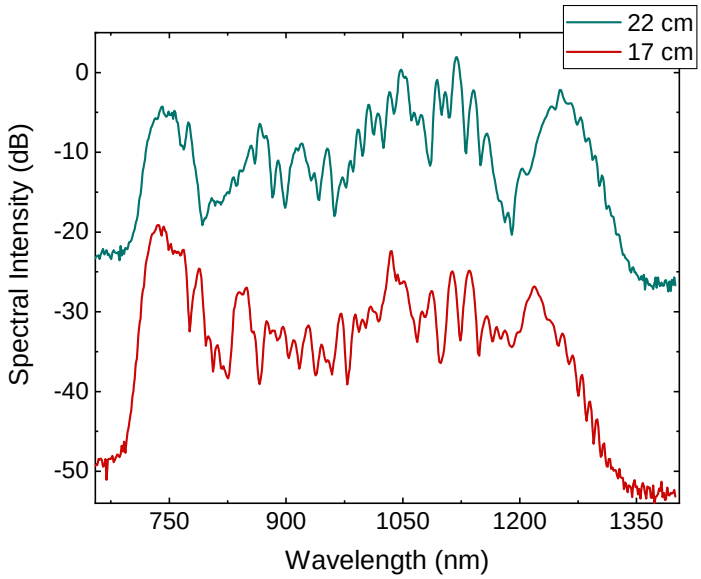

Fig. 5.7. Spectra broadened in SC-975 segments with different lengths, at 35mW coupled power. The broadening is not considerably different between the 22 cm and the 17-cm-long fibers, because after some propagation the pulse peak power is reduced in such a way that SPM does not act significantly. Both curves have a relative offset of 15 dB for a clear visualization.

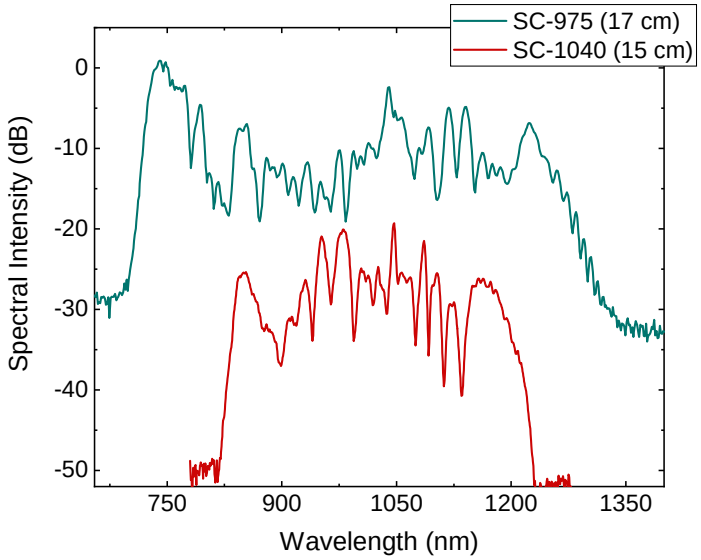

Fig. 5.8. Spectra broadened in SC-975 and SC-1040 segments of similar length, at 35mW coupled power. The SC-975 segment was somewhat longer, which could be the reason of its corresponding spectrum being broader. Still, it does not seem like the SC-1040 would outperform the SC-975 at equal length, therefore the latter was the preferred one for the definitive setup. Both curves have a relative offset of 20 dB for a clear visualization

and the SC-1040 PCFs. Two segments of similar lengths were prepared from both fibers[9], and spectra at the same coupled power were measured. These are shown in Fig. 5.8. It is clear that the spectrum from the SC-975 is broader than the one from the SC-1040. This can partially be due to the SC-975 fiber being slightly longer, but even considering that, the best we could say about the SC-1040 fiber is that it performs similarly to the SC-975.

For this reason, the SC-975 was the preferred and definitive choice for spectral broadening. Also, the results from Fig. 5.6 and 5.7 were decisive for building the fiber amplifier, in order to access higher pulse powers.

Octave spanning

After completing the fiber amplifier, the spectral broadening was studied for average coupled powers 2 or 3 times higher than before, now easily accessible. The measured spectra after a 16-cm-long SC-975 fiber are shown in Fig. 5.9.

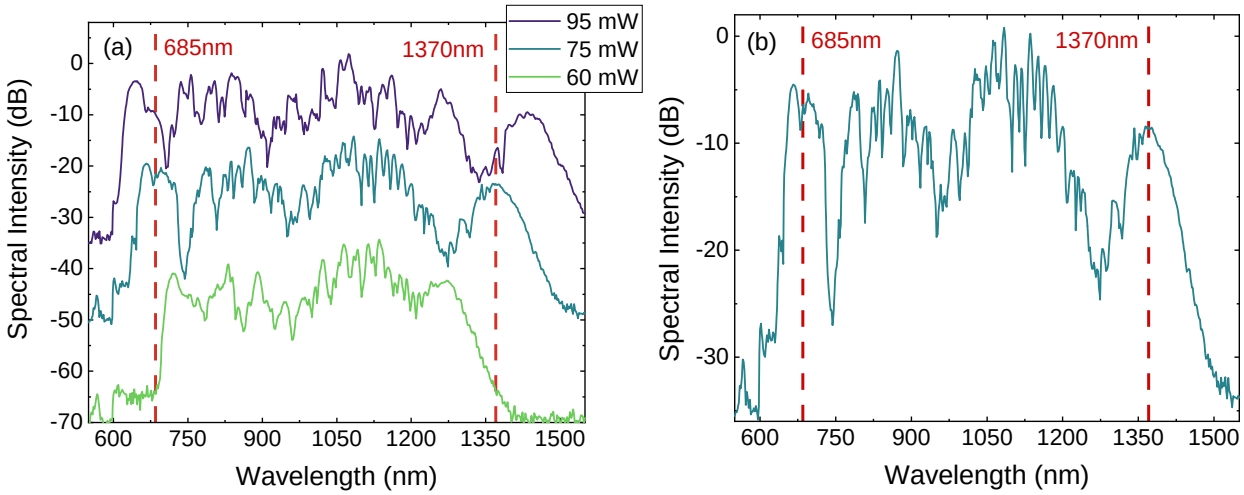

Fig. 5.9. (a) Spectra broadened in a 16 cm SC-975 fiber for different coupled powers. At 75 mW and 95 mW the spectrum spans an octave of frequencies and more, but it is at 75 mW that the f and $2f$ frequencies fall on the spectrum's side lobes, maximizing their intensity. The spectra have been offset by -35, -15 and 0 dB (from lower to higher power) for a clear visualization. **(b) Octave spanning spectrum at a 75 mW coupled power in a 16cm SC-975 PCF.** The f and $2f$ components fall on the spectrum's side lobes and correspond to wavelengths around 1370 nm and 685 nm respectively.

One observes how at 60 mW average coupled power, the spectrum is not broad enough yet for this fiber length, but at 75 mW and higher powers such as 95 mW, the spectrum spans more than an octave of frequencies, achieving the main condition for f-2f interferometry. In order to maximize the spectral power that corresponds to the f and $2f$ components, the ideal broadening is sought to be such that the side lobes of the spectrum fall on the f and $2f$ regions. This is precisely what happens at 75 mW average coupled power, corresponding to a 2.6 A LD current in the amplifier, and a 135 mW average optical power sent into the PCF. The corresponding wavelengths in this case are 1370 nm and 685 nm, and this will be the definitive setup configuration for the f-2f interferometer.

[9]Preparing two different segments of the same length is quite challenging, specially when multiple cleaving attempts may be made to achieve the appropriate quality in the fiber end facets.

5.3.2 Beat note detection

All our efforts so far were leading to the detection of the carrier-envelope offset frequency f_0 as the beat note from the f-$2f$ interferometer. Having an octave-spanning spectrum and after careful alignment of the interferometer, the beat spectrum is measured in an electronic spectrum analyzer that receives the modulated output current from the avalanche photodetector (APD).

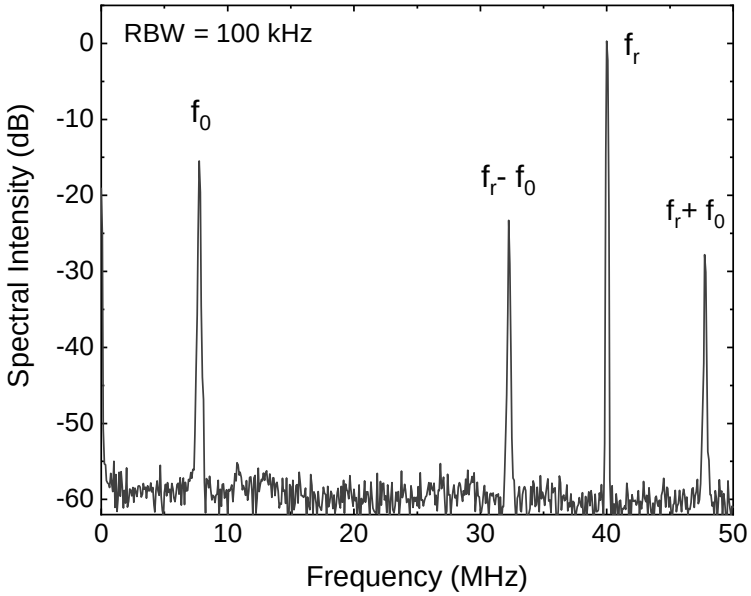

Fig. 5.10. Beat spectrum from f-2f interferometer. The spectrum shows the carrier-envelope offset frequency f_0 and the repetition rate f_r, the two degrees of freedom of the frequency comb. The beat between these two frequencies also appears as lines at $f_r - f_0$ and $f_r + f_0$. The peak widths are limited by the resolution bandwidth (RBW), 100 kHz. Measurement averaged over 10 scans.

Fig. 5.10 shows the measured beat spectrum with a resolution bandwidth (RBW) of 100 kHz, in a range from 0 MHz to 50 MHz, which is enough for displaying the carrier-envelope offset frequency f_0, the repetition rate f_r and their relative beat $f_r \pm f_0$. This pattern is periodically repeated for higher frequencies, as expected from Eq. 5.10. The offset frequency f_0 can take any value between 0 and 40MHz, which is the value of f_r, and in fact it can freely drift in time. It should be noted that identification of f_0 and $f_r - f_0$ is arbitrary, since it is not possible to tell them apart. Still, the identity of f_r and f_0 can be confirmed by blocking the light from one of the arms of the interferometer, making f_0 disappear but not f_r.

The offset frequency f_0 is therefore measured with a signal-to-noise ratio (S/N) of roughly 40 dB at 100 kHz RBW[10]. There are four contributions to the background and noise in the spectrum: the detector's (APD) and spectrum analyzer's (SA) instrumental noise, noise on the measurement of the light's amplitude and phase, and lastly the light's shot-noise, even though these last two are hardly distinguishable. This means, there are contributions to the noise from the instruments themselves that are there even when there is no light input, and additional contributions generated when measuring light. At least the contribution from each of the instruments

[10]The RBW is specified because the noise floor level depends on its value, i.e. it is higher for a higher RBW value, thus affecting the S/N ratio.

and the light itself can be easily tested by some simple measurements. One can measure the noise spectrum from the SA when it is not receiving any input from the APD, and then again when the APD is connected but the light input is completely blocked. These measurements can be compared to that of the beat spectrum, as in Fig. 5.11, to realize the different contributions to the background. As one can see, the spectrum analyzer's instrumental noise is the major contribution to the background, with almost no addition from the APD.

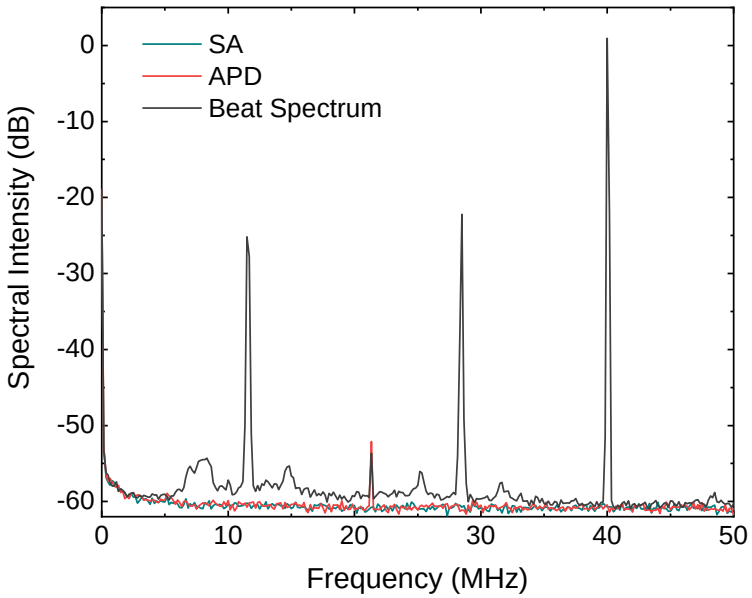

Fig. 5.11. Background levels in the beat spectrum The blue curve is the noise spectrum as measured from the SA without external input. The red curve is a similar measurement, with the APD connected to the SA but blocking the light input, i.e. the APD's instrumental noise on top of the SA's. The grey curve is the spectrum measured with light input, showing the beat spectrum. A spurious signal at 21 MHz is originated by some environmental signal that appears in the spectrum when a BNC cable is connected to the SA, acting as an antenna, connected or not to the APD (this signal does not appear in other measurements). Measurement averaged over 100 scans, with RBW= 100 kHz

Chapter 6

Comb stabilization

Stabilizing the comb, or phase-locking the mode-locked laser in other words, is a cornerstone in the full realisation of the frequency comb. Absolute control of the comb is achieved by locking its two degrees of freedom, the carrier-envelope offset frequency f_0 and the repetition rate f_r, or equivalently any other combination of two between f_0, f_r and one optical mode f_n. The choice of which two degrees of freedom are locked depends on the final application for the comb. For instance, if one locks f_0 and f_n[1], as it is our case, one can make sure that the optical mode used for spectroscopy has a phase noise that is only limited by the quality of the lock and the noise of reference laser to which the comb mode is locked. Alternatively, if f_0 and f_r are locked, the noise in f_r will be propagated and multiplied along the comb spectrum. Depending on the precision required in the experiment this may be something to consider.

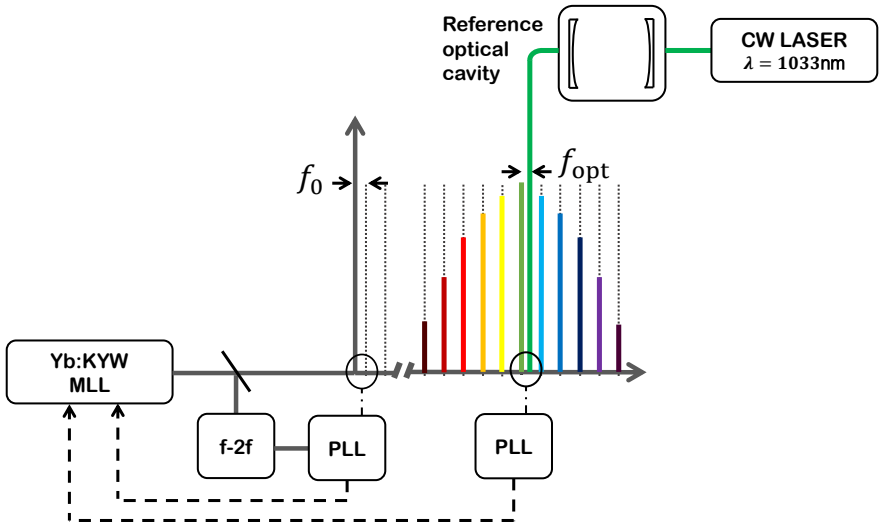

Fig. 6.1. Schematic diagram of the setup for the full stabilization of the Yb:KYW frequency comb. The beat of an optical mode with a CW laser at 1033 nm (f_{opt}), and the carrier-envelope offset frequency f_0 are locked by phase-locked loops (PLL), that send feedback to the cavity length and the optical power of the Yb:KYW MLL respectively.

Since the purpose of the Yb:KYW laser will ultimately be to perform spectroscopy on He^+, an optical mode from the oscillator's 10 mW main output is locked to a CW laser reference at 1033 nm. This was made before and independently from this work. As we have stated before, the main goal of this work is to fully lock the comb

[1]The specific mode number n may not be known, and may not be relevant.

by measuring an locking f_0 to an RF reference. A schematic of the complete setup is depicted in Fig. 6.1.

Throughout this chapter, we will explain some basic concepts about control theory and phase-locked loops, we will demonstrate how the offset frequency of the Yb:KYW laser f_0, measured by f-$2f$ interferometry, was experimentally locked; and we will show proof of the complete stabilization of the frequency comb.

6.1 Theoretical background

6.1.1 Control and feedback

Control theory is the field of engineering that deals with the control of dynamical systems. Control systems operate most of modern technologies, like cars or dishwashers, but they also regulate many natural processes. Think for instance about how your body regulates its temperature, keeping it close to a constant value. When our temperature sensors detect a drop in body temperature, our system burns calories and activate our muscles to shake and generate heat. On the other hand, when our temperature rises too much, we sweat and cool down by evaporating water. This intuitive example contains the main ideas behind control systems, that apply these ideas to mechanical or electronic systems.

One of the most important concepts in control theory is the notion of *feedback*. This refers to a situation in which two dynamical systems are strongly coupled, meaning they influence each other's dynamics in such a way that they must be described as a whole. Picture we have a system A that produces an output that is sent to another system B as an input. This affects the dynamics of B, and we can say that A controls B, but A knows nothing about B's output, and there is thus no feedback between them (open-loop control). However, if B's output is sent to A, affecting its dynamics and own input, we form a *feedback loop* (closed-loop control) in which each system is controlling the other's dynamics in a manner that a causality relation is not straightforwardly established and it is unclear who is controlling who.

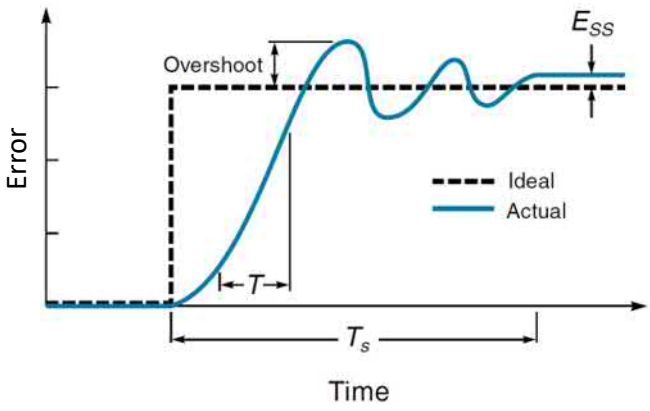

Fig. 6.2. Typical transient response showing common dynamics. Over-shooting, steady-state error (E_{SS}), rise time (T) and settling time (T_s) contribute to the departure of the transient response from the ideal case. Adapted from Killian's textbook [63].

This is the idea used by control systems to monitor the operation of a system, compare it with a desired performance and act on some of its physical properties to guide it towards the ideal behaviour.

We can understand this better, while introducing some jargon, with an example. A control system constantly measures the output of a *process* with a sensor, say an electrical current oscillating at a certain RF frequency. The measured quantity is referred to as the **process variable** (PV). A *comparator*, takes as input the sensor's signal and a given **set point** (SP), a target RF in this case, and produces an output known as the **error signal** e which is nothing more than the difference between the sensor's signal and the set point, $e = \mathrm{SP} - \mathrm{PV}$. The error signal is then sent to a *controller*, which has an implemented strategy for minimizing the error, thus driving the controlled variable to the set point. To do this, the controller sends a command to an *actuator*, that physically acts on the system, changing some property that affects the process variable.

The path the process variable follows from one point to another is called the *transient response*, and its typical features are shown in Fig. 6.2. In order to minimize the error signal in time, different control strategies may be used. The art in control theory is to find a strategy for each process that ensures stability while minimizing the time it takes for the process value to reach the set point, by avoiding **over-shooting** and a **steady-state error** as much as possible.

6.1.2 PID Control

The most common type of controller used in engineering systems is the **PID** controller. This controller applies a correction based on a linear combination of three types of feedback: Proportional + Integral + Derivative. Even though in some devices the use of Proportional + Integral feedback is enough, and we could be talking about PI controllers, PID is the general method and nomenclature.

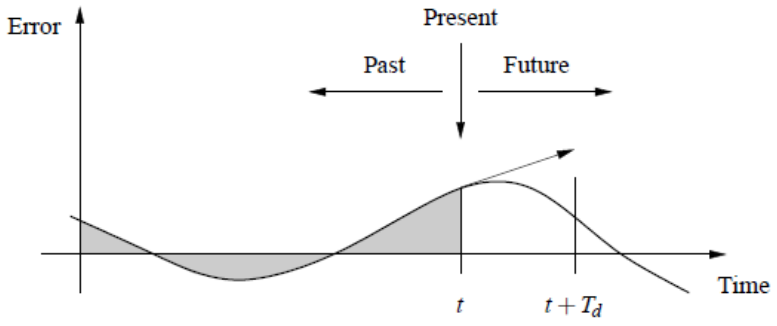

Fig. 6.3. Action of a PID control. The proportional term acts considering the instantaneous error at t, the integral term integrates over all past errors (shaded area) and the derivative term makes a projection to future errors based on the current trend. From Åström and Murray's book [64].

Proportional Control

In a purely proportional controller, the actuator applies a corrective action that is directly proportional to the error signal:

$$u_p(t) = K_p e(t) \ , \tag{6.1}$$

where u_p is the controller's output, K_p is the proportional gain, and $e(t) = \mathrm{SP}(t) - \mathrm{PV}(t)$ is the error signal at an instant t. This logic makes sense for quickly getting to the SP from distant PVs, while trying to avoid over-shooting by reducing the proportional-signal when these two values are close.

One problem of using proportional control only is its tendency to stabilize the system close to, but not exactly on the set point. This is known as the *steady-state error*. This happens because the controller output gets asymptotically close to zero when the process variable approaches the set point, but some opposition mechanism may prevent the system to ever reaching the set point, such as heat escaping an oven.

Integral Control

The introduction of integral control can eliminate the steady-state error. An integral controller has an output proportional to all past errors integrated in time

$$u_i(t) = K_i \int_{t_0}^{t} e(\tau)\mathrm{d}\tau \sim K_i \sum e\Delta t \ , \tag{6.2}$$

where K_i is the integral gain, and the sum is over all past errors e multiplied by some time interval Δt. If the error is constant in time, the integral term grows linearly and at some point it will overcome the aforementioned opposition mechanism. In other words, since the control has a notion of memory of past events, it is able to realize when the system is settling at a wrong steady state and prevent it, thus avoiding the steady-state error. As a counterpart, integral control reduces overall stability in the system, and can lead to a situation where the process value drifts away or oscillates around the set point with ever increasing oscillation amplitude, under certain conditions. This happens because the integral control can only "look back" in time and will only stop pushing the process value towards the set point when it has already passed it, leading to over-shooting. This is why an integral control is rarely used by itself, but is usually combined with a proportional control.

Derivative control

The over-shooting problem can solved by including a derivative term of the form

$$u_d(t) = K_d \frac{\mathrm{d}e(t)}{\mathrm{d}t} \sim K_d \frac{\Delta e}{\Delta t} \ , \tag{6.3}$$

being K_d the derivative gain. This type of control has some predictive ability, since it computes the slope or rate of change at the current position of the process value, such that $e(t + t') = e(t) + t' \ \mathrm{d}e(t)/\mathrm{d}t$. This way, it can slow down the rate at which the process value is approaching the set point with some anticipation and avoid over-shooting. Consequently, it reduces the settling time by helping the process value reach the set point, minimizing over-shooting, and also giving an initial boost when

the system goes from a steady-state to a new set point. But, the derivative control can also slow the system's response down when K_d is too high, and it can easily amplify any present noise. Considering this, and that PI controls can already achieve good stability under the right conditions, derivative control is not always used in control systems.

In conclusion, the complete action of a PID control can be summarized by the combined action of its three components: an integral term that makes decisions based on the past states of the system, a proportional term that acts according to the present error, and a derivative term that predicts the future states of the system based on its current trend, as depicted by Fig. 6.3. This is summarized by the PID equation [63, 64]:

$$u(t) = K_p e(t) + K_i \int_0^t e(\tau)\mathrm{d}\tau + K_d \frac{\mathrm{d}e(t)}{\mathrm{d}t} \,, \tag{6.4}$$

which also found in the literature as

$$u(t) = K_p \left(e(t) + \frac{1}{T_i} \int_{t_0}^t e(\tau)\mathrm{d}\tau + T_d \frac{\mathrm{d}e(t)}{\mathrm{d}t} \right) , \tag{6.5}$$

where we define the *integral time* $T_i = K_p/K_i$ and the *derivative time* $T_d = K_d/K_p$.

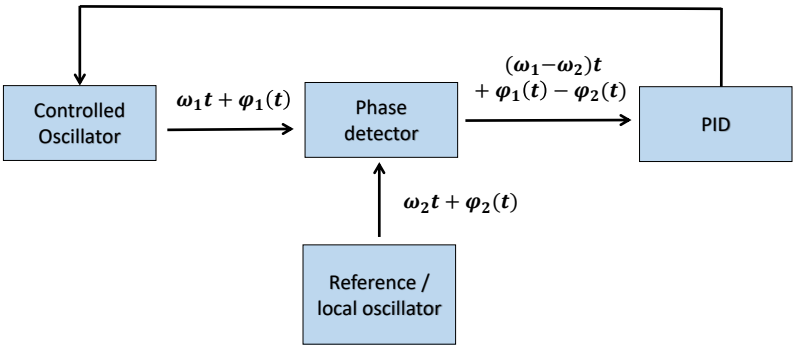

Fig. 6.4. Conceptualization of a phase-locked loop. A phase detector receives an input oscillatory signal and compares its phase to that of a reference oscillator. It generates a phase-error signal that is sent to a PID controller, that acts on the oscillator to keep a fixed phase relation between the signals, making both frequencies the same and correcting for any possible phase-jitter $\varphi(t)$.

6.1.3 Phase-locked loop

For our current application, which is locking and controlling f_0, we focus our attention on a specific kind of control systems, known as phase-locked loops (PLL). These systems keep a constant phase relation between an input wave signal and a reference oscillator. In order to do this, PLLs have a phase detector, that receives two input oscillatory signals and produces an oscillatory output with a phase proportional to their phase difference. If, for instance, these signals differ in frequency, the phase detector generates a signal that oscillates at the difference frequency. In PID

terms, the two inputs would be the process variable and the set point, and the output would be the error signal. This phase-error signal is usually filtered and amplified and then sent to a PID controller, which cancels out the error signal via an actuator that controls or affects the input frequency at its source, "locking" it to the reference oscillator's frequency. This is diagrammatically depicted in Fig. 6.4. Note that in a PLL, the phase detector creates an error signal dependent on the phase, but the PID controller is adjusting a frequency. This only means there is integration within the PLL, since phase is the time integral of frequency $\varphi(t) = \omega t + \varphi_0$.

6.2 Experimental setup

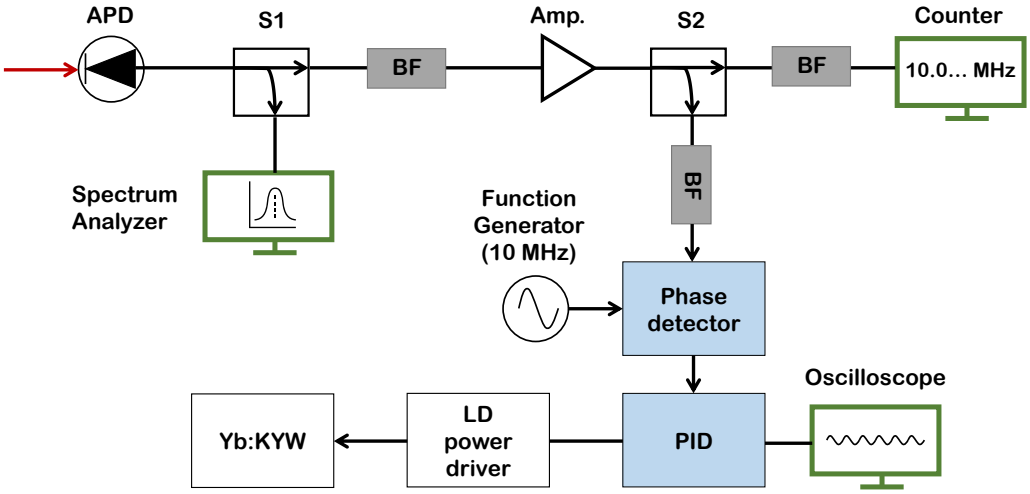

Fig. 6.5. Layout of the phase-locked loop setup for locking f_0. The beat spectrum is detected by the avalanche photodetector and displayed by the spectrum analyzer after being split (S1). The beat note is filtered through a band-pass filter at 10 MHz, amplified and split again (S2) between a frequency counter and the phase detector. The phase detector mixes the beat note with a 10 MHz reference signal from a function generator and produces the error signal that is sent to the PID controller and is also displayed on an oscilloscope. The PID controller minimizes the error signal by acting on the LD power drive that controls the optical pump power of the Yb:KYW oscillator, therefore locking f_0 to 10 MHz.

A phase-locked loop (PLL) is used for locking the carrier-envelope offset frequency f_0 to an RF reference. As explained in the previous section, a phase detector and a PID controller can be employed for locking f_0 to the set point established by an external reference, which is a sinusoidal signal with a frequency arbitrarily chosen to be 10 MHz. The control of f_0 is achieved by controlling the Yb:KYW's pump power, that affects f_0 as explained in Chapter 2.

Let us analyze the layout of our PLL setup with help from Fig. 6.5. From Chapter 5 we know the APD detects the beat spectrum. This signal is split (S1) so that we have a live visualization of the beat signal on the spectrum analyzer and can monitor the position and shape of the beatnote at all times. This permits, for instance, manually controlling the Yb:KYW's pump power to place f_0 close to 10 MHz to facilitate the locking process.

To separate and select the beatnote at 10 MHz from the full spectrum, a 10 MHz band-pass filter (BF) with 0.5 MHz bandwidth is used after the splitter. This signal is then amplified and split again (S2), and sent towards a counter and the phase detector. Additional band-pass filters are used at the input of both instruments to improve the beatnote S/N ratio, filtering out any noise that may have been amplified by the previous amplifier. The counter will measure the beat note frequency with high precision, and its working principle and related considerations will be explained later on.

The filtered beatnote signal from the S2 splitter in Fig. 6.5, is sent to the balanced mixer phase detector. The set point or reference signal is provided by a function generator that synthesizes a sinusoidal signal oscillating at 10 MHz. As explained in section 6.1.3, the phase detector mixes this reference signal with its main input, the offset frequency f_0, to produce a signal at the difference frequency, that plays the role of the error signal.

The error signal is then sent to a PID controller, which needs to be manually tuned to optimize its performance, overseen by monitoring the error signal in an oscilloscope. After tuning, it eventually locks the offset frequency f_0 to 10 MHz by acting on the LD power driver that controls the pump optical power of the Yb:KYW laser.

6.2.1 Counters, Function Generators and timebases

The frequency counter is a device that measures frequencies by counting the number of times an oscillating electronic signal crosses a voltage threshold (it may be a zero-crossing in a specific direction, e.g. from negative to positive) in a given time interval. In other words, it accumulates the number of cycles during a time interval, after which it calculates the oscillations per second. This time interval is known as the *gate time* and it determines the resolution of the counter. According to this, a gate time of 1 s would allow for a resolution of 1 Hz. Although, as a matter of fact, modern counters not only count the cycles in the gate time, but also the relative time of arrival of the first and last pulses in that interval. This makes it possible to improve the resolution. The signal that triggers the gating is usually given by a local oscillator, which is typically a temperature controlled crystal oscillator, like that in a quartz clock. This internal clock sets the counter's *time-base*, and its precision limits the precision of the measured frequency. For some applications, a highly stable time-base may be wanted, and external references may be used to improve on the local oscillator's performance.

In this experiment, the counters and function generator's time-bases, i.e. elements that either measure or produce frequencies, are referenced to a hydrogen maser emitting a 10 MHz RF. This maser is hosted at the MPQ's Laser Spectroscopy Division and serves as a highly stable reference for many of the electronics in the different labs where high-precision experiments are carried out. The maser signal is propagated and split in frequency distributors which bring the signal to the desired devices, allowing for synchronization of their time-bases with each other and with the 10 MHz maser. Additional devices can also be synchronized by cascading them with the maser referenced oscillators.

6.2.2 The phase detector

The phase detector is usually an electronic circuit that has the ability to produce a periodic output at the difference frequency between two input frequencies. In

phase-locked loops, we can classify phase detectors in two types. Type I or analog detectors can act on analog or digital signals, by simply multiplying both inputs as a *frequency mixer*[2]. In digital systems this operation is performed by an XOR gate, while for analog signals, the phase detector is an analog multiplier also called a balanced mixer, whose output is an analog waveform. On the contrary, Type II or digital detectors produce a digital output sensitive to the relative timing between the edges of the input signals. They each have their own advantages, but for the present PLL a Type II detector was used.

6.2.3 PID tuning

The PID controller is manufactured by the group's electronic workshop and is in fact a PI controller with only proportional and integral gains. Both gains must be manually adjusted by rotating their corresponding knobs to find the parameters that achieve the best performance when closing the loop. This process is commonly known as "tuning" the PID. To monitor the PID's action, the error signal is sampled and displayed by an oscilloscope, so that one can see whether it is overshooting, drifting or stable, and also how clean or noisy it is. The tuning proceeds as follows. Both gains are set to zero, and f_0 is set close to 10 MHz by manually adjusting the pump power of the Yb:KYW laser. Then, closing the loop, the proportional gain can be gradually increased. The error signal may initially not change or change very slowly, but when the P-gain is increased it will at some point flatten the error signal, meaning there is a constant phase relationship between the reference and the input waves, and they have thus the same frequency. At this point, f_0 is already locked. The integral gain is then increased to make sure there is no steady-state error, but avoiding an oscillatory behaviour of the error signal, which means it is overshooting and losing stability. When the PID is optimized and the error signal is flat and steady, we can claim the loop to be stable and the system phase-locked. Both gains can also be fine tuned by reducing the noise on the beat note, which is related to its width around 10 MHz and can be checked in the spectrum analyzer with the appropriate scale and RBW.

One must also consider one important aspect of locking f_0. As we discussed in Chapter 5, in the frequency interval between the origin and f_r there two beat notes, f_0 and $f_r - f_0$, and their individual identification is not possible a priori. This means we will be locking any of the two at 10 MHz, but this locks f_0 and the comb spectrum anyways, so it does not pose a problem. The only difference is they will have opposite behaviour when changing the laser's pump power, meaning one will move towards higher frequencies and the other ones towards lower frequencies when increasing the pump power and vice-versa. This means the PID controller should act in opposite ways with one frequency or the other if it is to successfully lock any of them. For this purpose, the sign of the loop can be easily inverted with a switch, so that one can just try what sign can lock the beat note at 10 MHz, and invert it manually.

[2]Note the similarity with an optical interferometer. In fact, the term "heterodyning" originally refers to mixing or multiplying two frequencies in electronic systems, to obtain their sum and difference frequencies.

6.3 Results

6.3.1 Control of f_0

As we have explained before, the complete stabilization of the comb spectrum is achieved by locking the beat between a comb mode and a CW laser at 1033 nm, which will be called f_{opt}, and the f-2f beat, i.e. the carrier-envelope offset frequency f_0.

Locking the optical beat f_{opt} is achieved by controlling the cavity length with a piezoelectric transducer that changes the position of one of the cavity mirrors when a voltage is applied to it, making use of a similar PLL scheme as the one used for locking f_0, but built independently from this work. The stabilization of f_0 is achieved by actuating on the LD's optical pump power of the Yb:KYW oscillator, regulated by a power driver which is controlled by the PID loop described in the previous section.

We can easily see the action of the pump power on f_0 by measuring the beat note frequency with the spectrum analyzer while changing the pump current manually on the LD power driver, with its PLL open so that f_0 is not locked to a specific value. It can be seen in Fig. 6.6 (a) how f_0 changes linearly with the pump current, and thus optical power. This is always the desired behaviour between an actuator and its controlled variable for a good control. Once again it must be noted that whether the beat frequency increases or decreases just depends on which beat note is being locked, so the sign of the slope seen in Fig. 6.6 (a) may change. The optical pump power proves to be a good actuator in terms of range, since f_0 can be shifted by a few MHz by only changing the pump current in the mA scale, and by doing a simple least-squares linear fitting we see that the shifting rate is (-)320 $\pm$ 5 kHz/mA.

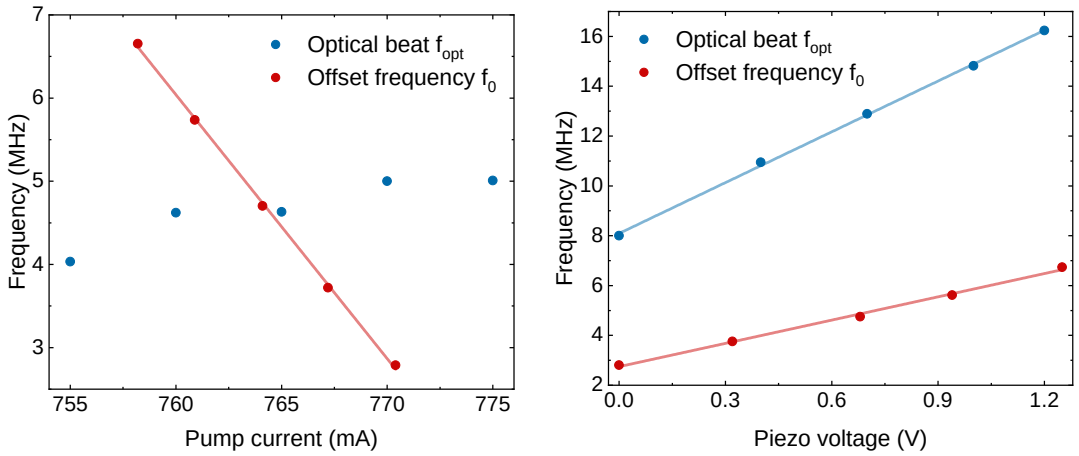

Fig. 6.6. (a) Carrier-envelope offset frequency as a function of the Yb:KYW pump current. The data points are measured from the position of the beat note on the spectrum analyzer, and the line is a least-squares linear fit with a slope of -320 $\pm$ 5 kHz/mA. f_0 follows a clear linear behaviour with the optical pump power over a range wide enough for optimal locking. **(b) Optical beat (blue) and CEO frequency (red) as a function of the voltage applied to the piezoelectric mirror controlling the Yb:KYW laser's cavity length**. The motion of the mirror affects the optical beat linearly as one would expect by changing the cavity length, but it also affects f_0 due to a slight misalignment it introduces, changing the non-linear index of refraction via the Kerr effect. The lines are linear fits of the data points with corresponding slopes of 6.8 $\pm$ 0.1 MHz/mA for f_{opt} and 3.1 $\pm$ 0.1 MHz/mA for f_0.

This should provide good long term stability, when f_0 could drift from 0 to 40 MHz if not controlled.

The ability to control f_0 in the short term depends more on the reaction speed or modulation bandwidth of the actuator to compensate for small scale but fast fluctuations. This will be further discussed later on, but regarding the long term stability we may wonder what is the effective range the LD power driver can tolerate, and as a matter of fact the limitation comes from the lasing modes of the Yb:KYW oscillator. When the optical pump power is driven below 0.5-0.6 A pump power, the oscillator will stop mode-locking, therefore losing the pulsed and comb structure. On the maximum boundary, when the pump power is too high, say above 1.8 A, the Yb:KYW starts lasing in a CW mode on top of the pulsed emission, which is an unwanted behaviour since it interacts with the comb structure adding extra RF beat notes that may confuse the locking system, apart from the consequences it may have when performing spectroscopy.

When locking simultaneously f_0 and f_{opt} we ideally want to control physical parameters of the optical oscillator that act independently on these two frequencies, i.e. we want both degrees of freedom to be uncoupled. This is in principle the case when acting on the optical pump power to control f_0 and the cavity length to control f_{opt}. Nonetheless, the observed behaviour is that changing the pump power does indeed only affect f_0, leaving f_{opt} unchanged [3], but applying some voltage to the piezoelectric transducer to change the cavity length affects both frequencies together. This can clearly be seen in Fig. 6.6 (b), were both frequencies were measured for different voltages applied to the piezoelectric mounted mirror. The optical beat f_{opt} changes 6.8 ± 0.1 MHz/V and the carrier-envelope offset frequency f_0 changes by 3.1 ± 0.1 MHz/V. This unexpected behaviour can be understood noticing the motion of the piezoelectric mirror is not exactly along a straight axis, but rather forms an arc with a slight curvature due to an imperfect design. This provokes not only a change in the geometric cavity length but also a slight misalignment of the light beam inside the cavity, that changes the Kerr-lens self-focusing condition in the Yb:KYW crystal. This changes the non-linear contribution to the index of refraction which in turn changes the dispersion in the cavity, and thus f_0. In conclusion, the motion of this specific mirror couples f_0 and f_{opt}.

This is not ideal but it does not impede simultaneously locking both frequencies, because the rate of change of the optical beat with the piezo voltage is still twice that of f_0, and f_0 has a broad range of action when controlled by the LD pump current, that can compensate for the deviations inflicted by the motion of the piezoelectric mirror. Still, it may impose a limit on the long term stability since, even though both locking systems may find a temporary balance, they are somehow coupled into a combined feedback loop that may eventually drive one of the actuators out of its effective working range, for instance lowering the optical pump power to a level where the laser stops mode-locking.

6.3.2 Stability of the frequency comb

By closing both the feedback loops controlling f_0 and f_{opt} we completely stabilize the frequency comb. This means that locking the offset frequency and one of the optical modes leaves the comb no degrees of freedom, therefore fixing also the repetition rate f_r. These three frequencies are measured by counters that sample the

[3] This is in fact not intuitive at all, but can be understood from the *fixed point model* [56].

frequencies with a 1 s gate time and send the data to a computer that uploads each data point with its timestamp to an online database hosted in a local server. This permits monitoring the three frequencies at all times and recording any event that may alter the stability of the comb and track how long the feedback loops can keep the comb stabilized. As we have just explained, the long term stability is limited by some factors like the coupling of f_0 and f_{opt} through the piezoelectric mirror, but still the regular practice showed that the comb can be stabilized commonly for about 30 minutes straight, and Fig. 6.7 shows an example of it. As we know, the CEO frequency is locked to a 10 MHz reference, and the optical beat is locked at 13 Mhz. The repetition rate is not locked at a specific value since it depends on the two aforementioned parameters, but is also fixed when the frequency comb is stabilized. In fact, for different measurements, the repetition rate is generally fixed at different values. This happens because when locking an optical beat note to the 13 MHz reference with respect to the CW laser, we do not choose or know the specific comb line that is being locked[4]. This means locking comb lines with different mode number will fix $f_r = (f_n - f_0)/n$ at different values.

Apart from fast noise fluctuations, the three frequencies are kept constant at their aim values for over 30 min. Note that the noise around the average value cannot be taken directly as a measure of the frequency oscillations since it depends on instrumental parameters such as the gate time, but it still shows the frequencies are kept constant within the 10-100 mHz scale. After the approximate 30 min time, either f_0 or f_{opt} would usually get unlocked and its corresponding PLL fail to lock it back, which is understandable since the pass-band filters limit the transmitted signal to narrow values around the reference frequencies. This 30 min stability time should be improved for performing spectroscopy experiments with f_0 stabilized, but it is a first step in the right direction.

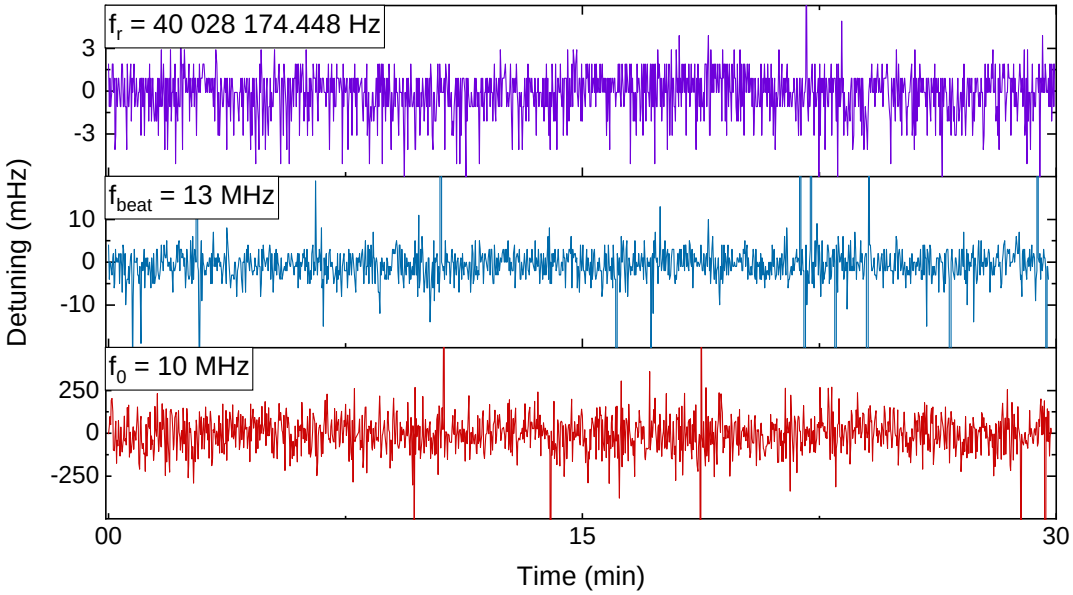

Fig. 6.7. Simultaneous measurement of the repetition rate f_r, optical beat f_{opt} and CEO frequency f_0 as a function of time, with the latter two locked by PLLs. The data are measured by frequency counters and depicted as detuning from the framed values. Measurement over 30 min shows good long term stability.

[4]Even though it could be found out.

The stability of f_0 in the short scale is a different matter. Any deviation of f_0 from a delta function can be attributed to the performance of the feedback loop. The shape and width of the beat note can be checked with a spectrum analyzer, as in Fig. 6.8. If the width of the corresponding peak is limited by the instrument's RBW, we can at least know its proper width is lower than that limit, and argue it can be a delta function, but if the RBW is lowered to such a value that the peak's width does not decrease any more, one can extract information about the phase-noise fluctuations of the measured frequency.

Phase-noise theory is a broad and complex field and we will not go into details in this work, but some references are left for the interested reader [65, 66]. Very briefly, phase-noise manifests as side-bands (e.g. with Lorentzian shape) on the carrier frequency. When the distinction between the delta function and its side-bands is clear, a measurement of the power spectral density (PSD) can be made to extract the standard deviation of the frequency fluctuations. However, when the phase-noise is too large, the distinction between carrier and sidebands is unclear and this analysis is practically unfeasible. This is our case (see Fig. 6.8), which indicates that the actuator is not fast enough to follow and compensate for the short-scale frequency fluctuations. One option to reduce the phase-noise in f_0 would be to use a modified LD power driver with a faster action on the optical pump power, or even replacing the laser diode by a more stable solid state laser that would reduce the amplitude noise of the pump. In any case, the limited time in which this work was performed did not allow for implementation of these ideas.

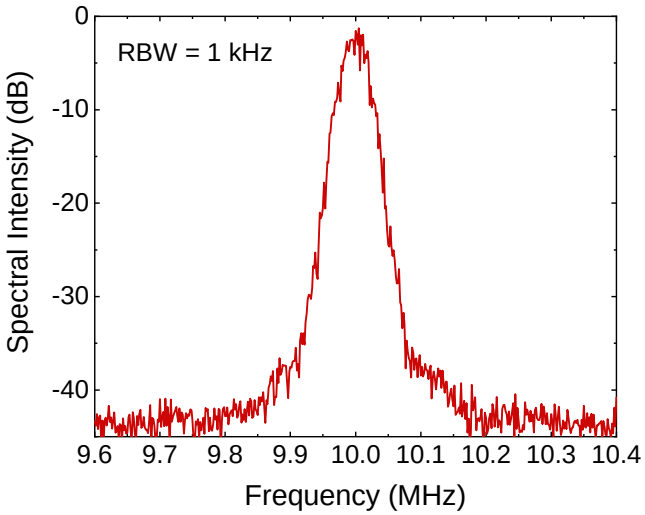

Fig. 6.8. Spectrum measured around the locked CEO frequency f_0. The spectrum was measured with a spectrum analyzer with RBW= 1 kHz. Its finite width, and the inability to distinguish the carrier from the noise side-bands evidences that the performance of the actuator in the short time-scale can be improved.

All in all, the degrees of freedom of the frequency comb were successfully locked and stabilized, which grants a full control over the comb. With a potential application in spectroscopy in mind, the long term stability may have to be further developed, and even though the short-scale stability of f_0 can be improved and there are already some ideas to do so, its fluctuations do not directly translate to phase-noise in f_{opt}, at least not in the same magnitude. How much the noise in f_0 affects f_{opt} will eventually depend on the quality of the lock on f_{opt}.

Chapter 7

Conclusions and Outlook

In this work, we report the phase stabilization of the carrier-envelope offset (CEO) frequency of an Yb:KYW femtosecond frequency comb. The output from the Yb:KYW optical oscillator was amplified, compressed and spectrally broadened to an octave of frequencies in a photonic crystal fiber. This octave spanning spectrum was used to measure the comb's CEO frequency in an f-2f interferometer, which was then stabilized by sending feedback to the laser pump current. This scheme, together with an independent setup that locks an optical comb mode to a CW laser, allows for fully stabilizing the Yb:KYW frequency comb.

First, numerical simulations were made for a better understanding of the pulse propagation dynamics that are most relevant for this experiment. The split-step Fourier method was implemented for this goal, and successfully reproduced the systematic effects of GVD, TOD and SPM and their combined effect. Simulations with realistic parameters from our experimental setup were also performed, showing the ability to achieve octave-spanning. The simulations can still be improved by introducing higher-order nonlinear effects that would potentially reproduce finer details of the calculated spectra and pulse shapes.

An Yb-doped fiber amplifier and pulse compressor were built for achieving enough peak intensity for octave-spanning in the photonic crystal fiber. The fiber amplifier can easily achieve average output powers of 300 - 500 mW (5 - 8 net gain) for supply currents of 2.5 - 3 A, well below the maximum available power for the laser diode that serves as optical pump. The pulse compressor's performance was tested with a FROG system, which showed a compression of the pulses down to 65 fs (FWHM), improving on their original 100 fs duration.

Octave spanning was achieved in a 16 cm long, 3.3 μm core-sized photonic crystal fiber seeded with 65 fs pulses at a repetition rate of 40 MHz, with an average optical power of 75 mW coupled into the fiber. This specific set of parameters was carefully selected for optimum performance, so that the broadened spectrum's side-lobes fall on the f and 2f frequencies, maximizing their intensity for better f-2f interferometry.

An f-2f interferometer was built and used to measure the CEO frequency f_0 with a 40 dB signal-to-noise ratio at 100 kHz resolution bandwidth.

The CEO frequency was stabilized by a phase-locked loop acting on the Yb:KYW laser's optical pump power. Together with an optical mode being phase-locked to a CW laser via the Yb:KYW laser's cavity length, the frequency comb can be fully stabilized for about 30 min. This stability time should be improved in the future if the device is to be used in spectroscopy experiments, and also the short-scale stability of

f_0 has some room for improvement, since low RBW spectra show a widened peak at f_0 that denotes excessive phase-noise. Possible upgrades on the setup to solve these issues could consist on increasing the bandwidth of the pump power modulation and substituting the laser diode pump by a solid state laser with lower intensity noise.

All in all, the success of this f-2f interferometer sets a milestone in the stabilization of the Yb:KYW frequency comb and its possible use in high precision spectroscopy experiments, such as the exploration of the 1S-2S transition in He^+.

Bibliography

[1] A. Beyer, L. Maisenbacher, K. Khabarova, A. Matveev, R. Pohl, T. Udem, T. W. Hänsch, and N. Kolachevsky, "Precision spectroscopy of 2S– n P transitions in atomic hydrogen for a new determination of the Rydberg constant and the proton charge radius", en, Physica Scripta **T165**, 014030 (2015).

[2] A. Grinin, A. Matveev, D. C. Yost, L. Maisenbacher, V. Wirthl, R. Pohl, T. W. Hänsch, and T. Udem, "Two-photon frequency comb spectroscopy of atomic hydrogen", en, Science **370**, Publisher: American Association for the Advancement of Science Section: Research Article, 1061–1066 (2020).

[3] R. Pohl, F. Nez, L. M. P. Fernandes, F. D. Amaro, F. Biraben, J. M. R. Cardoso, D. S. Covita, A. Dax, S. Dhawan, M. Diepold, A. Giesen, A. L. Gouvea, T. Graf, T. W. Hänsch, P. Indelicato, L. Julien, P. Knowles, F. Kottmann, E.-O. Le Bigot, Y.-W. Liu, J. A. M. Lopes, L. Ludhova, C. M. B. Monteiro, F. Mulhauser, T. Nebel, P. Rabinowitz, J. M. F. dos Santos, L. A. Schaller, K. Schuhmann, C. Schwob, D. Taqqu, J. F. C. A. Veloso, A. Antognini, and CREMA Collaboration, "Laser spectroscopy of muonic deuterium", eng, Science (New York, N.Y.) **353**, 669–673 (2016).

[4] A. Beyer, L. Maisenbacher, A. Matveev, R. Pohl, K. Khabarova, A. Grinin, T. Lamour, D. C. Yost, T. W. Hänsch, N. Kolachevsky, and T. Udem, "The Rydberg constant and proton size from atomic hydrogen", en, Science **358**, Publisher: American Association for the Advancement of Science Section: Research Article, 79–85 (2017).

[5] R. Pohl, R. Gilman, G. A. Miller, and K. Pachucki, "Muonic Hydrogen and the Proton Radius Puzzle", en, Annual Review of Nuclear and Particle Science **63**, 175–204 (2013).

[6] T. Udem, "Quantum electrodynamics and the proton size", en, Nature Physics **14**, Number: 6 Publisher: Nature Publishing Group, 632–632 (2018).

[7] R. Pohl, A. Antognini, F. Nez, F. D. Amaro, F. Biraben, J. M. R. Cardoso, D. S. Covita, A. Dax, S. Dhawan, L. M. P. Fernandes, A. Giesen, T. Graf, T. W. Hänsch, P. Indelicato, L. Julien, C.-Y. Kao, P. Knowles, E.-O. Le Bigot, Y.-W. Liu, J. A. M. Lopes, L. Ludhova, C. M. B. Monteiro, F. Mulhauser, T. Nebel, P. Rabinowitz, J. M. F. dos Santos, L. A. Schaller, K. Schuhmann, C. Schwob, D. Taqqu, J. F. C. A. Veloso, and F. Kottmann, "The size of the proton", en, Nature **466**, 213–216 (2010).

[8] M. Herrmann, M. Haas, U. D. Jentschura, F. Kottmann, D. Leibfried, G. Saathoff, C. Gohle, A. Ozawa, V. Batteiger, S. Knünz, N. Kolachevsky, H. A. Schüssler, T. W. Hänsch, and T. Udem, "Feasibility of coherent xuv spectroscopy on the 1 S 2 S transition in singly ionized helium", en, Physical Review A **79**, 052505 (2009).

[9] A. Ozawa, J. Rauschenberger, C. Gohle, M. Herrmann, D. R. Walker, V. Pervak, A. Fernandez, R. Graf, A. Apolonski, R. Holzwarth, F. Krausz, T. W. Hänsch, and T. Udem, "High Harmonic Frequency Combs for High Resolution Spectroscopy", Physical Review Letters **100**, Publisher: American Physical Society, 253901 (2008).

[10] D. C. Yost, T. R. Schibli, and J. Ye, "Efficient output coupling of intracavity high-harmonic generation", EN, Optics Letters **33**, Publisher: Optical Society of America, 1099–1101 (2008).

[11]C. Gohle, T. Udem, M. Herrmann, J. Rauschenberger, R. Holzwarth, H. A. Schuessler, F. Krausz, and T. W. Hänsch, "A frequency comb in the extreme ultraviolet", en, Nature **436**, 234–237 (2005).
[12]R. J. Jones, K. D. Moll, M. J. Thorpe, and J. Ye, "Phase-Coherent Frequency Combs in the Vacuum Ultraviolet via High-Harmonic Generation inside a Femtosecond Enhancement Cavity", Physical Review Letters **94**, Publisher: American Physical Society, 193201 (2005).
[13]S. A. Diddams, K. Vahala, and T. Udem, "Optical frequency combs: Coherently uniting the electromagnetic spectrum", en, 14 (2020).
[14]J. N. Eckstein, "High resolution spectroscopy using multiple coherent interactions", Journal Abbreviation: Ph.D. Thesis Publication Title: Ph.D. Thesis, PhD thesis (1978).
[15]A. I. Ferguson, J. N. Eckstein, and T. W. Hänsch, "Polarization spectroscopy with ultrashort light pulses", en, Applied physics **18**, 257–260 (1979).
[16]T. Udem, R Holzwarth, and T. W. Hänsch, "Optical frequency metrology", en, **416**, 5 (2002).
[17]L. E. Hargrove, R. L. Fork, and M. A. Pollack, "LOCKING OF He–Ne LASER MODES INDUCED BY SYNCHRONOUS INTRACAVITY MODULATION", Applied Physics Letters **5**, Publisher: American Institute of Physics, 4–5 (1964).
[18]H. Telle, G. Steinmeyer, A. Dunlop, J. Stenger, D. Sutter, and U. Keller, "Carrier-envelope offset phase control: A novel concept for absolute optical frequency measurement and ultrashort pulse generation", en, Applied Physics B **69**, 327–332 (1999).
[19]J. Reichert, R. Holzwarth, T. Udem, and T. W. Hänsch, "Measuring the frequency of light with mode-locked lasers", en, Optics Communications **172**, 59–68 (1999).
[20]J. K. Ranka, R. S. Windeler, and A. J. Stentz, "Visible continuum generation in air–silica microstructure optical fibers with anomalous dispersion at 800 nm", EN, Optics Letters **25**, Publisher: Optical Society of America, 25–27 (2000).
[21]K. Evenson, J. Wells, F. Petersen, B. Danielson, and G. Day, "Accurate frequencies of molecular transitions used in laser stabilization: the 3.39-m transition in CH4 and the 9.33- and 10.18-m transitions in CO2", Applied Physics Letters **22**, Publisher: American Institute of Physics, 192–195 (1973).
[22]V. P. Chebotayev, V. G. Goldort, V. M. Klementyev, M. V. Nikitin, B. A. Timchenko, and V. F. Zakharyash, "Development of an optical time scale", en, Applied Physics B **29**, 63–65 (1982).
[23]L. Hollberg, S. Diddams, A. Bartels, T. Fortier, and K. Kim, "The measurement of optical frequencies", English, Metrologia **42**, Publisher: IOP Publishing Ltd., S105–S124 (2005).
[24]H. Schnatz, B. Lipphardt, J. Helmcke, F. Riehle, and G. Zinner, "First Phase-Coherent Frequency Measurement of Visible Radiation", Physical Review Letters **76**, Publisher: American Physical Society, 18–21 (1996).
[25]T. W. Hänsch, "Nobel Lecture: Passion for precision", en, Reviews of Modern Physics **78**, 1297–1309 (2006).
[26]J. L. Hall, "Nobel Lecture: Defining and measuring optical frequencies", en, Reviews of Modern Physics **78**, 1279–1295 (2006).
[27]S. A. Diddams, T. Udem, J. C. Bergquist, E. A. Curtis, R. E. Drullinger, L. Hollberg, W. M. Itano, W. D. Lee, C. W. Oates, K. R. Vogel, and D. J. Wineland, "An Optical Clock Based on a Single Trapped 199Hg+ Ion", en, Science **293**, Publisher: American Association for the Advancement of Science Section: Research Article, 825–828 (2001).
[28]C. Lisdat, G. Grosche, N. Quintin, C. Shi, S. M. F. Raupach, C. Grebing, D. Nicolodi, F. Stefani, A. Al-Masoudi, S. Dörscher, S. Häfner, J.-L. Robyr, N. Chiodo, S. Bilicki,

E. Bookjans, A. Koczwara, S. Koke, A. Kuhl, F. Wiotte, F. Meynadier, E. Camisard, M. Abgrall, M. Lours, T. Legero, H. Schnatz, U. Sterr, H. Denker, C. Chardonnet, Y. Le Coq, G. Santarelli, A. Amy-Klein, R. Le Targat, J. Lodewyck, O. Lopez, and P.-E. Pottie, "A clock network for geodesy and fundamental science", en, Nature Communications **7**, Number: 1 Publisher: Nature Publishing Group, 12443 (2016).

[29]K. Predehl, G. Grosche, S. M. F. Raupach, S. Droste, O. Terra, J. Alnis, T. Legero, T. W. Hänsch, T. Udem, R. Holzwarth, and H. Schnatz, "A 920-Kilometer Optical Fiber Link for Frequency Metrology at the 19th Decimal Place", en, Science **336**, Publisher: American Association for the Advancement of Science Section: Report, 441–444 (2012).

[30]J. Guéna, S. Weyers, M. Abgrall, C. Grebing, V. Gerginov, P. Rosenbusch, S. Bize, B. Lipphardt, H. Denker, N. Quintin, S. M. F. Raupach, D. Nicolodi, F. Stefani, N. Chiodo, S. Koke, A. Kuhl, F. Wiotte, F. Meynadier, E. Camisard, C. Chardonnet, Y. L. Coq, M. Lours, G. Santarelli, A. Amy-Klein, R. L. Targat, O. Lopez, P. E. Pottie, and G. Grosche, "First international comparison of fountain primary frequency standards via a long distance optical fiber link", en, Metrologia **54**, Publisher: IOP Publishing, 348–354 (2017).

[31]T. Fortier and E. Baumann, "20 years of developments in optical frequency comb technology and applications", en, Communications Physics **2**, 153 (2019).

[32]S. Diddams, A. Bartels, T. Ramond, C. Oates, S. Bize, A. Curtis, J. Bergquist, and L. Hollberg, "Design and Control of Femtosecond Lasers for Optical Clocks and the Synthesis of Low-Noise Optical and Microwave Signals", Selected Topics in Quantum Electronics, IEEE Journal of **9**, 1072–1080 (2003).

[33]S. Bize, S. A. Diddams, U. Tanaka, C. E. Tanner, W. H. Oskay, R. E. Drullinger, T. E. Parker, T. P. Heavner, S. R. Jefferts, L. Hollberg, W. M. Itano, and J. C. Bergquist, "Testing the stability of fundamental constants with the 199Hg+ single-ion optical clock", eng, Physical Review Letters **90**, 150802 (2003).

[34]T. Rosenband, D. B. Hume, P. O. Schmidt, C. W. Chou, A. Brusch, L. Lorini, W. H. Oskay, R. E. Drullinger, T. M. Fortier, J. E. Stalnaker, S. A. Diddams, W. C. Swann, N. R. Newbury, W. M. Itano, D. J. Wineland, and J. C. Bergquist, "Frequency Ratio of Al+ and Hg+ Single-Ion Optical Clocks; Metrology at the 17th Decimal Place", en, Science **319**, Publisher: American Association for the Advancement of Science Section: Report, 1808–1812 (2008).

[35]M. Fischer, N. Kolachevsky, M. Zimmermann, R. Holzwarth, T. Udem, T. W. Hänsch, M. Abgrall, J. Grünert, I. Maksimovic, S. Bize, H. Marion, F. P. D. Santos, P. Lemonde, G. Santarelli, P. Laurent, A. Clairon, C. Salomon, M. Haas, U. D. Jentschura, and C. H. Keitel, "New Limits on the Drift of Fundamental Constants from Laboratory Measurements", Physical Review Letters **92**, Publisher: American Physical Society, 230802 (2004).

[36]T. M. Fortier, N. Ashby, J. C. Bergquist, M. J. Delaney, S. A. Diddams, T. P. Heavner, L. Hollberg, W. M. Itano, S. R. Jefferts, K. Kim, F. Levi, L. Lorini, W. H. Oskay, T. E. Parker, J. Shirley, and J. E. Stalnaker, "Precision Atomic Spectroscopy for Improved Limits on Variation of the Fine Structure Constant and Local Position Invariance", Physical Review Letters **98**, Publisher: American Physical Society, 070801 (2007).

[37]P. Wcisło, P. Ablewski, K. Beloy, S. Bilicki, M. Bober, R. Brown, R. Fasano, R. Ciuryło, H. Hachisu, T. Ido, J. Lodewyck, A. Ludlow, W. McGrew, P. Morzyński, D. Nicolodi, M. Schioppo, M. Sekido, R. L. Targat, P. Wolf, X. Zhang, B. Zjawin, and M. Zawada, "New bounds on dark matter coupling from a global network of optical atomic clocks", en, Science Advances **4**, Publisher: American Association for the Advancement of Science Section: Research Article, eaau4869 (2018).

[38] A. Hees, J. Guéna, M. Abgrall, S. Bize, and P. Wolf, "Searching for an Oscillating Massive Scalar Field as a Dark Matter Candidate Using Atomic Hyperfine Frequency Comparisons", Physical Review Letters **117**, Publisher: American Physical Society, 061301 (2016).

[39] U. Keller, "Recent developments in compact ultrafast lasers", en, Nature **424**, Number: 6950 Publisher: Nature Publishing Group, 831–838 (2003).

[40] T. Steinmetz, T. Wilken, C. Araujo-Hauck, R. Holzwarth, T. W. Hänsch, L. Pasquini, A. Manescau, S. D'Odorico, M. T. Murphy, T. Kentischer, W. Schmidt, and T. Udem, "Laser Frequency Combs for Astronomical Observations", en, Science **321**, Publisher: American Association for the Advancement of Science Section: Report, 1335–1337 (2008).

[41] A. J. Metcalf, T. Anderson, C. F. Bender, S. Blakeslee, W. Brand, D. R. Carlson, W. D. Cochran, S. A. Diddams, M. Endl, C. Fredrick, S. Halverson, D. D. Hickstein, F. Hearty, J. Jennings, S. Kanodia, K. F. Kaplan, E. Levi, E. Lubar, S. Mahadevan, A. Monson, J. P. Ninan, C. Nitroy, S. Osterman, S. B. Papp, F. Quinlan, L. Ramsey, P. Robertson, A. Roy, C. Schwab, S. Sigurdsson, K. Srinivasan, G. Stefansson, D. A. Sterner, R. Terrien, A. Wolszczan, J. T. Wright, and G. Ycas, "Stellar spectroscopy in the near-infrared with a laser frequency comb", EN, Optica **6**, Publisher: Optical Society of America, 233–239 (2019).

[42] R. A. Probst, D. Milaković, B. Toledo-Padrón, G. Lo Curto, G. Avila, A. Brucalassi, B. L. Canto Martins, I. de Castro Leão, M. Esposito, J. I. González Hernández, F. Grupp, T. W. Hänsch, H. Kellermann, F. Kerber, O. Mandel, A. Manescau, E. Pozna, R. Rebolo, J. R. de Medeiros, T. Steinmetz, A. Suárez Mascareño, T. Udem, J. Urrutia, Y. Wu, L. Pasquini, and R. Holzwarth, "A crucial test for astronomical spectrograph calibration with frequency combs", en, Nature Astronomy **4**, Number: 6 Publisher: Nature Publishing Group, 603–608 (2020).

[43] M.-G. Suh and K. J. Vahala, "Soliton microcomb range measurement", en, Science **359**, Publisher: American Association for the Advancement of Science Section: Report, 884–887 (2018).

[44] P. Trocha, M. Karpov, D. Ganin, M. H. P. Pfeiffer, A. Kordts, S. Wolf, J. Krockenberger, P. Marin-Palomo, C. Weimann, S. Randel, W. Freude, T. J. Kippenberg, and C. Koos, "Ultrafast optical ranging using microresonator soliton frequency combs", en, Science **359**, Publisher: American Association for the Advancement of Science Section: Report, 887–891 (2018).

[45] T. M. Fortier, A. Bartels, and S. A. Diddams, "Octave-spanning Ti:sapphire laser with a repetition rate >1 GHz for optical frequency measurements and comparisons", EN, Optics Letters **31**, Publisher: Optical Society of America, 1011–1013 (2006).

[46] J. W. Nicholson, M. F. Yan, P. Wisk, J. Fleming, F. DiMarcello, E. Monberg, A. Yablon, C. Jørgensen, and T. Veng, "All-fiber, octave-spanning supercontinuum", EN, Optics Letters **28**, Publisher: Optical Society of America, 643–645 (2003).

[47] F.-L. Hong, K. Minoshima, A. Onae, H. Inaba, H. Takada, A. Hirai, H. Matsumoto, T. Sugiura, and M. Yoshida, "Broad-spectrum frequency comb generation and carrier-envelope offset frequency measurement by second-harmonic generation of a mode-locked fiber laser", EN, Optics Letters **28**, Publisher: Optical Society of America, 1516–1518 (2003).

[48] F. Tauser, A. Leitenstorfer, and W. Zinth, "Amplified femtosecond pulses from an Er:fiber system: Nonlinear pulse shortening and self-referencing detection of the carrier-envelope phase evolution", EN, Optics Express **11**, Publisher: Optical Society of America, 594–600 (2003).

[49]M. Lezius, T. Wilken, C. Deutsch, M. Giunta, O. Mandel, A. Thaller, V. Schkolnik, M. Schiemangk, A. Dinkelaker, A. Kohfeldt, A. Wicht, M. Krutzik, A. Peters, O. Hellmig, H. Duncker, K. Sengstock, P. Windpassinger, K. Lampmann, T. Hülsing, T. W. Hänsch, and R. Holzwarth, "Space-borne frequency comb metrology", EN, Optica **3**, Publisher: Optical Society of America, 1381–1387 (2016).

[50]S. A. Meyer, J. A. Squier, and S. A. Diddams, "Diode-pumped Yb:KYW femtosecond laser frequency comb with stabilized carrier-envelope offset frequency", en, The European Physical Journal D **48**, 19–26 (2008).

[51]D. R. Carlson, D. D. Hickstein, W. Zhang, A. J. Metcalf, F. Quinlan, S. A. Diddams, and S. B. Papp, "Ultrafast electro-optic light with subcycle control", en, Science **361**, Publisher: American Association for the Advancement of Science Section: Report, 1358–1363 (2018).

[52]A. L. Gaeta, M. Lipson, and T. J. Kippenberg, "Photonic-chip-based frequency combs", en, Nature Photonics **13**, Number: 3 Publisher: Nature Publishing Group, 158–169 (2019).

[53]T. J. Kippenberg, R. Holzwarth, and S. A. Diddams, "Microresonator-Based Optical Frequency Combs", en, Science **332**, Publisher: American Association for the Advancement of Science Section: Review, 555–559 (2011).

[54]N. Picqué and T. W. Hänsch, "Frequency comb spectroscopy", en, Nature Photonics **13**, 146–157 (2019).

[55]K. W. Holman, R. J. Jones, A. Marian, S. T. Cundiff, and Jun Ye, "Detailed studies and control of intensity-related dynamics of femtosecond frequency combs from mode-locked Ti:sapphire lasers", IEEE Journal of Selected Topics in Quantum Electronics **9**, Conference Name: IEEE Journal of Selected Topics in Quantum Electronics, 1018–1024 (2003).

[56]D. Walker, T. Udem, C. Gohle, B. Stein, and T. Hänsch, "Frequency dependence of the fixed point in a fluctuating frequency comb", en, Applied Physics B **89**, 535–538 (2007).

[57]J.-C. Diels and W. Rudolph, *Ultrashort laser pulse phenomena: fundamentals, techniques, and applications on a femtosecond time scale*, en, 2nd ed, Optics and photonics (Elsevier / Academic Press, Amsterdam ; Boston, 2006).

[58]G. Agrawal, *Nonlinear fiber optics*, en, 6th ed. (Elsevier Inc, Cambridge, 2019).

[59]D. Strickland and G. Mourou, "Compression of amplified chirped optical pulses", en, Optics Communications **56**, 219–221 (1985).

[60]B. Saleh and M. Teich, *Fundamentals of Photonics, 3rd Edition* (Feb. 2019).

[61]R. Paschotta, J. Nilsson, A. C. Tropper, and D. C. Hanna, "Ytterbium-Doped Fiber Amplifiers", en, IEEE JOURNAL OF QUANTUM ELECTRONICS **33**, 8 (1997).

[62]E. Treacy, "Optical pulse compression with diffraction gratings", IEEE Journal of Quantum Electronics **5**, Conference Name: IEEE Journal of Quantum Electronics, 454–458 (1969).

[63]C. T. Kilian, *Modern Control Technology: Components and Systems*, en, Google-Books-ID: h35SAAAAMAAJ (Delmar Thomson Learning, 2001).

[64]K. J. Åström and R. M. Murray, *Feedback systems: an introduction for scientists and engineers*, en, OCLC: ocn183179623 (Princeton University Press, Princeton, 2008).

[65]M. Zhu and J. L. Hall, "Stabilization of optical phase/frequency of a laser system: application to a commercial dye laser with an external stabilizer", en, Journal of the Optical Society of America B **10**, 802 (1993).

[66]C. H. Henry and R. F. Kazarinov, "Quantum noise in photonics", en, Reviews of Modern Physics **68**, 801–853 (1996).